U.PORTO
FACULDADE DE CIÊNCIAS
UNIVERSIDADE DO PORTO
INSTITUTO DE CIÊNCIAS
BIOMÉDICAS ABEL SALAZAR
UNIVERSIDADE DO PORTO

MSc
2.º
CICLO
FCUP
ICBAS
2019

U.PORTO

Computational Modelling of Carbon Nanotubes
as Drug Carriers

Alexandre Ricardo Vieira Pinto

U.PORTO
FACULDADE DE CIÊNCIAS
UNIVERSIDADE DO PORTO
INSTITUTO DE CIÊNCIAS
BIOMÉDICAS ABEL SALAZAR
UNIVERSIDADE DO PORTO

Computational Modelling of Carbon Nanotubes as Drug Carriers

Alexandre Ricardo Vieira Pinto
Dissertação de Mestrado apresentada à
Faculdade de Ciências da Universidade do Porto
Bioquímica e Instituto de Ciências Biomédicas Abel Salazar

2019

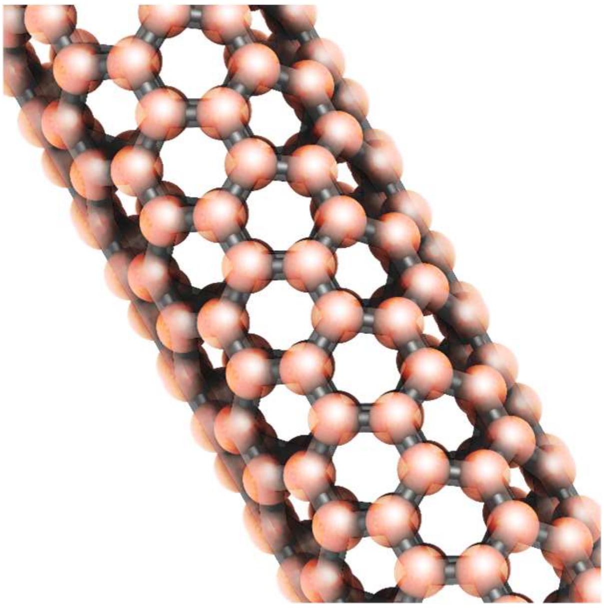

Computational Modelling of Carbon Nanotubes as Drug Carriers

Alexandre Ricardo Vieira Pinto
Mestrado em Bioquímica
Faculdade de Ciências da Universidade do Porto
Instituto de Ciências Biomédicas Abel Salazar
2018/2019

Orientador
Alexandre Lopes Magalhães, Professor Auxiliar,
Faculdade de Ciências da Universidade do Porto

U.PORTO

FACULDADE DE CIÊNCIAS
UNIVERSIDADE DO PORTO

INSTITUTO DE CIÊNCIAS
BIOMÉDICAS ABEL SALAZAR
UNIVERSIDADE DO PORTO

Todas as correções determinadas pelo júri, e só essas, foram efetuadas.

O Presidente do Júri,

Porto, ______/______/_________

Agradecimentos

A presente dissertação constitui um ponto de viragem no meu percurso académico, marcando a finalização do grau de mestrado em Bioquímica e o início da minha carreira profissional.

Durante esta jornada a Faculdade de Ciências da Universidade do Porto e o Instituto de Ciências Biomédicas Abel Salazar foram a minha “segunda casa”, proporcionando um excelente ambiente para o meu crescimento pessoal e científico. Como tal, quero começar por agradecer ao meu orientador Alexandre Magalhães, por toda a paciência, orientação, dedicação e pela constante partilha de conhecimentos. Agradeço em especial ao professor Pedro Fernandes pelo apoio e oportunidades que me proporcionou e ainda à professora Maria João Ramos pelo acolhimento no Departamento de Química Teórica. Agradeço também ao Rui e João por estarem sempre disponíveis para ajudar e ao resto do grupo pela boa disposição e ambiente.

Estou imensamente agradecido aos maiores impulsionadores desta minha jornada, os meus pais, porque foram eles que incentivaram este meu interesse pela ciência e pelas respostas aos mistérios do universo, suportando e motivando toda a minha aprendizagem até este ponto. Também com um papel de suporte importante, agradeço ao meu padrinho Carlos e á minha restante família (Marco, Tatiana, Carlos, Iolanda, Gonçalo e Mariana), por todo o apoio e encorajamento que me presenciaram. Aproveito também para agradecer às minhas grandes amizades por participarem nesta jornada ao meu lado (Gonçalo e Dmitriy). Grande parte da minha gratidão pertence à Sara, ela que foi o meu maior pilar pessoal e que contribui todos os dias para a minha felicidade e para o meu crescimento como pessoa.

Por fim, dedico esta tese aos meus avós Aida, Carlos, Luís e Rosalina.

Abstract

Since their discovery, carbon nanotubes and other related nanomaterials are on the spotlight due to their unique molecular structures and properties. The cage like structure of carbon nanotubes is especially appealing as a route to isolate drug molecules until they reach a specific cellular target where they can be delivered. In this sense, many studies have been published concerning the topic of carbon nanotube cellular toxicity, indicating that in certain conditions the nanomaterials present very little risks, and thus suitable to the drug delivery scope.

Accordingly, this project aims to explore through density functional theory (DFT) calculations, a novel covalent end-functionalization of single-walled carbon nanotubes (SWCNTs). It is proposed that the end-functionalization with a carboxylic acid derivative establishes a pH sensible molecular gate, considering intramolecular hydrogen bonds between the introduced functions which prevent diffusion of molecules from inside the SWCNT to the surrounding medium. The pH sensibility of the molecular gate arises from repulsion between deprotonated functions, leading to a conformational change upon deprotonation. Furthermore, the protonated functions are also predicted to oscillate between closed and opened conformations, however, is it reasonable to assume that the closed state is preferred.

Overall, the results suggest that the functionalized SWCNTs hold chemical properties that may be desirable in the design of a drug delivery system to enhance the efficiency of some pharmacological treatments. On the hand, the qualities present in these SWCNTS could extend the use to other areas through the incorporation in nanocomposites, such as catalysis and separation processes.

Keywords

Single-walled Carbon Nanotube (SWCNT), Carboxylic Acid, Functionalization, Hydrogen Bond, Non-Covalent Interactions, pH-sensitive, Drug Delivery, Quantum Mechanics, Density Functional Theory (DFT), Topology Analysis

Resumo

Desde a sua descoberta, nanotubos de carbono e outros nanomateriais relacionados estão em foco devido às suas estruturas e propriedades moleculares excecionais. A estrutura em forma de jaula dos nanotubos de carbono é especialmente apelativa como um meio para isolar fármacos até que eles atinjam um alvo celular específico onde poderão ser entregues. Neste sentido, foram vários estudos dirigidos ao tópico da toxicidade celular dos nanotubos de carbono, indicando que em certas condições os nanomateriais apresentam riscos insignificantes, e, portanto, são adequados para o âmbito de sistemas de entrega de fármacos.

De acordo, este projeto tem o objetivo de explorar, com cálculos da teoria do funcional da densidade (DFT), uma funcionalização terminal de nanotubos de carbono com parede simples (SWCNTs) inovadora. É proposto que a funcionalização com um derivado de ácido carboxílico estabeleça um portão molecular sensível ao pH, considerando ligações de hidrogénio intramoleculares entre as funcionalizações introduzidas, que previnem a difusão de moléculas do interior dos nanotubos para o meio. A sensibilidade ao pH do portão molecular advém de repulsão entre funcionalizações desprotonadas, induzindo uma mudança conformacional aquando da desprotonação. Além disso, também é previsto que as funcionalizações protonadas oscilem entre a conformação aberta e fechada, no entanto, é razoável assumir que o estado fechado é preferível.

No geral, os resultados sugerem que os nanotubos funcionalizados possuem propriedades químicas que podem ser desejáveis na conceção de um sistema de entrega de fármacos para aumentar a eficiência de alguns tratamentos farmacológicos. Por outro lado, as qualidades presentes nestes nanotubos podem ter o seu uso estendido a outras áreas através da incorporação em nanocompósitos, processos de catálise e de separação.

Palavras-Chave

Nanotubos de Carbono de Parede Simples, Ácido Carboxílico, Funcionalização, Ligação de Hidrogénio, Interações Não-Covalentes, Sensibilidade ao pH, Entrega de Fármacos, Mecânica Quântica, Teoria do Funcional da Densidade, Análise Topológica

Index

List of Figures, Tables and Appendixes

Figures

Tables

Appendixes

Appendix 1 – Carbon nanotube bond length and angle parameters

Appendix 2 – Bond lengths associated with the functionalizations

Appendix 3 – Bond and dihedral angles associated with the functionalizations

Appendix 4 – IR vibrational spectra

Appendix 5 – Topology parameters associated with all hydrogen bonds

Appendix 6 – Relative energy of the B3LYP/6-31g dihedral bidimensional scans

List of Equations

List of Abbreviations

A – Acceptor

BCP – Bond critical point

B3LYP – Becke 3 and Lee–Yang–Parr hybrid functional

B88 – Becke 88 exchange functional

B97 – Becke 97 correlation functional

BLG – Bi-layered graphene

CP – Critical Point

CCP – Cage critical point

CNT – Carbon nanotube

CVB – Core-valence bifurcation

D – Donor

DFT – Density functional theory

ED – Electron density

ELF – Electron localization function

FLG – Few-layered graphene

GGA – Generalized gradient approximation

GTO – Gaussian type orbital

H – Hydrogen

HB – Hydrogen bond

HF – Hartree-Fock

HRTEM – High resolution transmission electron microscopy

IEF-PCM – Integral equation formalism of the polarizable continuum model

KS – Kohn-Sham

LDA – Local density approximation

LSDA – Local spin-density approximation

MWCNT – Multi-walled carbon nanotube

M06 – Minnesota 06 functionals

M06-2X – Minnesota 06-2X functional

NCI – Non-covalent interactions index

NCP – Nuclear critical point

NMR – Nuclear magnetic resonance

NPE – Nonhomogeneous Poisson equation

PBE0 – Perdew–Burke-Ernzerhof hybrid functional

QTAIM – Quantum theory of atoms in molecules

RCP – Ring critical point

SLDB – Same level different basis approach

SLG – Single-layered graphene

SMD – Solvation model based on density

STO – Slater type orbitals

SWCNT – Single-walled carbon nanotube

Chapter I

Introduction

"Without sensibility no object would be given to us, without understanding no object would be thought. Thoughts without content are empty, intuitions without concepts are blind."

Immanuel Kant, The Critique of Pure Reason (1781)

1. Carbon Nanomaterials

Carbon is a very special chemical element, acting as a core constituent in numerous chemical structures, including those which allowed life to begin millions of years ago. The ground-state electronic structure of an isolated carbon atom is $(1s)^2$ $(2s)^2$ $(2p)^2$, having four valence electrons available for bonding. Because the ground state orbitals in the valence-shell are similar enough in energy, when comparing with the binding energy from covalent bonds, an electron from the 2s orbital is easily excited to the empty 2p orbital. The wave function of the 2s electron is then free to merge with the 2p electrons wave functions, in a phenomenon called hybridization (Fig. 1), culminating in degenerated hybrid orbitals[1-3].

As consequence of the three hybridized states, carbon forms many different types of structures[4, 5]. These structures, although having mostly nonpolar C atoms, can act as scaffolds that anchor diverse functional groups, culminating in distinct chemical properties. The present model for carbon in organic compounds elucidates that this atom is bonded to several types of elements, in addition to itself, in innumerable diverse ways, ensuing a versatile building block for constructing complex chemical structures[3]. Indeed, nowadays a great focus of nanoscience is directed towards structures exclusively composed by C atoms, as in graphene, carbon nanotubes (CNTs) and fullerenes[3, 6, 7] (Fig. 2).

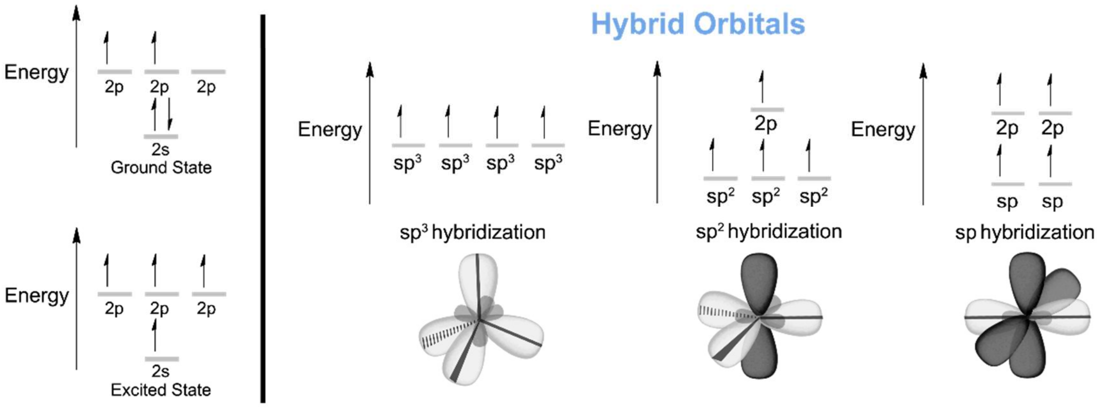

Figure 1 – Orbital Hybridization in Carbon.

When we look at carbon allotropes, there are many spatial arrangements the carbon atoms can take due to the geometrical flexibility discussed above. For example, diamond can have a cubic or hexagonal crystal structure where the C atoms are sp^3 hybridized, bonded together in a tetrahedral arrangement (Fig. 3a), while graphite consists of a layered planar structure, each sheet having a 2D repetitive hexagonal arrangement for carbon which is sp^2 hybridized (Fig. 3b) [3]. As result of the structural variation, their properties also differ. Since the tetrahedral carbon atoms in diamond are covalently bond in a strain free structure which is very stable, the bulk material has high hardness and thermal conductivity[8].

The sp^2 atoms in graphite, however, have a trigonal planar geometry, and the overlap between their out-of-plane 2p orbitals generates π bonds that result in a parallel delocalized π-system in the entire sheet. The electron delocalization present in each sheet provides graphite with high electrical conductivity[9]. Nonetheless, the layers are connected by weak van der Waals bonds from the interaction between bonding π orbitals and the empty antibonding π orbitals from the adjacent layer, making it a material very prone to exfoliation[8, 9]. Another consequence of this structural arrangement is that the properties tend to be anisotropic, for example, the electrical and thermal conductivities also differ depending on the direction relative to the crystal structure[3].

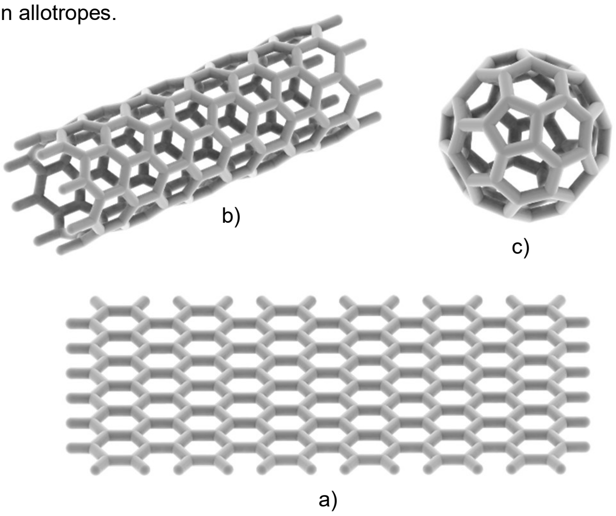

Figure 2 – Examples of tridimensional structures of carbon allotropes.

a) Graphene sheet;

b) Carbon Nanotube;

c) Buckminster Fullerene;

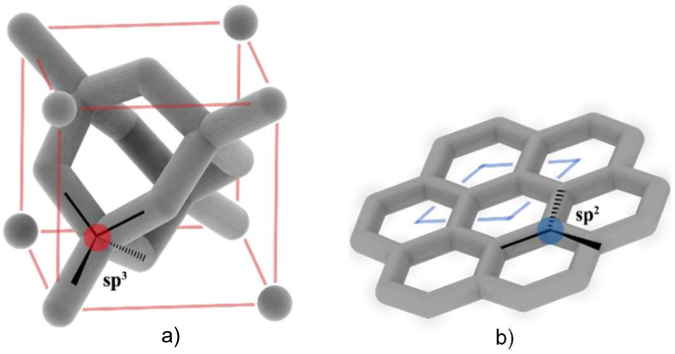

a) b)

Figure 3 – Unit cells of a) diamond and b) graphene.

1.1 Graphene

Now focusing on the individual sheets of graphite as another type of allotrope, the graphene nanomaterial. Graphene was first isolated in 2004, through a technique that consisted in mechanical exfoliation of graphite with scotch-tape, developed by Geim and Novoselov[10]. Their work set in motion great advances in graphene research and they were awarded the Nobel Prize in 2010 for "*ground-breaking experiments regarding the bidimensional material graphene*"[11]. Since then, graphene has become a hot topic for research, which includes new production methods, functionalization, nanocomposites and toxicity, as well as applications in a wide range of areas such as flexible sensors and electronics, biotechnology, aerospace, automotive, among others[12-14].

This mono-layered type of allotrope is characterized by a hexagonal periodic motif, where each atom is sp^2-hybridized in a trigonal planar geometry, with bond angles of 120.0º, as aforementioned for the graphite case. The bonds between C atoms are very strong and have a mean length of 1.412 Å, a value that falls in the interval between mean single and double carbon-carbon bond lengths[8]. This arises because the overlapping of sp^2 orbitals leads to the formation of σ bonds, but the remaining 2p orbitals participate in the formation of a delocalized π-system (Fig. 4) that elevates the bond order character of the $C-C$ bonds to that amidst single and double[8].

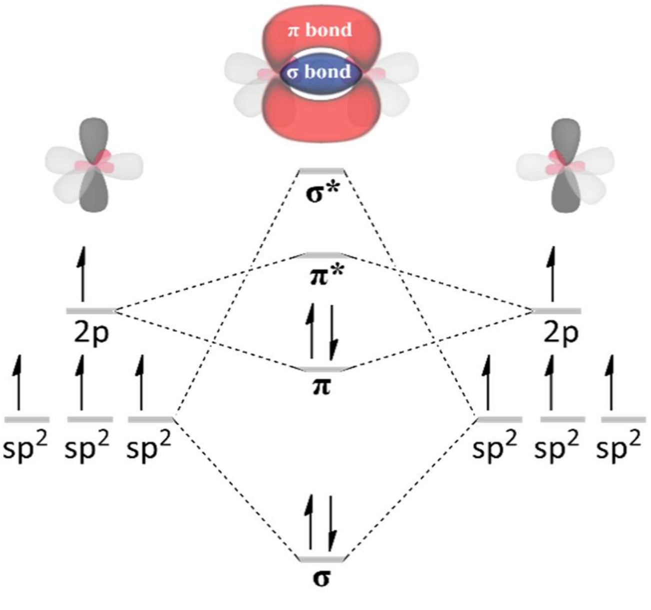

Figure 4 – Schematic and graphic representation of molecular orbitals between sp^2 carbon atoms.

1.1.1 Geometric Structure

Since graphene is a periodic system, the geometric description is of great value to understand its properties, principally to elucidate the electronic band structure. Indeed, P. R. Wallace employed the geometrical structure of graphene to calculate its band structure, in order to approximate that of graphite, more than half a century before graphene was even synthesized[15, 16]. The bidimensional direct lattice of graphene (a_1, a_2) can be defined by a rhombic unit cell, S_g, including two nonequivalent carbon atoms (A and B), which is essentially described as two triangular Bravais sublattices, each one having a different atom basis[17], as depicted in Fig. 5a. Considering a cartesian coordinate system (x, y) with origin at the center of one hexagon, each site on the sublattice is described by $\overrightarrow{R_\iota} = m\vec{a}_1 + n\vec{a}_2$, the $\vec{a}_1$ and $\vec{a}_2$ vector components being defined as:

$$\vec{a}_1 = a_0(\frac{\sqrt{3}}{2}e_x + \frac{1}{2}e_y) \qquad \vec{a}_2 = a_0\left(\frac{\sqrt{3}}{2}e_x - \frac{1}{2}e_y\right) \qquad (1)$$

The basis vectors form an angle of $\frac{\pi}{3}$ degrees and have equivalent lengths[18], these being related to the lattice constant a_0 and the interatomic distance by $|\vec{a}_1| = |\vec{a}_2| = a_0 = \sqrt{3}a_{c-c}$. The reciprocal lattice (b_1, b_2) unit cell, Σ_g, represented in Fig. 5b is spanned by two primitive vectors $\vec{b}_1$ and $\vec{b}_2$, with the same length $|\vec{b}\,| = 4\pi\sqrt{3}a_0$, and form a $\frac{2\pi}{3}$ angle[18]. Their components are defined as:

$$\vec{b}_1 = a_0(\frac{2\pi}{2}e_x + \frac{1}{2}e_y) \qquad \vec{b}_2 = a_0\left(\frac{\sqrt{3}}{2}e_x - \frac{1}{2}e_y\right) \qquad (2)$$

The basis vectors mentioned for the direct and reciprocal lattices can be related by $\vec{a}_\iota \cdot \vec{b}_j = 2\pi \cdot \vec{\delta}_{ij}$, where $i, j = 1{,}2$ and $\vec{\delta}_{ij}$ represents the vectors that connect a site to the closest neighbors from the other sublattice[9]. Also, the unit cell areas from both lattices can be related[3] by $A_g \cdot B_g = (2\pi)^2$. The first Brillouin zone depicted in Fig. 5b contains the high symmetry points $(\Gamma, K, K'$ and $M)$ that are translated by the reciprocal lattice vectors to equivalent points in the corners of the hexagon where the band structure is plotted[9].

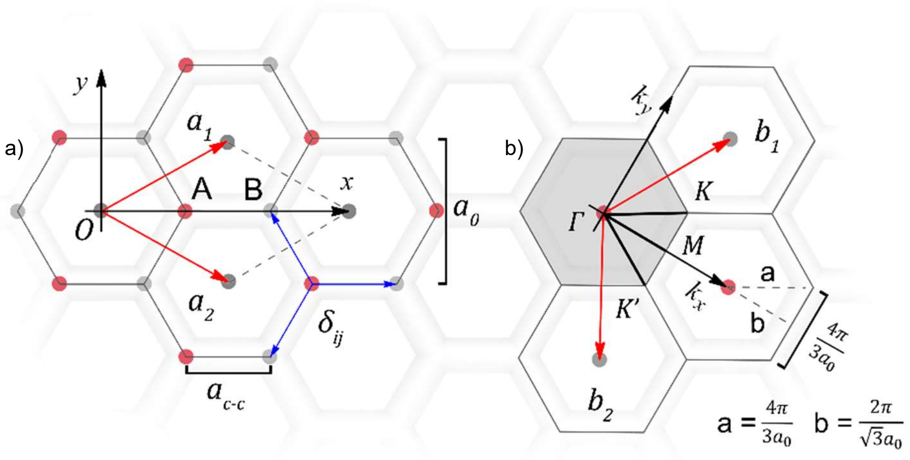

Figure 5 – a) Direct lattice and b) reciprocal lattice of the unit cell from graphene.

1.1.2 Electronic Structure

The vectors in the direct lattice have length dimensions, whilst the reciprocal lattice has their vectors defined in terms of the reciprocal of length, and therefore one can view the reciprocal lattice as a Fourier transform of the direct lattice[3]. The direct lattice exists in a position space, concurrent with the reciprocal lattice existing in the reciprocal space, or k-space, which corresponds to all the wave vectors k of the system, and hence, the electronic band structure is calculated exploring the periodic nature of graphene through the k-space.

Considering the nearest neighbor tight-binding model, the following Hamiltonian can be written:

$$H = -t \sum_{\langle i,j \rangle,\sigma} \left(a_{\sigma,i}^{\dagger} b_{\sigma,j} + h.c. \right) - t' \sum_{\langle\langle i,j \rangle\rangle,\sigma} \left(a_{\sigma,i}^{\dagger} a_{\sigma,j} + b_{\sigma,i}^{\dagger} b_{\sigma,j} + h.c. \right) \tag{3}$$

,where $a_{\sigma,j}$ ($a_{\sigma,i}^{\dagger}$) annihilates (creates) an electron with spin σ on site R_i on sublattice A (or B), t (≈2.8 eV) is the nearest neighbor hopping energy and t' is the next neighbor hopping energy[19]. Deriving Eq. 3 gives the resultant function for the π electron dispersion relation in graphene[16, 20]:

$$E^{\pm}(k_x, k_y) = \pm t \sqrt{1 + 4cos\frac{\sqrt{3}k_x a_0}{2} cos\frac{k_y a_0}{2} + 4cos^2\frac{k_y a_0}{2}} \tag{4}$$

The plot of Eq. 4 versus k_x and k_y is reported in Fig. 6a, where the negative part of the function corresponds to the filled π-band (valence band) and the positive to the empty π*-band (conduction band)[18]. The two bands meet at the Dirac points, represented by $K\ (\frac{2\pi}{\sqrt{3}a_0}, \frac{2\pi}{3a_0})$ and $K'\ (\frac{2\pi}{\sqrt{3}a_0}, -\frac{2\pi}{3a_0})$, which coincide with the Fermi level and also where the density of states is zero, making graphene a zero gap semiconductor[4, 16]. As consequence, near the Dirac points the charge carriers display unique properties, that are best described through the famous Dirac equation in the context of quantum electrodynamics theory, which includes a relativistic view:

$$\widehat{H} = \hbar v_f \begin{pmatrix} 0 & k_x - ik_y \\ k_x + ik_y & 0 \end{pmatrix} = \hbar v_f \sigma k \tag{5}$$

,where k stands for the quasiparticle momentum, σ the 2D Pauli matrix, v_f (≈0,87x10^6 m/s)[3, 18] is the Fermi velocity and ħ is the reduced Planck constant[21]. This proposes a linear relation between energy and momentum at low energy values (Fig. 6b), that suggests a massless quasiparticle behavior for electrons in this condition, analogous to that of neutrinos but slower ($v_f \approx \frac{c}{300}$) and carrying charge[16]. The quasiparticles, designated by the term massless Dirac fermions, are better characterized as electrons who lost their rest mass, travelling unimpeded through the lattice at high speeds[21, 22].

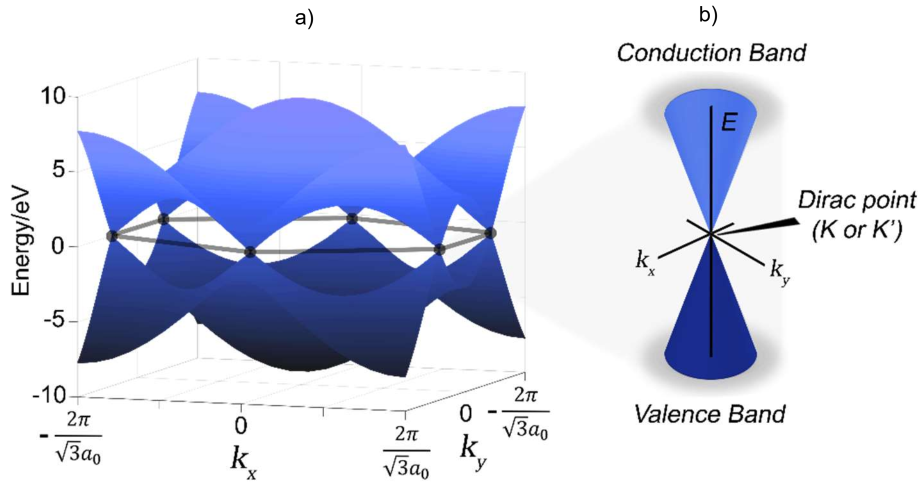

Figure 6 – a) Dispersion relation energy plot from the tight binding approximation and b) Dirac cones.

1.1.3 Properties of Graphene

The peculiar electronic structure of graphene has a deep impact in its properties, which present themselves as very distinct from most known materials. For instance, the bidimensional material displays low electronic noise from the thermal agitation of charge carriers (Johnson noise), a very large surface area and changes in the charge carrier properties upon adsorption of molecules, making it optimal for the development of sensors[23]. Relative to electron transport, graphene presents high charge carrier density[21] (10^{13} cm^{-2}), high charge carrier mobility[21, 23] (15,000 $cm^2V^{-1}s^{-1}$) and very low resistivity (10^{-6} ohm-cm), which renders the material unique for the use in electronic devices, such as transistors[23]. Another important feature is the ambipolar effect at room temperature, that allows to modulate the charge carriers between electrons and holes upon the nature of the applied voltage[21, 24]. As consequence of the relativistic behavior of electrons, Klein tunneling also arises, being described as a phenomenon in which the particles always cross a potential energy barrier, in contrast with quantum tunneling of non-relativistic particles, which have a given probability of crossing an energetic barrier[16, 19, 25]. Thanks the high energy bonds and the delocalized π-system, graphene stands out as material stronger than diamond that is also a remarkable thermal and electric conductor[26].

Nonetheless, it is important to clarify that the theoretical approach made for graphene only considers an idealized bidimensional layer that is one-atom thick, and the properties of the material vary when more layers are added until it is regarded as tridimensional graphite. In this sense, three types of graphene can be defined: single-layer (SLG), bi-layer (BLG) and few-layer (FLG), which can have three to ten sheets of graphene stacked[21]. The different types of edges present in graphene materials, zig-zag and armchair, also show dissimilar electronic properties[19]. Furthermore, covalent functionalization and presence of defects in the graphene structure can also impact the properties of the material[16].

1.2 Carbon Nanotubes

Graphene is considered the building block of sp^2 carbon structures, because ideally all the graphitic forms of carbon can be conceived from a graphene sheet. Perhaps carbon nanotubes are the most obvious to this matter, since they can be regarded as a rolled graphene sheet, with edges bonded together to form a hollow cylinder. Notably, CNTs and fullerenes were discovered more than a decade before SLG was first isolated. Although some studies announced the discovery of tubular structures made of C atoms between 1950 and 1990[27, 28], the popularity of CNTs only began to thrive in 1991, after S. Ijima reported the synthesis of multi-walled carbon nanotubes (MWCNTs) through the arc-discharge evaporation method and observation with the high resolution transmission electron microscopy (HRTEM) technique[29].

Nowadays, CNTs have a wide range of potential applications[30], such as biomedical (e.g. drug-delivery, biosensing), electronic (e.g. transistors) and energetic (e.g. electrodes), among others. Nevertheless, the methods related to synthesis, separation and dispersion of CNTs have several limitations, especially when conceptualizing the mass-production of these nanomaterials for the implementation in reproducible products that are economically viable[30-33].

The CNT atomic structure is essentially the same as graphene, sp^2-hybridized carbon atoms bonded to three other carbon atoms in a repetitive hexagonal motif, however there are differences in the π-system due to the curvature[3, 34, 35], and additionally, alternative orientations for the hexagonal motifs (Fig. 7a) effect the system electronic properties[20, 24, 36]. Considering that graphene can be classified on regard to the number of layers present in the material, likewise CNTs can be classified on this basis as single-walled and multi-walled[37], if they are formed by one tube or more concentric tubes (Fig. 7b), respectively.

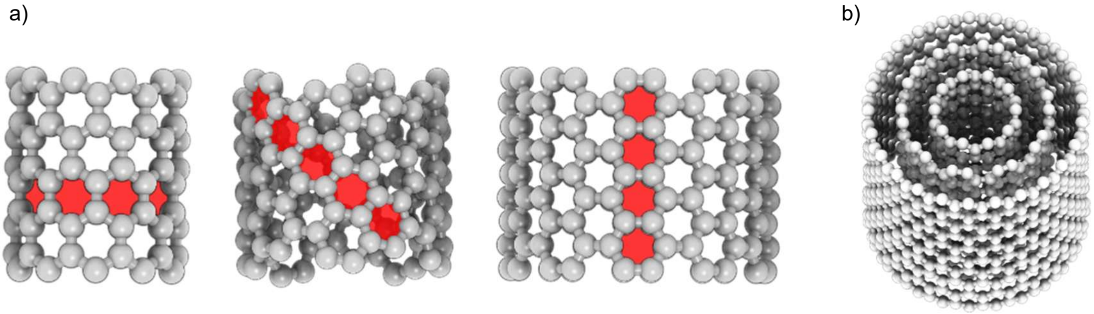

Figure 7 – Representation of a) different hexagonal orientations for zigzag, chiral and armchair nanotubes, respectively from left to right, and b) multi-walled carbon nanotube.

1.2.1 Geometric Structure

The structure of CNTs is represented as the rolling of a graphene sheet into a tube, according to a chiral vector (Fig. 8) [36, 38]. The chiral vector represents the circumference of the cylinder, such that the two points at the beginning and end of the vector are coincident. It is constructed as a linear combination of the real space basis vectors from the graphene lattice (Eq. 6) [17, 38], and is therefore defined by the chiral index (n, m):

$$\vec{C_h} = n \cdot \vec{a}_1 + m \cdot \vec{a}_2 \tag{6}$$

The two integers comprising the chiral index label all possible CNT structural arrangements and are generally divided in three categories: zigzag, armchair and chiral. The $(n, 0)$ CNTs are classified as zigzag and have a chiral angle $\theta = 0°$, this corresponding to the angle between the chiral vector and the zigzag direction (Eq. 7), while the armchair (n, n) CNTs display $\theta = 30°$, both types with high symmetry[39].

$$\theta = \arctan\left(\frac{\sqrt{3m}}{2n + m}\right) \tag{7}$$

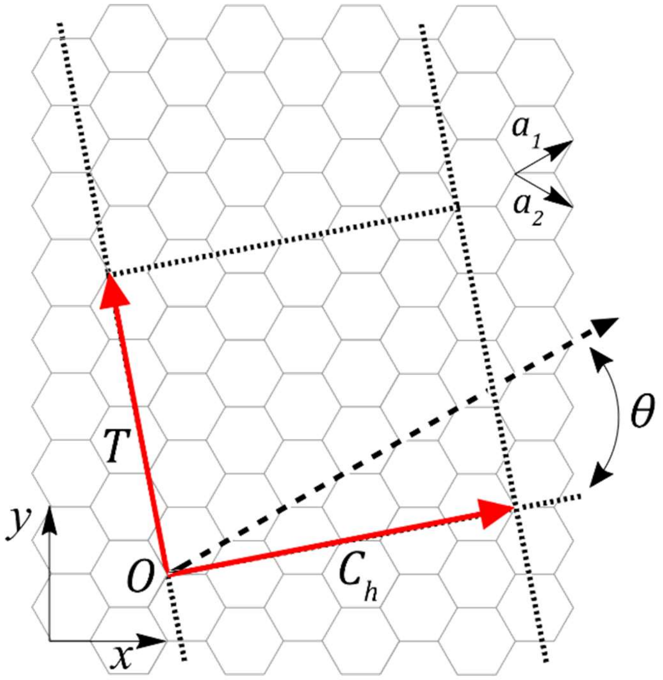

Figure 8 – Unit cell for carbon nanotubes.

Zigzag CNTs are characterized by having the hexagonal motif oriented such that opposing C atoms are parallel to the tube axis, in contrast to armchair CNTs, where the hexagonal motif is oriented perpendicular to the axis[17]. Chiral (n, m) CNTs have a chiral angle between that of zigzag and armchair $0° < \theta < 30°$, thus the hexagonal pattern is distorted between the two limits of the zigzag and armchair structures, forming a helicoidal structure and additionally producing enantiomers due to loss of symmetry[8, 17]. The CNT diameter is related to the chiral vector by[8, 17]:

$$d = \frac{|\vec{C_h}|}{\pi} = \frac{a_0\sqrt{n^2 + nm + m^2}}{\pi} \qquad (8)$$

The unit cell of the CNT is a rectangle of sides equivalent to the chiral and translation vectors, which are always perpendicular and have an intersection at O. The translation vector $\vec{T}$ is given by:

$$\vec{T} = t_1 \cdot \vec{a}_1 + t_2 \cdot \vec{a}_2 \qquad t_1 = \frac{2m+n}{d_R} \qquad t_2 = -\frac{2n+m}{d_R} \qquad (9)$$

, where d_R is the greatest common divisor between $(2m + n)$ and $(2n + m)$ [8, 17]. The area of the unit cell is then $\vec{C_h} \times \vec{T}$, and the area of the unit cell from graphene is $\vec{a}_1 \times \vec{a}_2$, thereby the number of primitive unit cells per CNT unit cell is[8, 17]:

$$N = \frac{|\vec{C_h} \times \vec{T}|}{|\vec{a}_1 \times \vec{a}_2|} = \frac{2(m^2 + mn + n^2)}{d_R} \qquad (10)$$

This idealized model for the CNT may be useful to describe general classes of nanotubes, yet the nanotube morphology may display several distortions like vacancies and Stone-Wales defects[39, 40]. The opened tips resulting from this rolling model are terminated by a spherical cap that could vary in structure, displaying pentagons and hexagons, some authors even point it as the main factor in controlling the chirality during synthesis[41].

1.2.2 Electronic Structure

The band structure for SWCNTs is a derivation of the one from graphene. The vectors from the unit cell are orthogonal to each other, so the reciprocal lattice vectors are related to them by:

$$\vec{C_h} \cdot \vec{k}_{||} = 0 \qquad \vec{C_h} \cdot \vec{k}_{\perp} = 2\pi \qquad \vec{T} \cdot \vec{k}_{||} = 2\pi \qquad \vec{T} \cdot \vec{k}_{\perp} = 0 \qquad (11)$$

, where $\vec{k}_{\perp}$ and $\vec{k}_{||}$ are wave vectors aligned perpendicular and parallel to the CNT longitudinal axis, respectively[20]. The wave vectors can then be devised in relation to the reciprocal lattice vectors from graphene as[20]:

$$\vec{k}_{\perp} = \frac{1}{N}(-t_2\vec{b}_1 + t_1\vec{b}_2) \qquad \vec{k}_{||} = \frac{1}{N}(m\vec{b}_1 - n\vec{b}_2) \tag{12}$$

The $\vec{k}_{||}$ vector is continuous for a CNT of infinite length, on the other hand, $\vec{k}_{\perp}$ has a periodic boundary condition imposed by the chiral vector resulting in quantization of the vector around the circumference[38]:

$$\vec{k}_{\perp} \cdot \vec{C}_h = 2\pi p\,, \quad p \in \mathbb{Z} \tag{13}$$

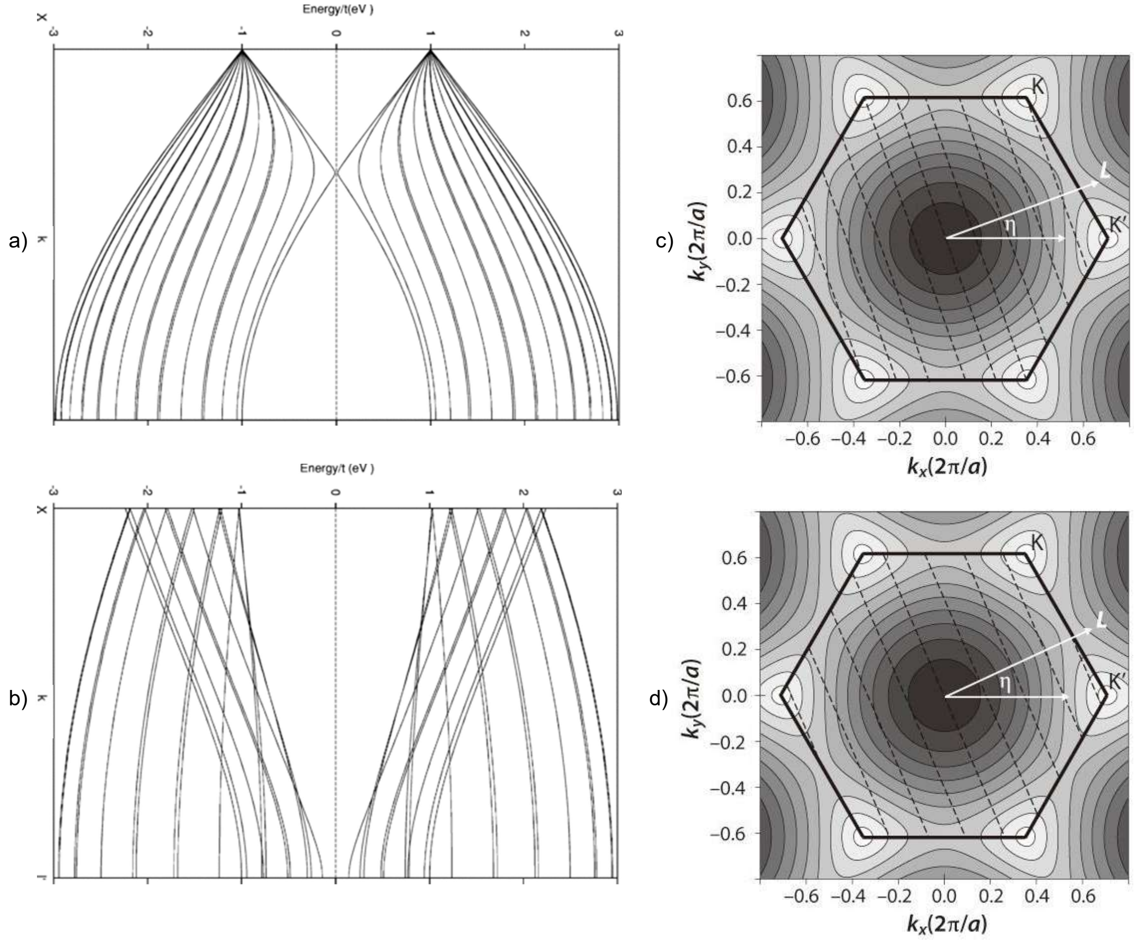

Figure 9 – Band structure from the folding zone method of a) metallic (5,5) CNT and a (b) semiconducting (5,0) CNT[1], and cross-sections on the band structure of graphene for c) metallic and d) semiconducting nanotubes[2].

[1] Iyakutti, K.; Bodapati, A.; Peng, X.; Keblinski, P.; Nayak, S. Electronic Band Structure, Electron-Phonon Interaction, And Superconductivity Of (5,5), (10,10), And (5,0) Carbon Nanotubes. Physical Review B 2006, 73.

[2] Ando, T. The Electronic Properties Of Graphene And Carbon Nanotubes. NPG Asia Materials 2009, 1, 17-21.

As result of being quantized, the allowed values of $\vec{k}_{\perp}$ determine the band structure for the SWCNTs as unidimensional cross-sections of the band structure from graphene (Fig. 9) [20, 24]. Since $\vec{k}_{\perp}$ is a vector along the circumference, and the latter depends of the chirality index (n, m), the electronic properties of the CNT will vary for different chiralities[20, 24, 39]. If the condition $(n - m) = 3q\ ,\ q \in \mathbb{Z}$ is satisfied, then an allowed wave vector will intersect the Dirac point of the Brillouin zone, generating a metallic CNT (Fig. 9a and Fig. 9c) [20, 24]. Otherwise, the cross-section of the band-structure from graphene won't intersect the Dirac point, culminating in a finite gap between the conduction and valence band, and making the CNT a semiconductor (Fig. 9b and Fig. 9d) [20, 24].

1.2.3 Properties of Carbon Nanotubes

As result of the similarity between structures, the properties of CNTs resemble that of graphene in many aspects. Both materials have a high surface area, but while graphene is a bidimensional material, the nanotubes have a high aspect ratio that renders them quasi-unidimensional materials, and therefore the properties tend to be anisotropic[42]. The curvature of CNTs relative to graphene imparts a pyramidalization angle above zero that misaligns the π-orbitals, which leads to an increase in reactivity[43]. The latter effect is negligible for CNTs with a large diameter, as it approximates the extreme case of graphene.

By virtue of the strong sp^2 bonding in a quasi-unidimensional structure, CNTs display high mechanical resistance while also having radial elasticity[37, 39], as well as high thermal conductivity[30, 31]. Because CNTs are quasi-unidimensional, the charge carrier transport is ballistic[37], thus being able to harbor very large current densities (100 $MA.cm^{-2}$) and high carrier mobilities (10^5 $cm^2V^{-1}s^{-1}$)[3], as well as low resistivities (10^{-4} ohm-cm)[37], making them very advantageous for electronic and electrochemical devices. Practical applications include the production of nanocomposites[39] with enhanced properties, gas and hydrogen storage, sensors, batteries and capacitors, solar cells, among many more [30, 37].

MWCNTs show more diffuse properties due to loss of one-dimensionality, so their applications are somewhat more restricted, and the presence of defects and functionalizations can also influence the properties[4]. In this sense, it is necessary that synthesis and functionalization methods lead to CNTs with monodisperse characteristics to ensure reproducible products in the mentioned applications[32].

1.2.4 Functionalization

In the past years, several different approaches on CNT functionalization were reported, targeting the production of specialized structures with improved properties[44]. The approaches diverge in the interaction between the carbon structure and the functional groups, which has covalent or non-covalent character[37, 44]. Covalent functionalization occurs through chemical bonding of functional groups at more reactive sites of the CNTs[33]. It usually takes place with highly reactive molecules in defect sites of the sidewall (Fig. 10a) [44, 45] or the tips of CNTs[46, 47], the latter being more reactive considering the effect of the curved geometry on π-conjugation[33, 48]. The functional groups to be introduced include hydroxyl, amino, alkyl, halogenates among others[33, 49, 50], and these can even be used as sites for further chemical reactions such as the covalent attachment of macromolecules (e.g. proteins, polymers) [49, 51].

At the tips, a curved end-cap structure closes the CNTs, however, treatment with strong acids (e.g. HNO_3, H_2SO_4) or strong oxidant agents (e.g. $KMnO_4$, O_3) leads to oxidative defects in the carbon structure which can include the opening of the tips and holes in the sidewalls[49, 52, 53]. The oxidation process also results in functionalization of the formed defects with groups containing oxygen, for example, carboxylic acids, ketones, alcohol and ester moieties, these also providing an anchor to harbor the introduction of other molecules[49, 50, 53, 54]. The covalent functionalizations are problematic in the view of retaining the original properties, since they are formed during harsh treatments that damage the structures and introduce unwanted defects, leading to disruption of the π-conjugated system and consequent loss of electrical and thermal properties[49, 55].

Non-covalent functionalization addresses this problem because it’s based of non-covalent interactions that do not disrupt the CNTs framework, thus allowing the preservation of the original properties[44, 56]. This approach relies on weak interactions such as π-π stacking and van der Waals, and so the molecules need to have present aromatic or hydrophobic portions in order to interact with the CNTs efficiently[44, 52, 56, 57]. Small drugs and other kinds of molecules can be encapsulated inside the nanotubes by interaction with the inner walls of the CNTs, experiencing confinement from the solvent[32]. Molecules such as surfactants and saccharides can simply adsorb to the outer surface, while some polymers and other complex molecules are wrapped around the CNTs (Fig. 10b) [44, 52, 56, 58, 59]. Importantly, amphiphilic molecules can change the interfacial properties of the nanotubes, adding polar or charged groups that act as solvation sites to enhance dispersion[56, 57].

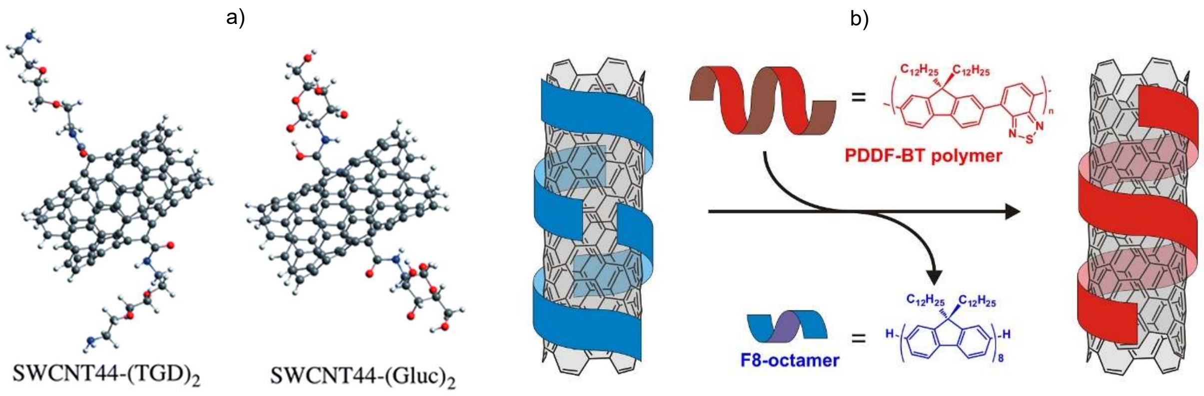

Figure 10 – a) Sidewall covalent bi-functionalization with triethylene glycol diamine and glucosamine[1]. b) Reversible wrapping with two different oligomers[2].

[1] Díaz-Cervantes, E.; García-Revilla, M.; Robles, J.; Aguilera-Granja, F. Solubility Of Functionalized Single-Wall Carbon Nanotubes In Water: A Theoretical Study. Theoretical Chemistry Accounts 2017, 136.

[2] Berton, N.; Lemasson, F.; Hennrich, F.; Kappes, M.; Mayor, M. Influence Of Molecular Weight On Selective Oligomer-Assisted Dispersion Of Single-Walled Carbon Nanotubes And Subsequent Polymer Exchange. Chemical Communications 2012, 48, 2516.

1.2.5 Dispersion, Biocompatibility and Drug Delivery

Since CNTs feature a very hydrophobic structure, their use in physiological conditions is severely limited by their dispersion in aqueous media, as they tend to form insoluble aggregates[49, 52, 60]. To overcome the attractive forces between CNTs and make stable dispersions, it is necessary to introduce new interfaces that can establish strong interactions with the solvent[61]. Many functionalization studies address this problem to enable their use as potential drug-delivery systems in biological medium, such as covalent functionalization with hydrophilic molecules or non-covalent functionalization with surfactants or biopolymers[45, 49, 52, 62-64]. The functionalizations need to be biocompatible to avoid cell toxicity, hence there is a preference for molecules with biological origin or analogs and greener synthesis methods sustainable at large scale[61, 62].

Biodegradation of CNTs can be carried out by enzymes that are present in human cells, for instance, myeloperoxidase and other peroxidases have been shown to oxidize SWCNTs[65]. Further mechanisms rely on the presence of functionalizations, for example, human albumin binds functionalized SWCNTs via electrostatic interactions to increase elimination[65]. While some studies point to the cellular toxicity of carbon nanotubes, through DNA damage and oxidative stress[65-68], ultimately leading to apoptosis, this depends on several factors, which include the length, the presence of defects and impurities, the nature of the dispersion agent and covalently bound molecules, and presence of additional nanotube layers, among others[67, 69].

The drugs used in cancer and other diseases generally have problems related to lack of cell-specificity and having a narrow therapeutic window[70, 71]. Drug-delivery systems can enhance the efficiency of these treatments, targeting specific cellular types where an encapsulated drug is to be delivered, and thus solving the mentioned problems[52, 71]. CNT formulations that surpass the toxicity-related issues can be used for this purpose[61, 62, 71], as they can efficiently encapsulate drugs, providing protection from enzymatic activity and longer circulation times, while having the advantage of being readily internalized by cells via phagocytosis and endocytosis[32, 70, 72-74]. The functionalizations present may include molecules that recognize a specific cell component or that interact with a pharmacological target, thus ensuing an enhancement of the accumulation in targeted cell types[51].

2. Hydrogen Bonding

Hydrogen bonds have been a subject of debate for a long period of time, since they constitute a common interaction of great importance to many chemical and biochemical phenomena, nevertheless the complexity inherent to the core contributions of the interaction ensued a troubled search for its definition[75]. Currently, the view of HBs is far more convoluted relative to the time of their introduction, being characterized by several criteria. HBs are defined as an attraction between a hydrogen atom H on a polarized bond $D-H$ and an atom A with an electron rich region (Fig. 11a). The strength of the HB tends to increment with increase in electronegativity of D and linearity of the interaction, resulting also in shorter bonds[76]. In terms of the atom types having the role of D or A, there has been some debate around the matter, but some authors report that D can be any element more electronegative than H ($F, N, O, C, P, S, Cl, Se, Br$ and I), while A belongs in the same list with the addition of π-electrons[77]. Albeit the low electronegativity of carbon, it has been shown to act as donor in weak HBs with N and O[78].

However this is a broad description since the contributions to the interaction tend to vary with dependency on several factors[75]. Under the circumstances, IUPAC established in 2011 a set of classification parameters that evaluate the main contributors to HBs: 1) the forces involved in the attraction include electrostatic, charge-transfer and dispersion; 2) the bond $D-H$ is covalent and polarized; 3) the angle $D\widehat{H}A$ is ideally linear; 4) the length of the $D-H$ bond typically increases upon interaction; 5) characteristic NMR signatures arise from the $D-H\cdots A-X$ bond; 6) experimental observation is only possible if the Gibbs energy of formation of the bond is greater than the thermal energy of the system[75]. Some authors classify HBs relatively to the total energy (Fig. 11b), reporting that weak interactions lie in the range below 4 kcal.mol^{-1}, medium interactions in 4-15 kcal.mol^{-1} and strong interactions in 15-40 kcal.mol^{-1} [79].

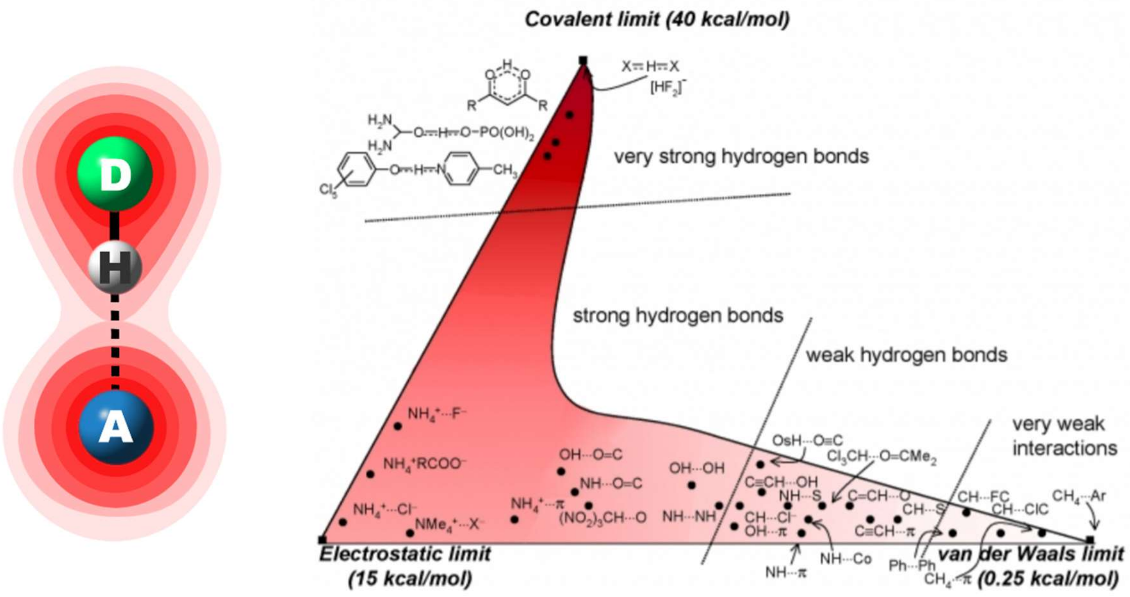

Figure 11 – a) Representation of hydrogen bond donor (D), hydrogen (H), acceptor (A) and fictitious electron density isovalues. b) Hydrogen bond classification by total energy of interaction[1].

[1] Desiraju, G. IUPAC Definition Of The Hydrogen Bond. Terminology And Nomenclature. Acta Crystallographica Section A Foundations and Advances 2017, 73, C308-C308.

The HB interaction can be decomposed into electrostatic interaction between permanent multipoles, inductive forces between permanent and induced multipoles, dispersion from instantaneous multipole-induced multipoles, charge transfer phenomena leading to partial covalency, and exchange-correlation effects from short-range repulsion due to electronic overlap[77]. Despite dispersion forces having a contribution, there is a strong directionality dependency in hydrogen bonds that can be attributed to electrostatic interactions, therefore an interaction originated predominantly by dispersion forces cannot be considered a hydrogen bond[75]. The main attractive components correspond to electrostatic and delocalization energies, and their ratio changes with strength and distance of the interaction[76]. Stronger interactions have shorter distances and are characterized by major contributions from delocalization energy, composed by the charge transfer and induction terms mentioned, while weaker HBs are mainly electrostatic[76]. The attractive components can be enhanced or reduced in resonance-assisted HBs, where π-conjugation leads to a redistribution of the ED[80, 81], and charge-assisted HBs, where the donor bears a positive charge or the acceptor a negative one[82]. A factor that is also distinctive in HBs is the correlation of the pK_a

of $D-H$ and the pK_b of $A-X$ with the strength of the interaction[75, 77]. Indeed, the interactions in which these dissociation constants display similar values are commonly designated low-barrier HBs and are very strong[83, 84]. Low-barrier HBs represent a class of bonds where the proton is partially shared by D and A with a low barrier height for proton-transfer[84-86]. Proton-transfer reaction is very representative of HBs as they can be considered a transition state for transfer in many cases[75]. In systems where HBs form a network, their individual strength can be increased or decreased in relation to the isolated case, an effect called cooperativity, which has been suggested to arise from electrostatic forces[78, 87].

IR and NMR spectroscopy are very useful in detecting HBs experimentally. Theoretical methods can further assist the analysis, particularly, the QTAIM method can evaluate the ED topology of the HB calculated with a quantum-mechanical method[77]. The lengthening of the $D-H$ bond generally increases, resulting in a red-shift of the stretching frequency and increase in IR spectral intensity and bandwidth, with some exceptions displaying blue-shifts[75, 77]. As the electron distribution around the proton in the HB is altered, there is also a downfield chemical shift of $D-H$ in the NMR spectra in virtue of the stronger deshielding of the proton[75, 77]. For HBs where the energetic potential barriers for bond breaking are surpassed by the thermal vibrational energy, experimental observation might not be possible, thus the thermal energy needs to be lower than the Gibbs energy for bond formation, as both entropy and enthalpy variations need to be accounted for[77]. There is also the possibility of the solvent to act as a competitor for hydrogen bonding, weakening or even disrupting solvent-exposed interactions[88, 89].

Chapter II

Methodology

"All other corpses may very well be illusion.

All the dead may be alive somewhere else,

All my own past moments may be existing somewhere

In the illusion of space and time,

In the fallibility of elapsing."

Fernando Pessoa, Poesia de Álvaro de Campos (1944)

1. Quantum Theory

In the late 1920's, the peculiar nature of electrons was extensively dissected, leading to the strange conclusion that these must behave as both wave and particle, the wave-particle duality. The De Broglie wavelength equation (Eq. 14) hypothesizes that electrons are waves with an associated wavelength λ that is inversely related to the particle's momentum p [90-92].

$$\lambda = \frac{h}{p} = \frac{h}{mv} \tag{14}$$

The famous double slit experiment can be interpreted using this concept. It consists of a wave source emitting in the direction of a barrier with two small slits, where diffraction phenomena occur as the waves pass through the slits, producing waves that overlap with each other in some regions[90]. At these regions they experience constructive and destructive interference depending if they are in phase or out of phase, respectively, a behavior that seems present in all wave-like disturbances[90, 92]. This experiment was demonstrated for photons, but also for small particles of matter (e.g. electrons, buckyballs), thus successfully confirming its wave-like behavior[90, 92].

In consonance with quantum mechanics, an object displaying wave-particle duality passes through both slits at the same time, traveling through the medium as a wave that interferes with itself on the other side of the barrier and collapses to a particle when it hits a detector[90]. Increasing the number of objects passing through the slits originates an interference pattern, that is described as a series of smooth band-like regions fading away from the middle, matching the regions where the waves don't cancel each other out[90]. So, the pattern can be interpreted as the probabilistic distribution of the locations where the waves collapse into particles[90].

When another detector is placed near one of the slits to verify through which the particles passes, there is evidence that the particles only travel through one of the holes, however, the interference pattern detected is gone and the result is just what you would expect for a classical particle[90]. One way to look at this is the Copenhagen interpretation, which explains that a quantum object travels through space as a probabilistic superposition of states when there is no observer, and the act of observation brings the wave-function collapse, resulting in the particle appearing at a certain location[92].

Heisenberg explained this in 1927 through the uncertainty principle, which establishes a limit for the precision in the measurement of a particle's complementary variables, such as position x and momentum p (Eq. 15) [90, 91, 93, 94]. The uncertainty principle traduces to a simple formulation, the more accurately you can determine a quantum particle's position, the less accurately you can measure its momentum.

$$\Delta x \Delta p \geq \frac{\hbar}{2} \tag{15}$$

1.1 Quantum Mechanics

Quantum theory reached a climax when Erwin Schrödinger postulated the famous Schrodinger wave equation, a mathematical model that describes the tridimensional wave function of a quantum system. This equation meant quite the revolution for theoretical physics, because it provided a new physical framework for electronic motions. This section aims to briefly detail the mathematical foundation for quantum mechanics, which exists as a set of postulates:

Postulate I:

Any given state of a physical system is determined by a wave function $\Psi(r_1, r_2, \dots, r_{3n,} \omega_1, \omega_2, \dots, \omega_n, t)$, that depends on three spatial coordinates (r_x, r_y, r_z) and one spin variable (ω) for any of the n electrons, also having time (t) dependency[90, 92, 94-96]. If Ψ is normalized, $\Psi^* \Psi \ dt$ gives the probability density of the particles in the respective volume element $d_\tau (\equiv d_{\tau 1}, d_{\tau 2}, \dots, d_{\tau n})$, at time t, thus Ψ represents a probability amplitude[90, 92, 94-96].

Postulate II:

To every observable A of a physical system (e.g. position, momentum, kinetic energy, potential energy) there is a correspondent linear Hermitian operator $\hat{A}$ [90-92, 96].

Postulate III:

The wave function evolves in time according to the time-dependent Schrödinger equation, where $\widehat{H}$ is the Hamiltonian operator giving the eigenvalue for the total energy of the system (Eq. 16) [90-92, 96].

$$\widehat{H}\Psi(r,t) = \frac{-\hbar}{i}\frac{\partial}{\partial t}\Psi(r,t) \tag{16}$$

Postulate IV:

The measurement of A over an eigenstate gives one of the eigenvalues a from the operator $\hat{A}$ (Eq. 17) [90-92, 96].

$$\hat{A}\Psi(r,t) = a\Psi(r,t) \tag{17}$$

Postulate V:

The average value for the measured A associated with the wave function Ψ [90-92, 96] is given by:

$$< A >= \int_{-\infty}^{\infty} \Psi^{*}\hat{A}\Psi d_{\tau} \tag{18}$$

Postulate VI:

The wave function Ψ is antisymmetric for the exchange of coordinates between identical fermions[90-92, 96].

The Hamiltonian operator $\hat{H}$ of a system composed by M nuclei and N electrons can be written as:

$$\hat{H} = -\frac{1}{2}\sum_{i=1}^{N} \nabla_i^2 - \frac{1}{2}\sum_{A=1}^{M} \frac{1}{M_A}\nabla_A^2 - \sum_{i=1}^{N}\sum_{A=1}^{M} \frac{Z_A}{r_{iA}} + \sum_{i=1}^{N}\sum_{j>i}^{N} \frac{1}{r_{ij}} + \sum_{A=1}^{M}\sum_{B>A}^{M} \frac{Z_A Z_B}{R_{AB}} \tag{19}$$

, where the first two terms represent the kinetic energy of electrons and nuclei, the remainder terms represent the potential of the nucleus-electron, electron-electron and nucleus-nucleus interactions, respectively[90, 93, 95, 96].

Following the Born-Oppenheimer approximation, as the electrons are massless relative to nuclei, the electrons move much faster than nuclei, so they rearrange instantly around the nuclei when there are nuclear motions[90, 92, 94-96]. This approximation considers the nuclei to be fixed in space, and thus the kinetic energy from the nuclei is zero and the potential from nuclear-nuclear interactions is constant[90, 92, 94-96], and the electronic Hamiltonian is then simplified to:

$$\hat{H}_{electronic} = -\frac{1}{2}\sum_{i=1}^{N} \nabla_i^2 - \sum_{i=1}^{N}\sum_{A=1}^{M} \frac{Z_A}{r_{iA}} + \sum_{i=1}^{N}\sum_{j>i}^{N} \frac{1}{r_{ij}} \tag{20}$$

And total energy in the system is calculated as:

$$E_{total} = E_{electronic} + E_{nuclear} \tag{21}$$

Simplification of the Hamiltonian to this form makes it easier to calculate the energy of the system, because it is defined only by nuclear positions, atomic numbers, and the number of electrons. However, the wave function that corresponds to the ground state is still unknown and the lowest energy state cannot be calculated without it. The variational principle allows to minimize the energy of the system using trial wave functions, in order to approximate the energy of the ground state (Eq. 22) [90, 95, 96]. Thus, each time a trial wave function lowers the energy, it becomes closer to the ground state wave function that gives the lowest energetic state.

$$\int \Psi_t{}^{*} \hat{H} \Psi_t d\tau \geq E_0 \tag{22}$$

2. Quantum Chemistry

The study of electronic structure of molecules provides theoretical chemists a great deal of information on the chemical properties of any system (e. g. dipole moment, charge distribution, potential energy surface). Accordingly, the accurate description of electrons in atoms or molecules is needed to theoretically explain chemical phenomena such as covalent and non-covalent bonding.

"The underlying physical laws necessary for the mathematical theory of a large part of physics and the whole of chemistry are thus completely known, and the difficulty is only that the exact application of these laws leads to equations much too complicated to be soluble. It therefore becomes desirable that approximate practical methods of applying quantum mechanics should be developed, which can lead to an explanation of the main features of complex atomic systems without too much computation."

Dirac, P. Quantum Mechanics of Many-Electron Systems. Proceedings of the Royal Society A: Mathematical, Physical and Engineering Sciences 1929, 123, 714-733.

The so-called many-body problem can be ascribed to the inability to analytically solve the Schrödinger equation for quantum mechanical systems containing a high number of interacting particles[97]. The resulting response to this many-body problem is adequately portrayed in the last sentence of the above citation, it originated the emergence of distinct approaches that enable efficient approximations on quantum mechanical behavior. Indeed, the modern computational chemist has at his disposal robust quantum mechanical methods based on different approaches that allow to retrieve information for almost any type of chemical system. The purpose of such studies is to theoretically predict the occurrence of phenomena that are difficult to research via experimental techniques, assisting experimental research in complementing the results or correcting misinterpretations of such phenomena, and therefore both factions need to be in constant dialectic. Depending on the physical basis adopted, quantum mechanical approximation methods fit into two separate categories: approaches based on the wave function and approaches based on density functional theory.

Ab initio calculations are methods based on the wave function that employ rigorous approximations to provide a more exact solution to the non-relativistic Schrödinger equation[93, 94, 96]. This approach is designated *ab initio* considering that is solely based on theoretical physics principles and fundamental physical constants, thus there is no requirement for empirical parameters[93, 94, 96]. *Ab initio* methods produce more accurate results, however the complexity associated with the calculations bears heavy computational costs and limits the size of the system[93, 94, 96].

Semi-empirical methods, also based on the wave function, employ several approximations as well as experimental parameters that speed up the calculations[93, 94, 96]. Subsequently, semi-empirical calculations can effectively handle larger systems, however, they cannot yield very accurate results unless the system is composed by molecules analogous to the ones used for parametrization[93, 94, 96].

Unlike the mentioned above, density functional theory calculations are based on the ED rather than the wave functions, which allows for accuracy comparable to that of *Ab initio* and application to larger systems, as result of shorter calculation times[97, 98].

2.1 Density Functional Theory

Considering that the wave function is an uninterpretable and complicated mathematical object that depends on 4N variables (i.e. three spatial and one spin variables for N electrons), for the sake of simplifying the complex mathematics from wave function theory, the Hamiltonian can be constructed using a physical observable[95-97]. The most useful physical observable is the ED, because it is a scalar field and essentiality all the information of interest for a chemical system is contained in it[95, 96]. From the probabilistic interpretation of the wave function, the ED is the relative probability of finding any electron within a given volume element regardless of the position of other electrons (Eq. 23) [95, 96].

$$\rho(r) = N \int \cdots \int \Psi\ (r, x_2, \cdots, x_N) \Psi(r, x_2, \cdots, x_N) dx_2 \cdots dx_N \qquad (23)$$

When the ED is integrated over all space, it gives the total number of electrons (Eq. 24) [95, 96]. Furthermore, it is also possible to determine the atomic numbers of the nuclei using the ED, since the physical observable is at a local maximum in the positions of the point charges that correspond to the nuclei and decays from there (Eq. 25) [95, 96]. Thus, the Hamiltonian for the system can be totally defined based on the ED, as it depends only on the positions and charges of the nuclei and the number of electrons[93, 95, 96].

$$N = \int \rho(r) dr \qquad (24)$$

$$\left. \frac{\partial \bar{\rho}(r_A)}{\partial r_A} \right|_{r_A = 0} = -2 Z_A \rho(r_A) \qquad (25)$$

2.1.1 Hohenberg-Kohn Theorems

In 1964, Hohenberg and Kohn published a paper that had the intend to establish the rigorous foundation for DFT, devising two theorems for this purpose.

Theorem I

As the electrons interact with an external potential that matches the nuclear attraction, the theorem declares:

"the external potential $V_{ext}(r)$ is (to within a constant) a unique functional of $\rho(r)$; since, in turn $V_{ext}(r)$ fixes $\widehat{H}$ we see that the full many particle ground state is a unique functional of $\rho(r)$."

It is proven via *reductio ad absurdum*, leading to the conclusion that it is impossible for two different external potentials to be associated with the same ground state ED[95, 96, 99]:

$$E_{0,a} < \langle \Psi_{0,b} | H_a | \Psi_{0,b} \rangle \tag{26}$$

This means the ground state density uniquely determines the external potential and proves that there is a mapping between the density and the wave function, so the ED must hold all properties for the ground and excited states of the system[95, 96, 99]. As the ground state energy is a functional of the density, the individual components (i.e. kinetic energy, electron-electron and nuclear-electron interaction) can be separated into a part that is system dependent (i.e. nuclear-electron interaction potential) and a part that is independent of the number of electrons, the positions of the nuclei and the nuclear charges (i.e. kinetic energy of electrons and electron-electron interaction potential) (Eq. 27) [93, 95, 96, 99].

$$E_0[\rho_0] = \int \rho_0(\vec{r}) V_{Ne} d\vec{r} + F_{HK}[\rho_0] \tag{27}$$

In this context, the Hohenberg-Kohn functional is a function of the ground state ED that gives the exact value for the kinetic energy of electrons and the potential for electron-electron interactions, however its specific form is unknown[95, 96, 99].

Theorem II

The theorem declares that the density obeys a variational principal. Thus, only the density that minimizes the ground state energy of the system, by means of the Hohenberg-Kohn functional, can be considered the true ground state ED[95, 96, 99]. Any trial density that integrates to the correct number of electrons and is associated with a certain external potential (i.e. V-representable), will give an energy value that is greater than the ground state energy, unless this trial input is equal to the ground state ED (Eq. 28) [95, 96, 99].

$$\left\langle \Psi_{trial} \middle| \hat{H} \middle| \Psi_{trial} \right\rangle = E[\rho_{trial}] \geq E_0[\rho_0] = \left\langle \Psi_0 \middle| \hat{H} \middle| \Psi_0 \right\rangle \tag{28}$$

Minimizing the energy allows to search for the ground state ED, but on the other hand there is no rational basis to improve trial densities and to calculate the energy one must know the Hohenberg-Kohn functional[95, 96, 99].

2.1.2 Kohn-Sham DFT

Returning to the Hohenberg-Kohn functional, it is defined by the following contributions:

$$F_{HK}[\rho(\vec{r})] = T[\rho(\vec{r})] + J[\rho(\vec{r})] + E_{nc}[\rho(\vec{r})] \tag{29}$$

, where J is the classical Coulomb interaction, T is the kinetic energy, and E_{nc} is the non-classical part, composed by the self-interaction correction, exchange and correlation effects[95, 97]. As $T[\rho(\vec{r})]$ and $E_{nc}[\rho(\vec{r})]$ have no explicit form, Kohn and Sham proposed to use a fictitious non-interacting system of N particles to calculate some fraction of T[93, 95, 96].The ground state of such system is a single Slater determinant, so that the $\rho_s(\vec{r})$ constructed from the Kohn-Sham orbitals corresponds to the actual $\rho_0(\vec{r})$ from the real interacting system[93, 95, 96]:

$$\rho_s(\vec{r}) = \sum_{i}^{N} \sum_{s} |\phi_i(\vec{r}, s)|^2 = \rho_0(\vec{r}) \tag{30}$$

The Hohenberg-Kohn functional can then be written as:

$$F_{HK}[\rho(\vec{r})] = T_s[\rho(\vec{r})] + J[\rho(\vec{r})] + E_{xc}[\rho(\vec{r})] \tag{31}$$

$$T_s = -\frac{1}{2} \sum_{i}^{N} \langle \phi_i | \nabla^2 | \phi_i \rangle \tag{32}$$

$$E_{xc}[\rho] = T_C[\rho] + E_{nc}[\rho] \tag{33}$$

, where T_s is the kinetic energy for a non-interacting system, J is the classical Coulomb interaction and E_{xc} is the exchange-correlation energy[95, 96]. Thus, the unknown part of the functional is now reduced to $E_{xc}[\rho]$, containing the rest of the kinetic energy and the non-classical contributions from electron-electron interaction[93, 95, 97].

The expression for the energy of the real system can be constructed using the KS orbitals[95, 97]:

$$\begin{aligned} E[\rho(\vec{r})] = -\frac{1}{2}\sum_{i}^{N}\langle\phi_i|\nabla^2|\phi_i\rangle + \frac{1}{2}\sum_{i}^{N}\sum_{j}^{N}\iint |\phi_i(\vec{r}_1)|^2\frac{1}{r_{12}}|\phi_i(\vec{r}_2)|^2 d\vec{r}_1 d\vec{r}_2 \\ + E_{xc}[\rho(\vec{r})] - \sum_{i}^{N}\int\sum_{A}^{M}\frac{Z_A}{r_{1A}}|\phi_i(\vec{r}_1)|d\vec{r}_1 \end{aligned} \tag{34}$$

Then, application of the variational principle aims to find the orbitals that minimize the energy, leading to the Kohn-Sham equations, where $\hat{f}^{KS}$ is the Kohn-Sham one-electron operator[95, 96]:

$$\hat{f}^{KS}\phi_i = \varepsilon_i\phi_i \tag{35}$$

$$\hat{f}^{KS} = -\frac{1}{2}\nabla^2 + V_s(\vec{r}) \tag{36}$$

$$V_s(\vec{r}) = \int\frac{\rho(\vec{r}_2)}{r_{12}}d\vec{r}_2 + V_{XC}(\vec{r}_1) - \sum_{A}^{M}\frac{Z_A}{r_{1A}} \tag{37}$$

$$V_{xc} = \frac{\delta E_{xc}}{\delta\rho} \tag{38}$$

Hence, if $V_s(\vec{r})$ is known, then the KS orbitals are obtained by solving the one-electron equations correspondent to the non-interacting system, subsequently the true ground state ED and ground state energy can be found in a self-consistent field procedure[95, 96]. However, V_{xc} corresponds to the functional derivative of E_{xc}, which has an unknown form and needs to be approximated[95, 96].

2.1.3 Exchange-Correlation Functionals

The functional $E_{xc}[\rho]$ accounts for the energetic contributions from the difference between classical and quantum mechanical electron-electron repulsion E_{nc}, and the difference between the kinetic energy from a non-interacting system and an interacting system T_C[93, 95, 96]. If the correct expression for this functional was known, DFT would allow to compute the exact energy for any given quantum mechanical system, therefore the accuracy of the method depends on the approximation made to the functional $E_{xc}[\rho]$[93, 95, 96]. Although the T_C correction is accounted in some functionals, other functionals omit the term or add empirical parameters which include the T_C corrections from experimental data[93, 95, 96].

The simplest approximation to $E_{xc}[\rho]$ is the local density approximation (LDA), where E_{xc} is attained through the uniform electron gas model (Eq. 39) [95, 96]. $E_{xc}[\rho]$ is expressed as the local interaction between ρ and an energy density ε_{XC} term, which can be further split into exchange ε_X and correlation ε_C contributions (Eq. 40) [95, 96].

$$E_{XC}^{LDA}[\rho] = \int \rho(\vec{r})\varepsilon_{XC}\big(\rho(\vec{r})\big)d\vec{r} \tag{39}$$

$$\varepsilon_{XC}\big(\rho(\vec{r})\big) = \varepsilon_X\big(\rho(\vec{r})\big) + \varepsilon_C\big(\rho(\vec{r})\big) \tag{40}$$

For this functional, the exchange energy is exact and corresponds to the Slater exchange from the uniform electron gas, while the correlation term has no explicit form and it was estimated from quantum Monte Carlo simulations of the uniform electron gas model[93, 95, 96]. The simplicity introduced in this functional is useful for idealized cases of solid-state physics but fails when it comes to systems where the ED isn't distributed uniformly[93, 95, 96].

Introducing the concept of spin density in this functional allows the application to open-shell systems and benefits in terms of accuracy, the so called the local spin-density approximation (LSDA)[93, 95, 96, 100]:

$$E_{XC}^{LSDA}[\rho_\alpha, \rho_\beta] = \int \rho(\vec{r})\varepsilon_{XC}\left(\rho_\alpha(\vec{r}), \rho_\beta(\vec{r})\right)d\vec{r} \tag{41}$$

Improvements to this type of functionals is accomplished by introducing a dependency that includes not only the local density, but also the gradient of the density to account for the non-uniform character of the ED[93, 95, 96]. Another correction is introduced relatively to the Fermi and Coulomb holes, being required to be integrated to -1 and 0, respectively[93, 95]. The addition of such corrections results in functionals that are typically designated gradient generalized approximations (GGA)[93, 95, 96, 100]:

$$E_{XC}^{GGA}[\rho_\alpha, \rho_\beta] = \int f\big(\rho_\alpha, \rho_\beta, \nabla\rho_\alpha, \nabla\rho_\beta\big)d\vec{r} \tag{42}$$

Further improvements to GGA functionals include a dependency on the Laplacian of ED and the orbital kinetic energy density as well, generating the meta-GGA functionals[93, 96, 100]:

$$E_{XC}^{MGGA}[\rho_\alpha, \rho_\beta] = \int f\big(\rho_\alpha, \rho_\beta, \nabla\rho_\alpha, \nabla\rho_\beta, \nabla^2\rho_\alpha, \nabla^2\rho_\beta, \tau_\alpha, \tau_\beta\big)d\vec{r} \tag{43}$$

A more accurate generation, the hybrid functionals, apply the calculation of the exact exchange energy from Hartree-Fock theory as a portion of the exchange-correlation energy, while the rest is treated with a DFT-based functional (Eq. 44) [93, 95, 96, 100]. The mixing ratio given by a is usually optimized through the fitting to some reference set of parameters[93, 95, 96].

$$E_{XC}^{hybrid} = (1-a)E_{XC}^{DFT} + aE_X^{HF} \tag{44}$$

In the current project, three different functionals were chosen and compared according to their accuracy for describing the types of interactions that are present in the carbon nanotube models: the PBE0, the B3LYP and the M06-2X functionals. PBE0 is a GGA hybrid functional that calculates the exchange energy as 25% of the Hartree-Fock exchange and 75% of the PBE exchange functional, while the correlation energy is given by the PBE correlation functional[100, 101]:

$$E_{XC}^{PBE0} = E_C^{PBE} + \frac{1}{4}(E_X^{HF} - E_X^{PBE}) \tag{45}$$

B3LYP is also a GGA hybrid functional, that employs three parameters to mix the Hartree-Fock exchange with the LDSA exchange, the LYP GGA correlation functional with the LSDA correlation functional, and the additional contribution from the B88 GGA exchange functional[93, 95-97, 100]:

$$E_{XC}^{B3LYP} = (1-a)E_X^{LSDA} + aE_X^{HF} + b\Delta E_X^B + (1-c)E_C^{LSDA} + cE_C^{LYP} \tag{46}$$

M06-2X is a meta-GGA hybrid functional belonging to the M06 suite, that incorporates 54% of Hartree-Fock exchange and combines the PBE exchange functional with the B97 correlation functional, as well as employing several semiempirical parameters[100, 102]:

$$E_{XC}^{M06} = \frac{X}{100}E_X^{HF} + \left(1 - \frac{X}{100}\right)E_X^{DFT} + E_C^{DFT} \tag{47}$$

Although PBE0 and B3LYP have been used extensively in publications[103, 104], they are outperformed by M06-2X when tested against several databases that include non-covalent interactions, such as HBs and dispersion interactions[100, 102, 105].

2.1.4 Basis Sets

Another major approximation that determines the accuracy of the DFT method is the basis set[93] [95, 96]. The basis sets are finite series of mathematical functions that are used in constructing the wave function of a system, where each molecular orbital is expressed as a linear combination of basis functions (Eq. 48) [95, 96].

$$\phi = \sum_{\alpha=1}^{M} c_\alpha \chi_\alpha \tag{48}$$

If the basis set were to have an infinite number of basis functions, it would be complete and this case would not constitute an approximation, yet this is impossible to implement[93] [95, 96]. Thus, smaller basis set harbor less accuracy, but the type of functions that are present in the basis set also influence the accuracy[93, 95, 96]. Considering computational efficiency, the ideal basis set should have a minimum number of functions possible to allow for quick calculations, if not the functions should be simple enough for the same purpose, and importantly they should reproduce useful results in terms of chemical interpretation[95, 96].

The basis functions fall in two categories: Slater type orbitals (STO) and Gaussian type orbitals (GTO) [93, 95, 96]. STOs were the first to be developed and they are characterized by having an exponential dependence on the nucleus-electron distance that exactly mirrors the hydrogen atom orbitals (Eq. 49) [93, 95, 96]. Nonetheless, the use of STOs in molecular systems is severely limited by the resulting three- and four-center two-electron integrals that are analytically unsolvable[93, 95, 96]. GTOs bypass this limitation by applying a r^2 exponential decay instead of the r present in STOs (Eq. 50) [93, 95, 96].

$$\chi_{\xi,n,l,m}(r,\theta,\varphi) = NY_{l,m}(\theta,\varphi)r^{n-1}e^{-\xi r} \tag{49}$$

$$\chi_{\xi,n,l,m}(r,\theta,\varphi) = NY_{l,m}(\theta,\varphi)r^{2n-2-l}e^{-\xi r^2} \tag{50}$$

The r^2 exponential dependence of GTOs results in a poor representation relative to STOs[93, 95, 96]. Nevertheless, the computation of the integrals is easier, so the number of GTOs can be increased in a linear combination to retrieve the accuracy one obtains with STOs, ensuing a more efficient mathematical process[93, 95, 96]. In this case the resulting basis function is labeled a contracted function and the individual GTOs of the linear combination are called primitive functions, accordingly, the contracted functions can be classified by the number of primitive functions used to form the STO[95, 96].

The STO-3G is a contracted basis function of three GTOs and is considered a single-ζ basis set, because it has only one basis function for each orbital, while double-ζ have two basis functions for each orbital and so on for higher multiple-ζ[93, 95, 96]. As valence orbitals are greatly influenced by bonding phenomena relatively to core orbitals, split-valence basis sets employ a single contracted basis function for core orbitals and higher number of basis functions for valence orbitals[93, 95, 96].

The widely used split-valence Pople basis sets have the form k-nlmG, where k is the number of primitives in the contracted functions for the core orbitals and nml represents the number of basis functions for valence orbitals, having the form nl for valence-double-ζ and nlm for valence-triple-ζ[93, 95, 96]. The 3-21G basis set has a contracted function of three GTO primitives representing the core orbitals, while the valence orbitals are represented by a contraction of two GTO primitives at their inner part and only one primitive gaussian at the outer part[93, 95, 96]. The 6-31G basis set employs a contracted function of six GTO primitives for core orbitals, a contracted function of three GTO primitives for the inner part of valence orbitals and one GTO primitive for the outer part[93, 95, 96].

For cases where the molecular structure presents polarization phenomena in bonding, the mathematical flexibility provided by GTOs to describe valence orbitals is not enough, requiring higher angular momentum functions[93, 95, 96]. These functions are called polarization functions and their notation appears after the G, referring which functions are added[93, 95, 96]. For example, in the 6-31G(d) basis set, d functions are added to polarize the p functions that are present in heavy atoms, and in the 6-31G(d,p) basis set, besides the later, p functions are added to polarize the s functions that are present in hydrogen atoms[93, 95, 96].

Furthermore, for situations where the electrons are loosely bound, such as anions or excited states, diffuse functions are required to augment the basis set[93, 95, 96, 106]. The notation of diffuse functions appears before the G as + or ++, if small exponent functions are added to heavy atoms or heavy atoms and hydrogen atoms, respectively, thus providing electron flexibility at longer distances[93, 95, 96, 107].

As these additional functions result in slower calculations, employing them in large systems is very time consuming[95], therefore the same level different basis (SLDB) approach is desirable, where important molecular features are treated with a larger basis set and the rest with a smaller basis set[108].

2.2 Solvation Models

The electronic structure calculations described until this point consider molecules as isolated chemical entities, however, this approach is severely limited when it comes to systems where the surrounding environment deeply impacts the properties of the system. To overcome the limitations of this approximation, solvation models can be employed in order to simulate the effect of solvent around a solute which constitutes the object of study. There are essentially two main categories of solvation models: explicit solvation, where solvent molecules are added to the system and treated individually, and implicit solvation, where the solvent is treated as a continuous medium[93, 94, 96]. Furthermore, the models can be classified in relation to the physical basis adopted to describe solvent-solute interactions and can be combined so that the system has one or more explicit solvation shells, while the rest of the environment is treated implicitly[93].

Implicit solvation models aim to replace the explicit solvent molecules needed to accurately describe the solvation process with a uniform polarizable medium associated with some dielectric constant, that can replicate the perturbations that a given solvent introduces in a gas phase system[93, 94, 96]. The free energy of solvation ΔG_s^0 is the central quantity that describes the solvent-solute interaction, corresponding to the free energy variation associated with changing from the gas phase to a condensed phase[93, 96, 109]. This quantity can be decomposed as follows:

$$\Delta G_s^0 = \Delta G_{ENP} + \Delta G_{CDS} + \Delta G_{conc}^0 \tag{51}$$

The term ΔG_{ENP} refers to the electronic, nuclear and polarization components, while the term ΔG_{CDS} refers to the cavitation, dispersion and solvent structure components of the free energy, and ΔG_{conc}^0 refers to the change in concentration which is taken to be zero in electronic structure calculations[109]. The implicit solvation models consider this type of energy decomposition, and the variation between models occurs at the definition of the ΔG_{ENP} and ΔG_{CDS} terms[109].

The nuclear part of the ΔG_{ENP} term is related to the energy difference from structural variation between gas and liquid phase, and thus can be neglected if the geometry remains similar[109]. The electronic and polarization contribution ΔG_{EP} is obtained from a molecular orbital self-consistent reaction field calculation, according to the solution of the nonhomogeneous Poisson equation (NPE) and is associated with the long range electrostatic and polarization effects[93, 109]. On the other hand, the ΔG_{CDS} term consists in the short-range polarization effects and short-range non-electrostatic effects such as cavitation, due to the cavity created in the medium where the solvent is placed, dispersion interactions and solvent structural effects, such as hydrogen bonds and exchange repulsion[109].

The SMD model used in this study is based on the polarized continuous quantum mechanical charge density of the solute, employing the IEF-PCM protocol to solve the NPE in order to compute the ΔG_{EP} term[109]. The cavity is created from a superposition of nuclear-centered spheres of radii equivalent to the intrinsic Coulomb radii, which depend on atomic number and have been carefully optimized[109]. In addition, it employs other parameters that also have been optimized using electronic structure calculations, the atomic surface tension coefficients, for the calculation of the ΔG_{CDS} term[109].

To make estimates on the acid dissociation constant pK_a of the functionalizations, considering the proton dissociation presented in Eq. 52 [110], the free energy difference ΔG_{aq} was calculated from the aqueous Gibbs free energy of the acids and conjugate bases (Eq. 53) [110], where $G_{aq}(H^+)$= -265.9 kcal.mol^{-1} [110, 111], and the pK_a calculated from Eq. 54 [110, 111]. For the pK_{an} values of the functionalizations, the conjugated bases of the first deprotonations were the acids of the second deprotonations and so on.

$$AH(aq) \xrightarrow{\Delta G_{aq}} A^-(aq) + H^+(aq) \tag{52}$$

$$\Delta G_{aq} = G_{aq}(A^-) + G_{aq}(H^+) - G_{aq}(AH) \tag{53}$$

$$pK_a = \frac{\Delta G_{aq}}{RTln(10)} \tag{54}$$

2.3 Quantum Chemical Topology

Through the topological analysis of real space functions dependent on the ED, it is possible to obtain useful chemical information about a system. In the current study, this analysis is of great value because there is interest in studying non-covalent bonding, which can be extensively characterized by evaluating some real functions of the ED on the spatial region of the interactions.

2.3.1 Quantum Theory of Atoms in Molecules

The quantum theory of atoms in molecules aims to explain the molecular structure of a system as a set of atom-atom interactions, such as covalent bonding and other types of non-covalent interactions that originate from the ED spatial distribution around the atomic nuclei[76, 112]. As the nuclei determine the local maxima for the ED, which then decays, the boundary of an atom is defined by the balance of forces that neighboring atoms apply on the electrons[76, 112, 113]. The interaction between atoms implies a change in the decay of the ED comparatively to the isolated case, that can be useful in defining and characterizing the interactions. Thus, because the ED is a scalar function, the topological analysis consists in detecting such phenomena through the vector gradient field of the ED $\nabla\rho(r)$[76, 112].

As follows the spatial coordinates where all the first derivatives contained in $\nabla\rho(r)$ are equal to zero represent critical points (CPs), corresponding to local maxima, local minima or saddle points in the ED[76, 112]. To distinguish between them, the second derivatives of the ED are considered. A 3×3 matrix of second-order partial derivatives of the ED at the CP constitutes the Hessian matrix[76, 112]:

$$A(r_c) = \begin{pmatrix} \frac{\partial^2\rho}{\partial x^2} & \frac{\partial^2\rho}{\partial x\partial y} & \frac{\partial^2\rho}{\partial x\partial z} \\ \frac{\partial^2\rho}{\partial y\partial x} & \frac{\partial^2\rho}{\partial y^2} & \frac{\partial^2\rho}{\partial y\partial z} \\ \frac{\partial^2\rho}{\partial z\partial x} & \frac{\partial^2\rho}{\partial z\partial y} & \frac{\partial^2\rho}{\partial z^2} \end{pmatrix}_{r=r_c} \qquad (55)$$

The diagonalization of the Hessian matrix through a unitary transformation rotates the coordinate system $r(x, y, z) \rightarrow r(x', y', z')$, and results in its diagonal form[76, 112]:

$$\Lambda(r_c) = \begin{pmatrix} \frac{\partial^2 \rho}{\partial x'^2} & 0 & 0 \\ 0 & \frac{\partial^2 \rho}{\partial y'^2} & 0 \\ 0 & 0 & \frac{\partial^2 \rho}{\partial z'^2} \end{pmatrix}_{r\prime = r_c} = \begin{pmatrix} \lambda_1 & 0 & 0 \\ 0 & \lambda_2 & 0 \\ 0 & 0 & \lambda_3 \end{pmatrix} \tag{56}$$

The diagonal elements λ_1, λ_2 and λ_3 are called the eigenvalues of the Hessian matrix and their sum represents the Laplacian of the ED (Eq. 57) [76, 112, 113].

$$\nabla^2 \rho(r) = \lambda_1 + \lambda_2 + \lambda_3 \tag{57}$$

CPs are classified according to the nature of these eigenvalues, although only CPs with three non-zero eigenvalues are considered to be stable enough to resist density perturbations from nuclear motions[76, 112]. CPs fall into the following categories:

- (3,-3) – nuclear critical point (NCP), having three negative eigenvalues corresponds to local maxima in the density and is associated with nuclear positions.
- (3,-1) – bond critical point (BCP), having two negative eigenvalue corresponds to second-order saddle points and are associated with bonding interactions between atoms.
- (3,+1) – ring critical point (RCP), having two positive eigenvalues corresponds to first-order saddle points and is associated with steric interactions and the center of cyclic molecules.
- (3,+3) – cage critical point (CCP), having three positive eigenvalues corresponds to local minima and is associated with the presence of ring motifs in a structure that encloses a portion of space without the ED.

The number of CPs of an isolated molecule obeys the Poincaré–Hopf relationship:

$$n_{NCP} - n_{BCP} + n_{RCP} - n_{CCP} = 1 \tag{58}$$

The path linking the NCPs of two bonded atoms is a line of local maxima in the ED designated bond path, and BCPs coincide with the ED minimum in the respective bond path[76, 112]. At the BCP of HBs, the analysis of $\rho(r)$, $\nabla^2 \rho(r)$ and energy density functions allow to characterize the strength of interaction[76, 112, 114, 115]. Although some HBs reach the covalent domain, covalent bonding usually displays higher ED values at the BCP, and this parameter increases with strength of interaction[76, 112, 114, 115]. $\nabla^2 \rho(r)$ is generally negative in covalent bonding and positive in hydrogen bonding, except for some cases where the reverse happens for both types of bonding[76]. The kinetic $G(r)$ and potential $V(r)$ energy densities define the total electron energy density $H(r)$ (Eq. 59) and are related to $\nabla^2\rho(r)$ (Eq. 60) [76, 112, 114, 115].

$$H(r) = G(r) + V(r) \tag{59}$$

$$\frac{1}{4}\nabla^2\rho(r) = 2G(r) + V(r) \tag{60}$$

Because $V(r) < 0$ and $G(r) > 0$, if the modulus of $V(r)$ is a greater value than $2G(r)$, then $\nabla^2\rho(r) < 0$ and $H(r) < 0$, presenting an interaction dominated by the local potential energy density that demonstrates covalent character[76, 112, 114, 115]. Having covalent nature, very strong HBs exhibit $\nabla^2\rho(r) < 0$ and $H(r) < 0$, and having partially covalent nature, strong HBs exhibit $\nabla^2\rho(r) > 0$ and $H(r) < 0$, while medium and weak HBs show $\nabla^2\rho(r) > 0$ and $H(r) > 0$, these being dominated by the local kinetic energy density[76, 112, 114, 115].

2.3.2 Non-Covalent Interactions Index

The non-covalent interactions (NCI) index is essentially a visual extension of QTAIM, as it is based on the ED and the respective derivatives, being able to provide a tridimensional visualization of non-covalent interactions. The method employs the search for spatial regions where the reduced density gradient $s(r)$ (Eq. 61) assumes low values, since $\nabla\rho(r)$ assumes values close or equal to zero, and the ED is also small in non-covalent interaction regions[116].

$$s(r) = \frac{1}{2(3\pi^2)^{\frac{1}{3}}}\frac{|\nabla\rho(r)|}{\rho(r)^{\frac{4}{3}}} \tag{61}$$

As the sign of λ_2 outlines if it is a (3,-1) or (3,+1) CP, plotting $s(r)$ against $sign[\lambda_2(r)]\rho(r)$ gives a plot with peaks reaching $s(r) = 0$ at either positive or negative values of $sign[\lambda_2(r)]\rho(r)$[113, 116]. These peaks coincide with CPs and can be ascribed to be HBs if they appear at $sign[\lambda_2(r)]\rho(r) < 0$, van der Waals interactions if they appear at $sign[\lambda_2(r)]\rho(r) \approx 0$ and steric clashes if they appear at $sign[\lambda_2(r)]\rho(r) > 0$, while the value of the ED at the peak also evaluates the strength of interaction[113, 116]. Plotting $s(r)$ at low $\rho(r)$ in tridimensional space allows to see the peaks as isosurfaces at the interaction sites[116].

2.3.3 Electron Localization Function

Another useful topology analysis to study non-covalent interactions surrounds the electron localization function (ELF), another scalar function. One can interpret the function as the local excess in kinetic energy due to Pauli repulsion, tending to 1 if the probability of finding two electrons of opposite spin in a given region of space is high, a localized pair, or tending to 0 if the probability of finding same-spin electrons in a given region is high[115, 117, 118]. The function is defined as:

$$ELF(r) = \frac{1}{1 + \chi_\sigma^2(r)} \tag{62}$$

$$\chi_\sigma(r) = \frac{D_\sigma(r)}{D_\sigma^0(r)} \tag{63}$$

, where $\chi_\sigma(r)$ (Eq. 63) is the ratio between the excess kinetic energy due to Pauli repulsion $D_\sigma(r)$ (Eq. 64) and the kinetic energy for a non-interacting uniform electron gas $D_\sigma^0(r)$ (Eq. 65) [118].

$$D_\sigma(r) = \tau_\sigma(r) - \frac{1}{4}\frac{(\nabla\rho_\sigma(r))^2}{\rho_\sigma(r)} \tag{64}$$

$$D_\sigma^0(r) = \frac{3}{5}(6\pi^2)^{\frac{2}{3}}\rho_\sigma^{\frac{5}{3}}(r) \tag{65}$$

The topological partition of tridimensional space using the ELF gradient field results in basins of attractors, which can be classified in two types: core basins $C(A)$ or valence basins $V(A)$, where A denotes the atoms to which the basins belong[117]. Core basins appear surrounding nuclei bigger than protons, while valence basins always share a boundary with at least one core basin and are classified according to the number of core basins that they share boundaries with[117].

As consequence of the electron delocalization being a major contributor to the energy of HBs, the ELF topology analysis allows to quantify the relative strength of these interactions[115, 117, 119]. Hydrogen bonds having the form $D - H \cdots A$ can have their relative strength evaluated through the core-valence bifurcation (CVB) index (Eq. 66), corresponding to the difference between $ELF_{cv}(DH)$, the value of ELF at the critical point between the basins $V(D,H)$ and $C(D)$, and $ELF_{vv}(DHA)$, the value of ELF at the critical point between the basins $V(D,H)$ and $V(A)$[115, 117, 119].

$$I_{CVB} = ELF_{cv}(DH) - ELF_{vv}(DHA) \tag{66}$$

The CVB index is negative for strong HBs and positive for weak HBs, having a good correlation with the binding energy of the interaction, $D - H$ stretching frequencies and geometrical parameters[115, 117, 119]. Besides that, $ELF_{vv}(DHA)$ can be used as a descriptor of covalency and interaction strength as well[115, 117, 119].

Chapter III

Results and Discussion

"The man who comes back through the Door in the Wall will never be quite the same as the man who went out. He will be wiser but less sure, happier but less self-satisfied, humbler in acknowledging his ignorance yet better equipped to understand the relationship of words to things, of systematic reasoning to the unfathomable mystery which it tries, forever vainly, to comprehend."

Aldous Huxley, Doors of Perception (1954)

1. Theoretical Models for Carbon Nanotubes

As discussed in Chapter I, the essential parameters needed to define a CNT model are its chirality index (n, m) and length, hence there are many conceivable systems available for study. Towards the choice of ideal SWCNT models for this study, the possible systems were initially analyzed according to a diameter criterion ($4Å \leq d \leq 8Å$), defined considering the length of the carboxylic functionalization. This allowed to explore a finite list of SWCNT with different chirality indexes that could include the carboxylic functions spatially directed to the inside of the CNT. Concerning the later, in relation to the usual end-functionalization addressed in many other studies[53, 120-124], a sp^3 C atom was added to link the carboxylic function and the SWCNT[125], so that the angle between the two is small enough to spatially position the groups for hydrogen bonding (Fig. 12a).

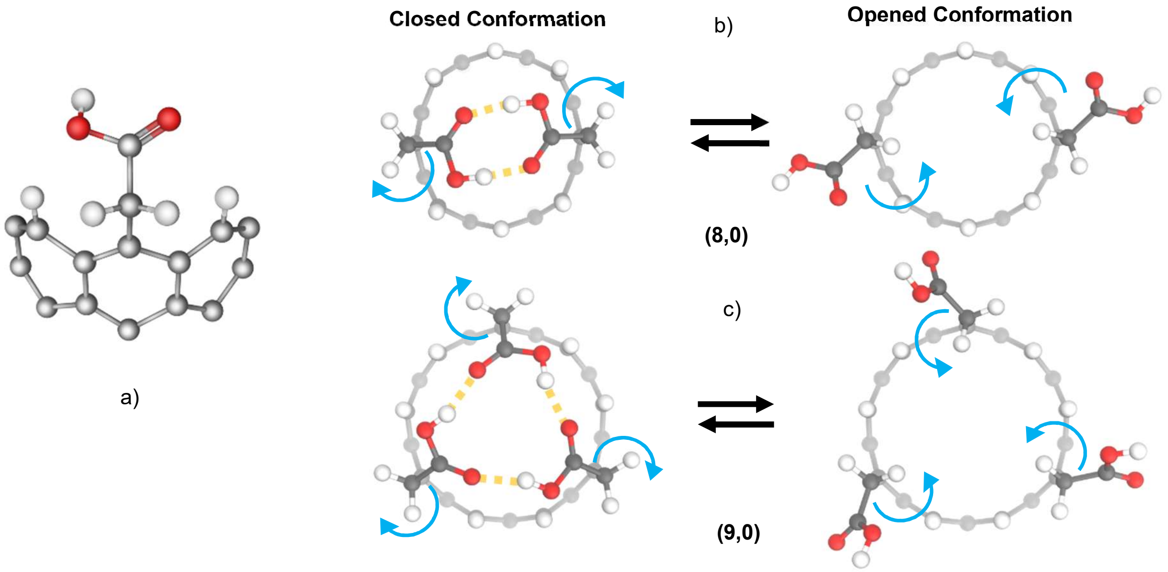

Figure 12 – Representation of the a) carboxylic functionalizations; b) bifunctionalized CNT; c) trifunctionalized CNT.

The next step was to define the systems to study according to the arrangement of terminal C atoms and their ability to harbor the functionalizations in a symmetrical manner, yielding SWCNT that could be bifunctionalized (Fig. 12b) and trifunctionalized (Fig. 12c). without distinction between the positions of the groups. As result, five types of chirality indexes were chosen to define the systems (6,0), (6,3), (8,0), (9,0) and (10,0) (Fig. 13). Notably all the chosen chiralities correspond to zig-zag CNTs, except the (6,3), which is classified as chiral. The (6,0), (8,0) and (10,0) models were found to be optimal for bifunctionalization, while the (6,3) and (9,0) for trifunctionalization (Table 1).

Figure 13 – Representation of the pristine CNTs considered in this study.

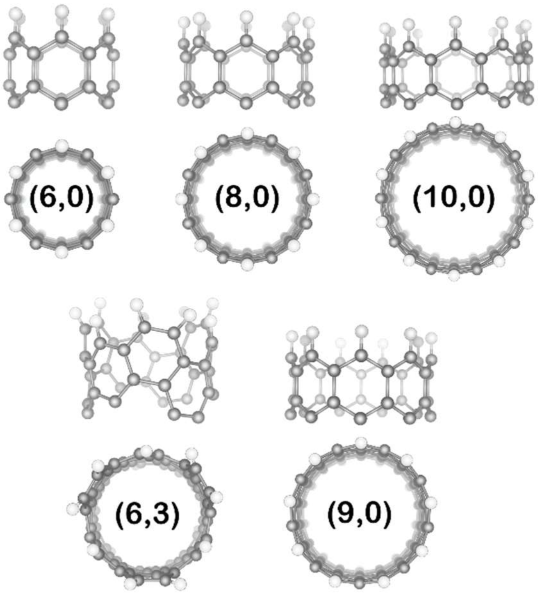

Table 1 – Characterization of SWCNT models.

(n,m)	Chirality	Diameter (Å)	Number of Terminal Carbons	Number of Functionalizations
(6,0)	Zig-zag	4,67	6	2
(6,3)	Chiral	6,18	9	3
(8,0)	Zig-zag	6,23	8	2
(9,0)	Zig-zag	7,01	9	3
(10,0)	Zig-zag	7,78	10	2

Since the sigma bonds between the CNT and the sp^3 C atom of the functionalizations have rotational freedom, two distinct conformations are hypothesized: i) a closed conformation, where the carboxyl groups are directed to the entrance of the CNT, interacting by HBs; ii) an opened conformation, where the carboxyl groups are rotated outwards, interacting with the solvent in a protonated or deprotonated state. In the protonated state, the functionalizations are predicted to oscillate between the open and closed conformations, the first being more energetically favorable by virtue of the intramolecular HBs present. Upon deprotonation, the carboxyl functions will display two equivalent oxygen atoms sharing a negative charge through resonance. Thus, it is envisioned that the functionalizations repel themselves and result in the rotation of the sigma bonds, positioning the carboxyl groups in the open conformation.

Another parameter crucial for defining the models that had to be considered is the CNT length. In various other works, this choice is analyzed because it could affect the results obtained, and so a minimum length is required to avoid this. To evaluate the dependence of our results with the increasing length, three CNTs with different number of C atoms were defined for each chirality.

The representation and characterization of chosen systems is displayed in Fig. 13 and Table 1, respectively. All SWCNT were created with TubeGen Online 3.4 (http://turin.nss.udel.edu/research/tubegenonline.html), and the functionalizations were added with Avogadro 1.2.0 Software[126]. All the dangling bonds present at the tips of the SWCNT were modelled as hydrogen atoms. The molecular representations were rendered with VMD 1.9.3 Software [127], UCSF Chimera 1.13.1 Software[128] and QuteMol 0.4.1 Software [129].

2. Methodology Benchmarking

Initially the different CNT systems were evaluated in terms of the energy difference between closed and open conformations, $\Delta E_{\text{CONFORMATIONAL}}$, applying three different functionals (B3LYP, M06-2X and PBE0), three different SLDB approaches (3-21G/6-31G, 3-21G/6-31+G(d) and 3-21G/6-31++G(d)) and considering three different CNT lengths (≈ 7, 9 and 11 Å), in order to rationally define the calculation methods for posterior studies. In this study, the SLDB approach considered treats the functionalizations and the terminal C and H atoms with a bigger basis set while a smaller basis set is employed in the rest of the CNT atoms. The functional benchmarking was performed with the SLDB 3-21G/6-31+G(d) approach, the SLDB approach benchmarking with the M06-2X functional and the CNT length benchmarking with M06-2X/3-21G/6-31+G(d). All quantum mechanical calculations were carried out with Gaussian 09 Software[130].

2.1 Functionals

The benchmarking for the functionals reveals that M06-2X gives the overall highest energy differences between conformations (Table 2). PBE0 gives higher energetic differences relative to B3LYP. The energy values from the (6,0) and (6,3) CNTs are lower for all functionals, being positive for the (6,3) CNT when evaluated with B3LYP and PBE0. The (8,0) CNT gives energy values close to that of (10,0), except for the PBE0 functional which is higher. The (9,0) CNT shows the highest energy differences of all systems, except for PBE0 functional which is very close to that of the (8,0) CNT.

Table 2 – Energetic gap of the conformational change against different functionals.

		$\Delta E_{CONFORMATIONAL}$/kcal.mol^{-1}		
(n,m)	**Number of Functionalizations**	**B3LYP**	**M06-2X**	**PBE0**
(6,0)	2	-3.11	-6.16	-6.07
(6,3)	3	6.64	-2.99	5.32
(8,0)	2	-7.26	-12.10	-15.40
(9,0)	3	-13.94	-17.36	-15.20
(10,0)	2	-6.83	-13.13	-9.77

As the (6,0) and (6,3) CNTs have very small diameters and show low energetic variations between closed and open conformations, they were only utilized as a reference in the analysis of geometrical parameters and non-covalent interactions (Section 2). As B3LYP gave similar geometries[108], it was further used in geometry optimizations where M06-2X displayed difficulties to converge and was time consuming, namely the dihedral scans (Section 3) and the drug release scans (Section 5). The M06-2X functional was evaluated as more reliable since the energy difference tendency is more coherent and because it is reported in the literature as a functional displaying higher performance when treating systems with hydrogen bonding and dispersion interactions[100, 102, 105]. Thus, it was employed in the non-covalent interactions analysis (Section 2), the acid dissociation constant calculations (Section 4) and to evaluate the scan structures given by B3LYP (Section 3 and 5).

2.2 SLDB approaches

Comparison of the larger basis sets shows higher energy differences for 3-21G/6-31G, while the 3-21G/6-31+G(d) and 3-21G/6-31++G(d) give similar values (Table 3). The 3-21G/6-31+G(d) approach was chosen to accompany M06-2X in the sections mentioned above, and the geometry optimizations with B3LYP were performed with 3-21G/6-31G, as it is less time consuming and gives a reasonable approximation to the structures obtained with M06-2X/3-21G/6-31+G(d).

Table 3 – Energetic gap of the conformational change with M06-2X functional against different basis sets.

	$\Delta E_{CONFORMATIONAL}$/kcal.mol^{-1}		
(n,m)	**3-21G/6-31G**	**3-21G/6-31+G(d)**	**3-21G/6-31++G(d)**
(8,0)	-21.58	-12.10	-12.99
(9,0)	-32.68	-17.36	-16.89
(10,0)	-21.29	-13.13	-13.62

2.3 Nanotube Length

The assessment of the length parameter demonstrates that there isn't a critical energy change for shorter or longer nanotubes, and thus the systems of length ≈9 Å were considered to provide an adequate approximation for the rest of the study (Table 4). Although the shorter nanotubes ≈7 Å gave similar results while having less atoms, the convergence to a minimum energy geometry carried the same difficulties as the other systems and similar calculation time.

Table 4 – Energetic gap of the conformational change with M06-2X functional against different nanotube lengths.

(n,m)	Number of Carbon Atoms	Lenght/Å	$\Delta E_{\text{CONFORMATIONAL}}$ /kcal.mol^{-1}
(8,0)	64	7.26	-12.60
	80	9.28	-12.10
	96	11.75	-12.30
(9,0)	72	7.12	-16.99
	90	9.26	-17.36
	108	11.37	-17.50
(10,0)	80	7.11	-13.97
	100	9.05	-13.13
	120	11.36	-13.52

For further validation, the CNT $C-C$ length and $C-C-C$ angle average values were calculated for the functionalized CNTs and compared to the values obtained for the pristine CNTs optimized with the same method, and the later were further compared to a literature reference. The parameters for the pristine CNTs do not present relevant variations relative to the reference (below 0.5%), and the parameters for the functionalized CNTs also do not significant differences (Appendix 1).

3. Non-Covalent Interactions Analysis

The non-covalent interactions present at the tips of the CNTs were characterized via geometrical parameters and topology analyses[131], such as QTAIM, NCI, ELF and electrostatic potential quantification, using the geometries optimized with M06-2X/3-21G/6-31+G(d). The analyses on the wave functions obtained were carried out with Multiwfn 3.6 Software[132, 133].

3.1 Geometrical Parameters

The bond lengths and angles for each HB are reported in Table 5 and Fig. 14, while all parameters relating to the functionalizations are reported in Appendixes 2 and 3. The $H \cdots O$ length is shorter and the covalent $O-H$ bond is longer for the (8,0) and (10,0) CNTs, which implies that these may be the stronger HB interactions of all systems, although recognizing that in some cases the distance criteria may not be enough for this distinction. Consequently, there is a red-shift of the $O-H$ stretching frequency relative to the opened conformation (Appendix 4) that is also bigger for the (8,0) and (10,0) CNTs. Additionally, the $C=O$ and $C-OH$ lengths are increased and decreased, respectively, for the (8,0) and (10,0) CNTs in relation to the other nanotubes. The (6,3) and (9,0) trifunctionalized CNTs display different lengths for each HB, whereas the (6,0), (8,0) and (10,0) bi-functionalized CNTs tend to be more symmetrical.

The $D-\widehat{H}-A$ angle is very close to the ideality (180º) for the (10,0) CNT, as the participating atoms are almost positioned in the same plane. This angle decreases for the (8,0) and (6,0) CNTs due to a misalignment of the HBs relative to (10,0). The (6,3) $D-\widehat{H}-A$ angle is lower than that of (9,0), while the later presents some variation between the different HBs. The $A'-\hat{A}-D$ and $A'-\hat{A}-H$ angles are increased for these CNTs, as the directionality of the HBs is considerably distorted, in contrast with the other CNTs where the two angles remain below 140º.

Table 5 – Bond lengths of the functionalizations and respective hydrogen bonds in the closed conformation.

			Lenght/Å			
(n,m)	**Hydrogen Bond**	**F**	**H···O**	**O−H**	**C=O**	**C−OH**
(6,0)	O80−H83···O82	F1	1.942	0.982	1.218	1.331
	O79−H81···O84	F2	1.942	0.982	1.218	1.331
(6,3)	O94−H105···O108	F1	2.123	0.978	1.210	1.339
	O98−H103···O106	F2	2.124	0.978	1.210	1.339
	O102−H107···O104	F3	2.126	0.978	1.210	1.340
(8,0)	O100−H107···O106	F1	1.757	0.993	1.223	1.323
	O104−H105···O108	F2	1.757	0.993	1.223	1.323
(9,0)	O116−H121···O123	F1	1.816	0.980	1.214	1.334
	O118−H124···O120	F2	1.871	0.986	1.213	1.325
	O112−H119···O122	F3	1.937	0.983	1.219	1.325
(10,0)	O132−H129···O128	F1	1.758	0.995	1.224	1.323
	O130−H131···O127	F2	1.758	0.995	1.224	1.323

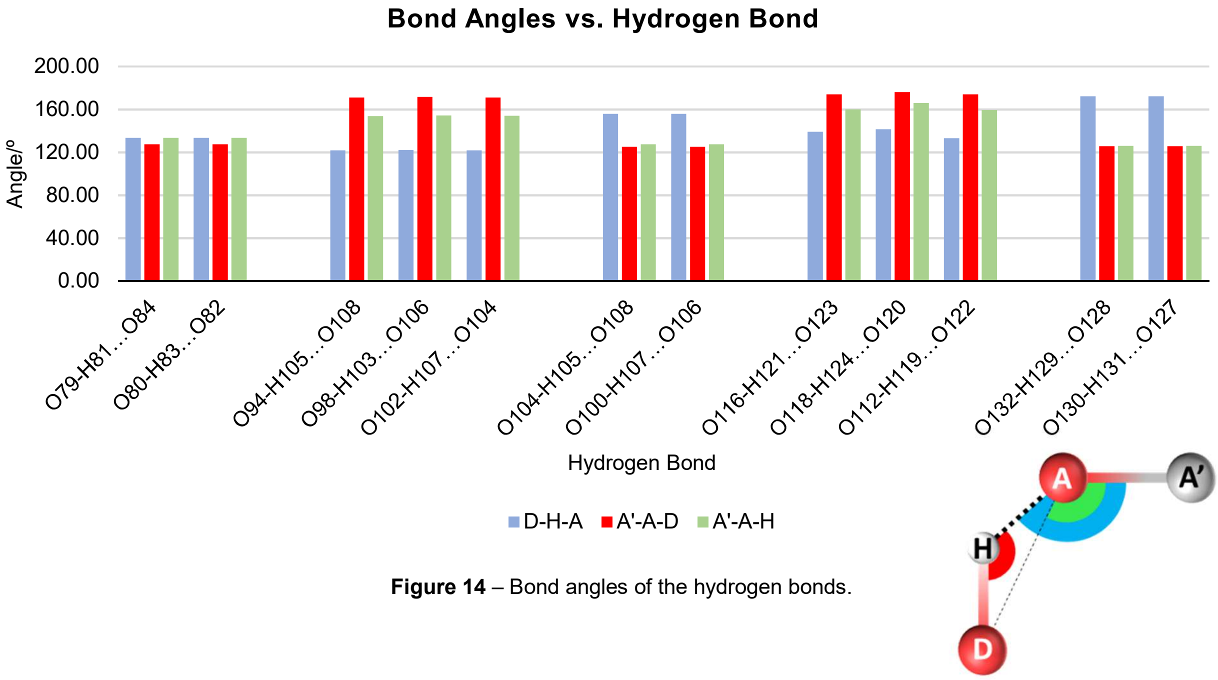

Figure 14 – Bond angles of the hydrogen bonds.

Table 6 – Diameter variation relative to pristine nanotube.

(n,m)	**∆Diameter/Å**
(6,0)	0.12
(6,3)	0.22
(8,0)	-0.08
(9,0)	0.06
(10,0)	-0.61

The energetic differences calculated here are greatly influenced by the intramolecular HBs, having a stabilizing role in the total energy. Note that there is also dependency on the variation of the CNT diameter (Table 6) and other geometrical parameters related to the functionalizations, that might introduce some energetically unfavorable strain effects. Because the (6,0) CNT has a small diameter, the two functionalizations are too close to position the hydrogen bonding groups properly, leading to axial deformation[134] of the tip that slightly increases the tip diameter of the (6,0) CNT. The (8,0) CNT allows for a better spatial arrangement of the groups, as result there is a small diameter decrease. The (10,0) CNT has the biggest diameter, as consequence it harbors a near linear HB system that induces the largest diameter decrease.

The trifunctionalized CNTs experience a diameter increase, because they carry a higher degree of tip saturation, which promotes steric clashes. The HBs also influence the $C - \widehat{CH_2} - C$ angle and related dihedrals, imposing geometries distorted from ideality that may be energetically unfavorable, but are compensated by the stabilization that the non-covalent interactions promote.

3.2 Quantum Theory of Atoms in Molecules

The QTAIM topology analysis displays BCPs at every HB expected, and these were characterized with density-dependent functions (Table 7). The BCPs with higher ED and $\nabla^2\rho(r)$ values correspond to the HBs from the (8,0) and (10,0) CNTs, followed by the asymmetrical HBs from the (9,0) CNT. The (6,3) CNT appears to exhibit the weakest HBs. The $V(r)$ and $G(r)$ values follow the same tendency expressed by the ED and $\nabla^2\rho(r)$ functions, reaching the highest values for the (8,0) and (10,0) CNTs, where $2G(r) > |V(r)| > G(r)$. Subsequently, $H(r)$ is negative while $\nabla^2\rho(r)$ is positive. For the other CNTs $|V(r)| < G(r)$, therefore $H(r)$ is positive.

This analysis suggests that the HBS belonging to the (8,0) and (10,0) systems have a great accumulation of ED at the BCP, where $\nabla^2\rho(r) > 0$ and $H(r) < 0$, being consistent with partially covalent strong HBs promoted by the larger electron delocalization contribution. The HBs present in the other systems, however, exhibit $\nabla^2\rho(r) > 0$ and $H(r) > 0$ and can be characterized as medium to weak HBs and having a larger electrostatic contribution. As mentioned, the energetic differences between conformations are influenced by factors other than the HBs, hence these can’t be used as estimates of the HB energies. Nonetheless, the energetic difference for the (10,0) CNT is slightly greater than that of the (8,0) CNT and must account for the energetically unfavorable axial deformation that accompanies the HBs, so one can conjecture that the HBs of the (10,0) CNT might be somewhat stronger. This can be corroborated by the $H(r)$ value being slightly more negative for the (10,0) CNT. Other BCPs appear in all systems between the terminal $C-H$ and O atoms (Appendix 5), some interactions showing relatively high EDs that may aid in stabilizing the HBs between functionalizations.

Table 7 – QTAIM parameters at the BCP associated with the respective hydrogen bond in the closed conformation.

(n,m)	Hydrogen Bond	BCP	ρ(r)	∇²ρ(r)	V(r)	G(r)	H(r)
(6,0)	O80-H83…O82	187	0.0251	0.0938	-0.0225	0.0230	0.0005
	O79-H81…O84	176	0.0251	0.0938	-0.0225	0.0230	0.0005
(6,3)	O94-H105…O108	250	0.0165	0.0692	-0.0145	0.0159	0.0014
	O98-H103…O106	223	0.0165	0.0690	-0.0144	0.0158	0.0014
	O102-H07…O104	180	0.0164	0.0688	-0.0144	0.0158	0.0014
(8,0)	O100-H107…O106	193	0.0378	0.1318	-0.0336	0.0333	-0.0003
	O104-H105…O108	182	0.0378	0.1317	-0.0336	0.0333	-0.0003
(9,0)	O116-H121…O123	177	0.0262	0.1088	-0.0240	0.0256	0.0016
	O118-H124…O120	246	0.0302	0.1247	-0.0280	0.0296	0.0016
	O112-H119…O122	241	0.0232	0.0969	-0.0212	0.0227	0.0015
(10,0)	O132-H129…O128	211	0.0377	0.1272	-0.0330	0.0324	-0.0006
	O130-H131…O127	262	0.0377	0.1272	-0.0330	0.0324	-0.0006

3.3 Non-covalent Interactions Index

The NCI index plot is found in Figs. 15 and 16, along with the isosurface representation of the spatial regions with low $s(r)$ and ED, and the information about the HB peaks is depicted in Table 8. The peaks in the blue region of the plots correspond to the HBs and are represented with a dark blue disc. For the symmetrical systems these peaks overlap because the same ED value is shared, and for the asymmetrical systems they appear at different $sign(\lambda 2)\rho(r)$ values. The HBs between $C-H$ and O correspond to the peaks that appear in the blue-green transition region and are represented, in the right-hand side of Figs. 15 and 16, as light blue isosurfaces where van der Waals and steric interactions also appear. Between the $O-H$ and the lateral terminal H appears a green isosurface that matches van der Waals interactions, and at the center of the CNT rings a red isosurface that are ascribed to steric effects. Other interactions present include repulsive interactions between the functionalization C atoms and the CNT terminal H atoms, coincident with RCPs, van der Waals interactions at the HBs contacts center, corresponding to RCPs, and attractive interaction between the H atoms from the $-CH_2-$ group and the CNT terminal hydrogens, matching BCPs.

Table 8 – NCI parameters at the BCP associated with the respective hydrogen bond in the closed conformation.

(n,m)	Hydrogen Bond	BCP	*s(r)*	$\text{sign}(\lambda_2)\rho(r)$
(6,0)	O80-H83…O82	187	0.345	-0.033
	O79-H81…O84	176	0.345	-0.033
(6,3)	O94-H105…O108	250	0.357	-0.023
	O98-H103…O106	223	0.359	-0.023
	O102-H07…O104	180	0.359	-0.023
(8,0)	O100-H107…O106	193	0.323	-0.047
	O104-H105…O108	182	0.323	-0.047
(9,0)	O116-H121…O123	177	0.308	-0.037
	O118-H124…O120	246	0.296	-0.041
	O112-H119…O122	241	0.313	-0.032
(10,0)	O132-H129…O128	211	0.340	-0.047
	O130-H131…O127	262	0.340	-0.047

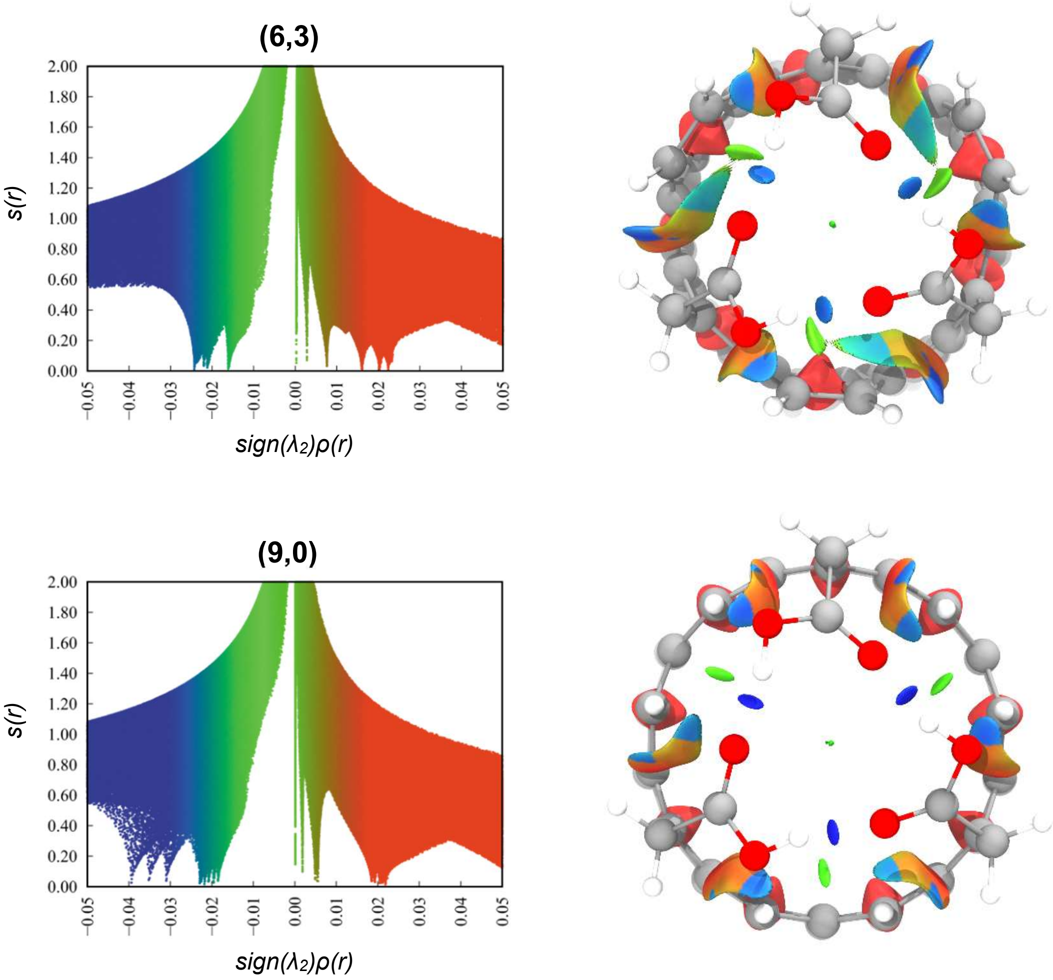

Figure 15 – NCI plots and reduced density gradient s(r) isosurface representation of the (6,3) and (9,0) systems in the closed conformation. The colors blue, green and red characterize the interaction as attractive (hydrogen bonding), weak (van der Waals) and repulsive (steric clashes).

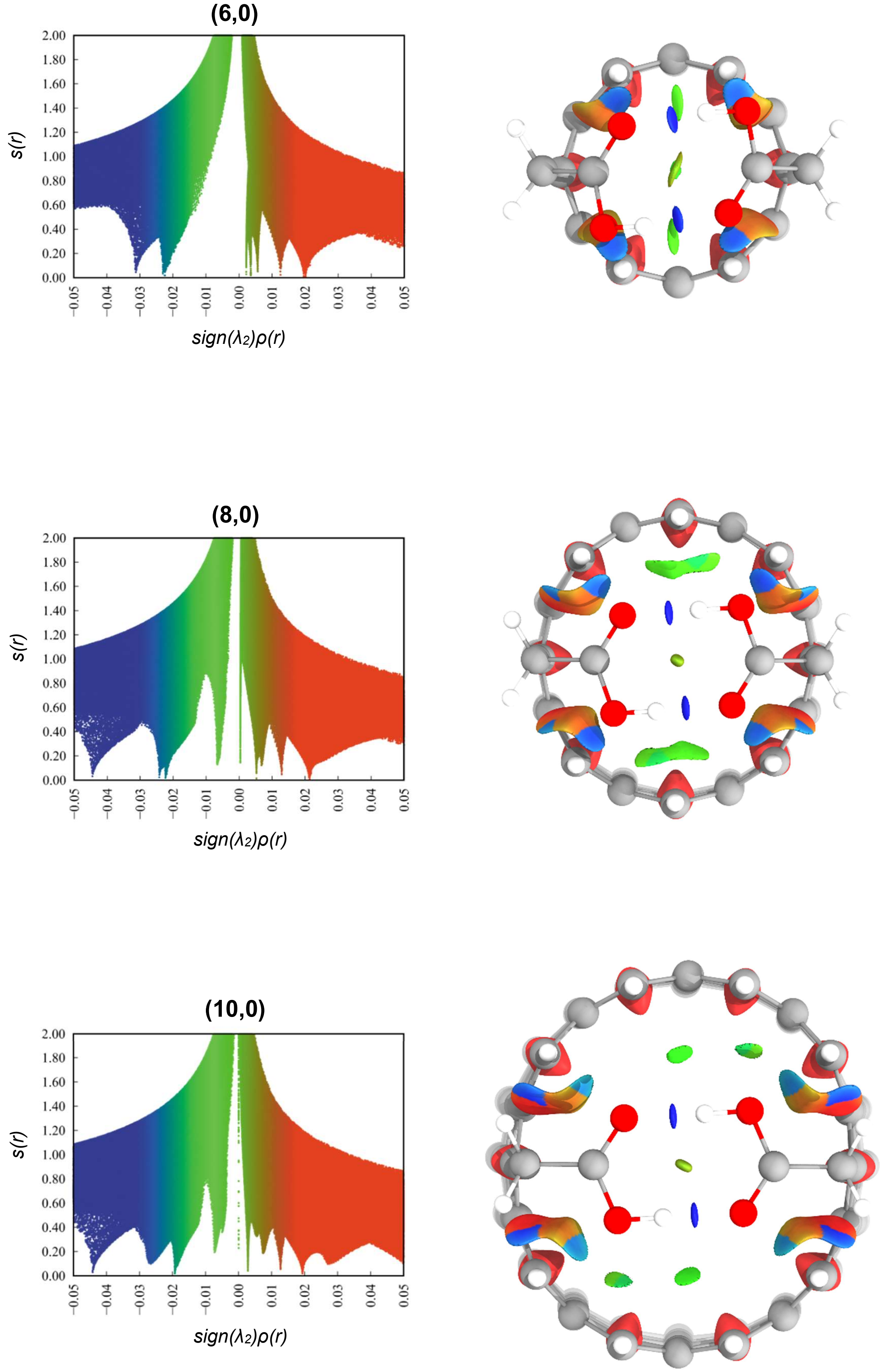

Figure 16 – NCI plots and reduced density gradient *s(r)* isosurface representation of the (6,0), (8,0) and (10,0) systems in the closed conformation. The colors blue, green and red characterize the interaction as attractive (hydrogen bonding), weak (van der Waals) and repulsive (steric clashes).

3.4 Electron Localization Function

At the BCPs, the ELF has higher values for the (8,0) and (10,0) CNTs that yield negative CVB indexes (Table 9, Figs. 17 and 18). The other CNTs have lower ELF values and positive CVB indexes, with the (6,3) CNT bearing the lowest ELF and highest CVB index. In agreement with the ED, $\nabla^2\rho(r)$ and $H(r)$ parameters, the proposed classification of the (8,0) and (10,0) HBs as stronger and partially covalent is reinforced, since the results suggest that they are dominated by electron delocalization. The other CNTs show a lower degree of delocalization, concomitant with electrostatic contribution dominance and weaker HBs. These findings also go in line with the hypothesis that the (10,0) HBs may be described, to a slight extent, by a larger delocalization energy, as both ELF and CVB index present some difference.

Table 9 – ELF value at the BCP and CVB index associated with the respective hydrogen bond in the closed conformation.

(n,m)	Hydrogen Bond	ELF(r)	CVB Index
(6,0)	O80-H83…O82	0.067	0.025
	O79-H81…O84	0.067	0.025
(6,3)	O94-H105…O108	0.036	0.053
	O98-H103…O106	0.036	0.053
	O102-H07…O104	0.036	0.053
(8,0)	O100-H107…O106	0.119	-0.024
	O104-H105…O108	0.119	-0.024
(9,0)	O116-H121…O123	0.063	0.018
	O118-H124…O120	0.075	0.029
	O112-H119…O122	0.054	0.037
(10,0)	O132-H129…O128	0.123	-0.028
	O130-H131…O127	0.123	-0.028

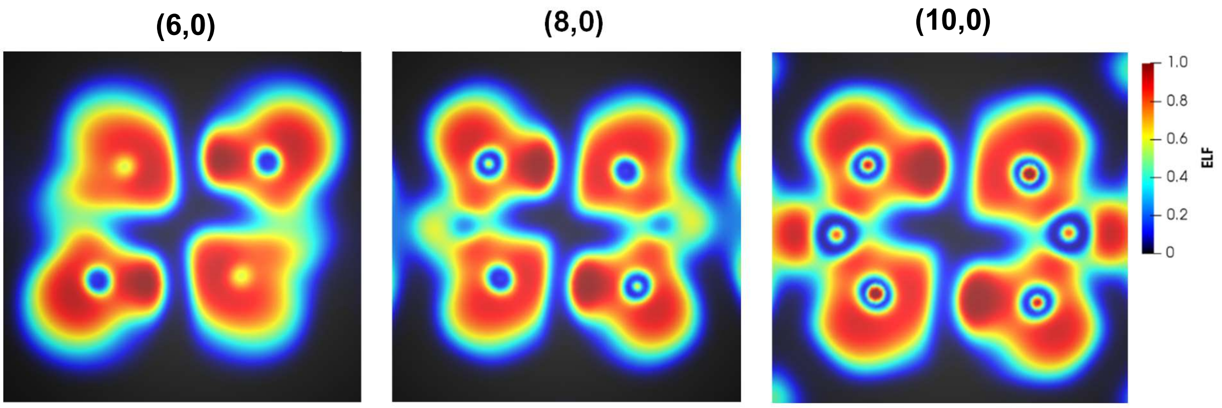

Figure 17 – ELF plane plots of the (6,0), (8,0) and (10,0) systems in the closed conformation.

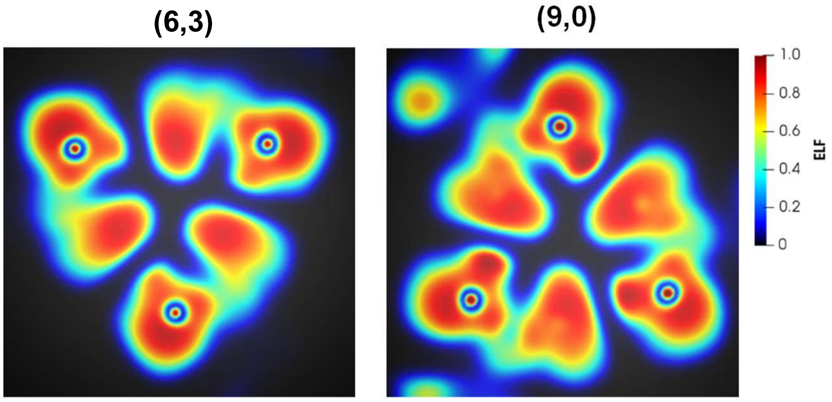

Figure 18 – ELF plane plots of the (6,3) and (9,0) systems in the closed conformation.

3.5 Quantitative Analysis of Electrostatic Potential

For the (6,0) CNT, the electrostatic potential has higher maxima at H regions than the other bifunctionalized CNT, and the (8,0) CNT presents the lowest maxima (Table 10 and Fig. 19). The electrostatic potential at the D region is similar for the (6,0) and (8,0) CNTs, but less negative for the (10,0) CNT. Acceptor regions have greater minima values of the bifunctionalized CNTs for (8,0) and the smaller for (10,0). Additional extrema appear in the (10,0) CNT, presenting two maxima of similar values associated with the H region. For the (6,3) and (9,0) CNTs, a minimum is displayed at the center of each HB network. The $-CH_2-$groups and terminal H atoms also display maxima, the latter being absent in the (6,3) and (9,0) CNTs.

The high electrostatic potential for the H region of the (6,0) weak HBs suggests that there is a low accumulation of charge, while the O atoms retain most of the ED. The increase in HB directionality in the (8,0) CNT results in a drastic reduction of the electrostatic potential in the H region and a minor decrease of the electrostatic potential at the A minima, which may lead to a weaker electrostatic interaction. This effect is more efficient in the (10,0) CNT, where the lower concentration of charge in the D and A regions generates higher minima, and the electrons are withdrawn to the H region. Consequently, the electrostatic component should be even lower in the (10,0) CNT.

The bond directionality is more perturbed for other CNTs, sharing a great increase of electrostatic potential in the H region, concomitant with a lower charge distribution in the D and A regions. Considering the charge distribution, these CNTs might have a greater electrostatic contribution and present weaker HBs. As mentioned before, the HBs from the (9,0) CNT appear to have distinct characteristics, being confirmed by the difference between electrostatic values among D, H and A regions. The (6,3), (9,0) and (10,0) CNTs present more charge depletion in the $-CH_2-$ and terminal H atom regions, which could result from higher H saturation brought by the increasing diameter and changing CNT chirality, as well from the introduced functionalizations. The two maxima associated with each H of the (10,0) CNT seem to be related with a secondary accumulation of ED from the A regions at the midpoint between the H regions, that may play a secondary role in electrostatic stabilization. For the (6,3) and (9,0) CNTs this is aggravated, originating extremum at the center of the tip where part of the charge from the A region is aggregated.

Table 10 – ESP value at the extrema indicated for each system.

	ESP/kcal.mol-1				
Extremum	**(6,0)**	**(6,3)**	**(8,0)**	**(9,0)**	**(10,0)**
1	37.41 (H)	45.14 (H)	17.73	40.85 (H)	20.69
2	37.23 (H)	45.10 (H)	17.71	37.44 (H)	20.66
3	21.20	44.90 (H)	17.11 (H)	33.19	19.43
4	21.19	24.88	17.07 (H)	32.50 (H)	19.43
5	16.43	24.83	13.36	32.30	18.25
6	16.43	24.77	13.35	28.77	18.24
7	15.61	22.22	13.34	22.39	14.66
8	15.61	22.13	13.33	22.37	14.65
9	6.02	22.05	7.35	20.03	12.05 (H)
10	6.02	17.75	7.34	17.70	11.97 (H)
11	-16.64 (D)	17.73	-16.67 (D)	17.20	11.87 (H)
12	-16.65 (D)	17.72	-16.68 (D)	16.91	11.85 (H)
13	-17.97 (A)	-6.15	-19.72 (A)	13.19	-10.61 (D)
14	-17.99 (A)	-6.20 (A)	-19.73 (A)	3.73 (A)	-10.66 (D)
15		-6.23 (A)		0.20 (A)	-15.68 (A)
16		-6.41 (A)		-3.21	-15.71 (A)
17		-14.39 (D)		-7.01 (D)	
18		-14.42 (D)		-8.65 (A)	
19		-14.47 (D)		-12.17 (D)	
20				-17.39 (D)	

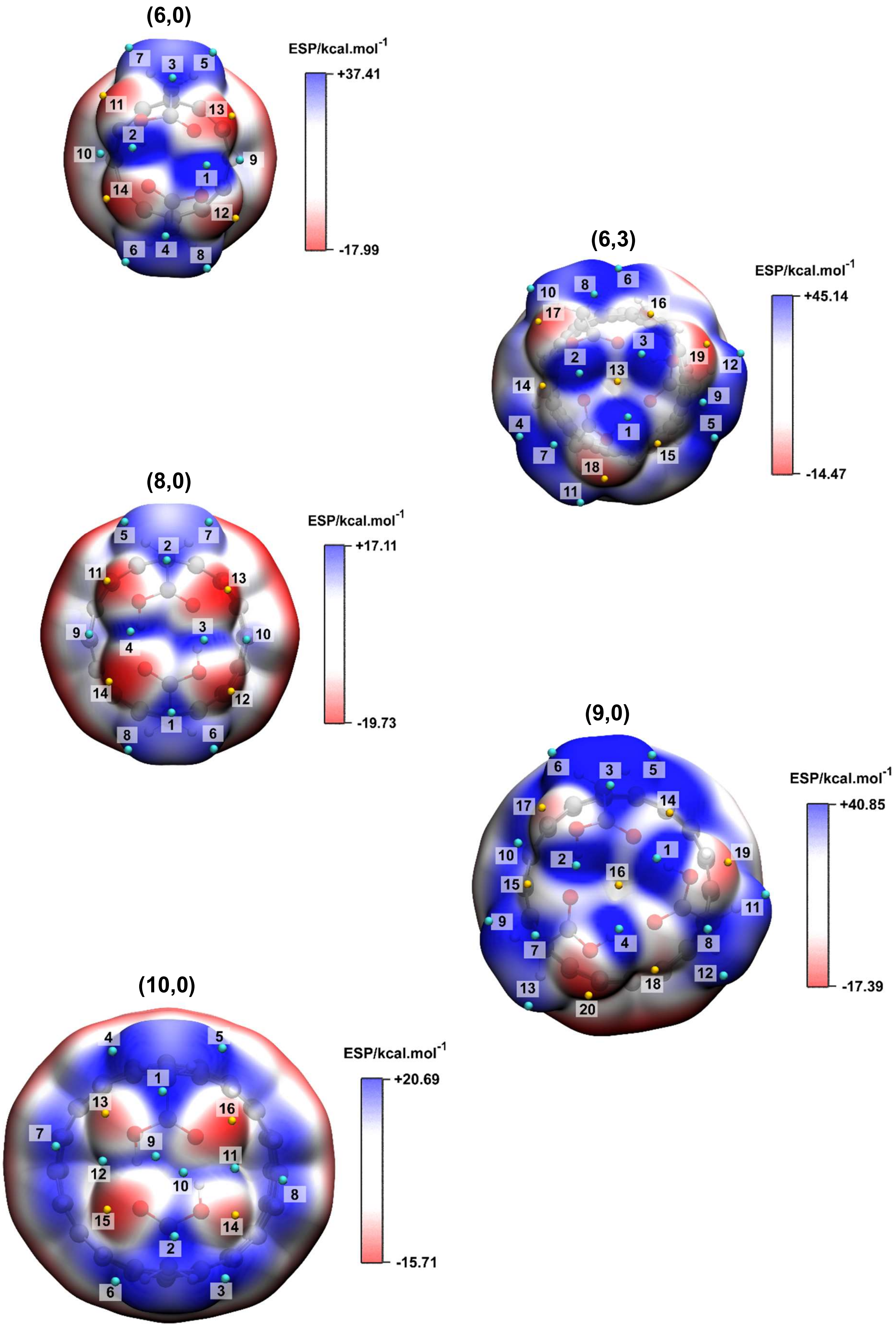

Figure 19 – Representation of the electrostatic potential map on the electron density isosurface (isovalue=0.001) and the ESP extrema for each system.

4. Conformational energetics

To get a grasp on the energetics of the conformational changes, bidimensional relaxed scans along the functionalizations dihedrals were carried out for the (8,0) and (10,0) CNTs (Appendix 6). For faster calculations, all atoms in the CNT except the terminal ring layer and the functionalizations were frozen. For the (9,0) system a unidimensional scan was performed for one dihedral, and bidimensional scans for the other dihedrals were produced using the resultant conformations of the unidimensional scan. Minimum energy paths corresponding to two different modes of rotation, successive and simultaneous, were traced along the potential energy surfaces, and single point energy calculations were carried out with the M06-2X functional to obtain the total energy of the local maxima and minima in the gas phase and with the solvation model (Table 11, Figs. 20, 21 and 22). The simultaneous mode of rotation constitutes a single step dihedral rotation to the opened conformation, while the successive mode represents a two or three step process.

The CNTs achieve local energy maxima when the functionalizations are positioned directly above the nanotube circumference and minima when the dihedral rotation is completed. The scans exhibit a single maximum for the simultaneous mode of rotation, that is energetically higher than the maxima for the successive mode of rotation in all CNTs. The 2-1 successive mode of rotation of the (9,0) CNT, where two dihedrals rotate at the same time and the third dihedral completes its rotation afterwards, has a first energetic barrier comparable to that of the simultaneous rotation, however still smaller. The successive mode of rotation gives rise to conformations that correspond to the local maxima individually characterized by lower energy change relative to the close conformation.

The different modes of rotation give similar total energetic barriers in all systems for both gas phase and solvation model, around 47 kcal.mol^{-1} in the gas phase and 44 kcal.mol^{-1} with solvation model for the (9,0) CNT, 40 kcal.mol^{-1} in the gas phase and 29 kcal.mol^{-1} with solvation model for the (10,0) CNT, finally the (8,0) CNT with 30 kcal.mol^{-1} in gas phase and 21 kcal.mol^{-1} with solvation model. The solvation model gives lower energetic barriers and decreases the energy of the opened conformation to a value near that of the closed conformation in all CNTs.

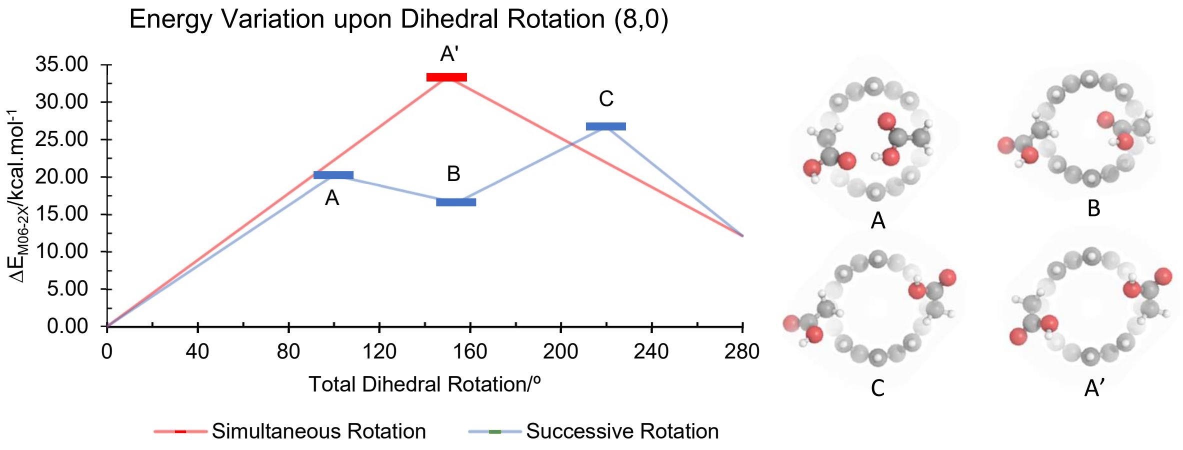

Figure 20 – Gas phase energy of the local maxima and minima relative to the closed conformation of the (8,0) system, according to different modes of dihedral rotation (successive and simultaneous) and representation of the respective conformations.

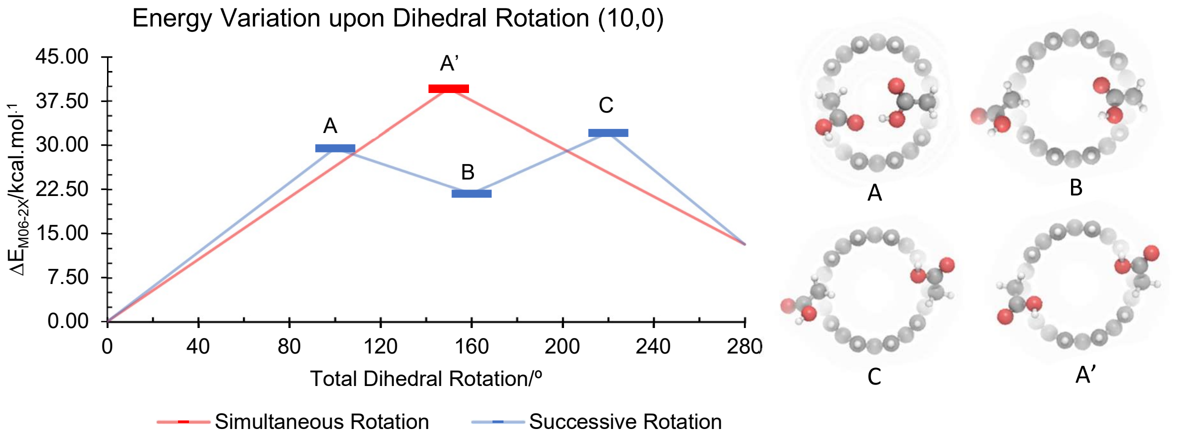

Figure 21 – Gas phase energy of the local maxima and minima relative to the closed conformation of the (10,0) system, according to different modes of dihedral rotation (successive and simultaneous) and representation of the respective conformations.

The increase in total energy at each maximum can be attributed to short range repulsive interactions arising between C and H atoms of the functionalizations and terminal H atoms of the CNTs, culminating in a notorious increase in total energy when more than one functionalizations are in this conformation. The high energetic barrier of the simultaneous dihedral rotation in the (9,0) CNT is a direct consequence of this, as the three functionalizations are experiencing repulsive forces. At the maxima, the functionalizations might be still interacting with one another, causing a decrease in energy.

The solvation model can lower the energetic barriers of the CNTs because it accounts for polarization, dispersion and HB interactions with the solvent that compensate the rupture of the non-covalent interactions and lack of intermolecular interactions in the gas phase. This also ensues the stabilization of the opened conformation that balances the total energies of the gas phase to produce low energy differences between opened and closed conformations.

It is possible that the successive mode of rotation is kinetically more favorable, as the molecules go through lower energy barriers and can get held in the minima until they receive the energy necessary to continue dihedral rotation. The achieving of the higher energy states present in the simultaneous dihedral rotations may be limited by the available energy, and thus less probable to occur than the other processes.

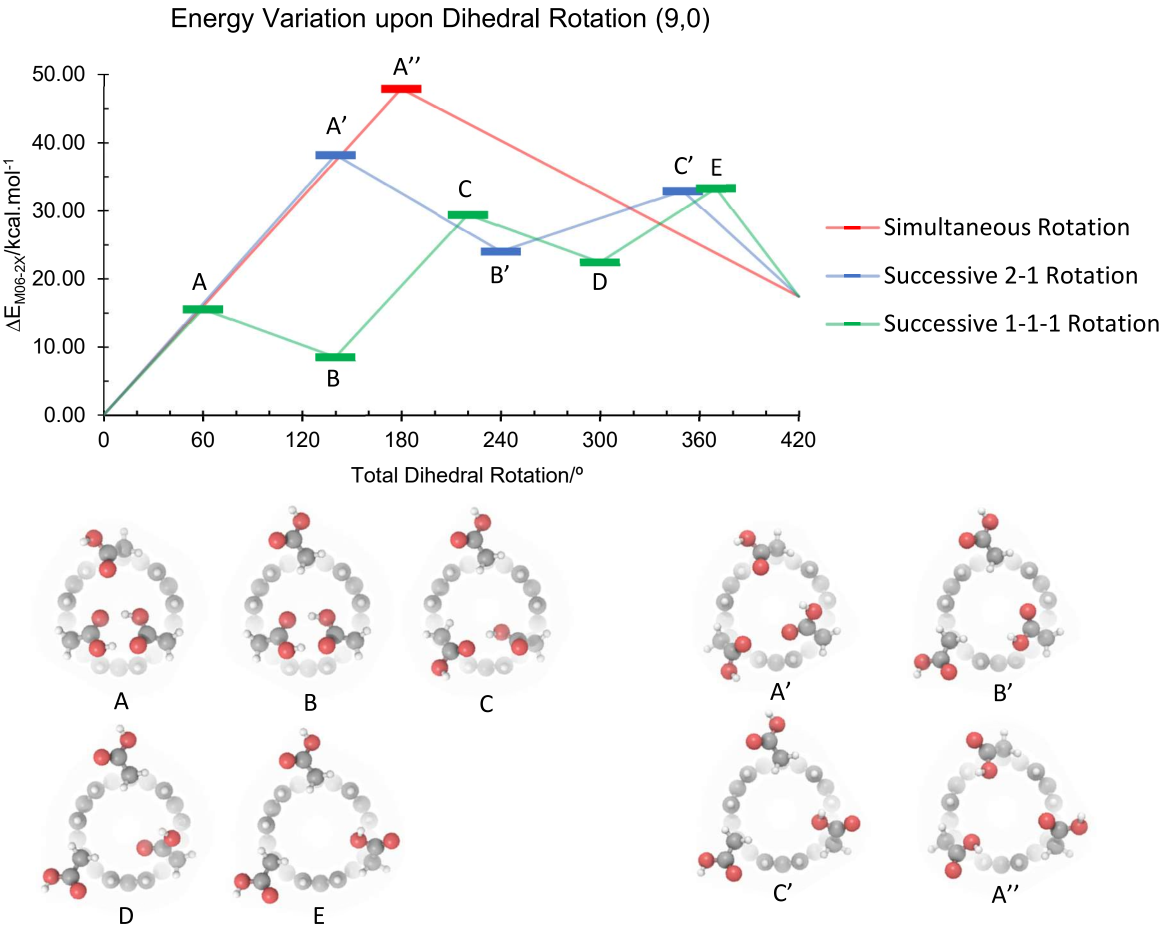

Figure 22 – Gas phase energy of the local maxima and minima relative to the closed conformation of the (9,0) system, according to different modes of dihedral rotation (successive and simultaneous) and representation of the respective conformations.

Table 11 – Energy variation evaluated by M06-2X and M06-2X with SMD solvation model upon conformational change of the systems (8,0), (9,0) and (10,0).

(n,m)	Conformational Change	$\Delta E_{M06\text{-}2X}$/kcal.mol^{-1}	$\Delta E_{M06\text{-}2X\ Solvation}$/kcal.mol^{-1}
(8,0)	Closed→A	20.20	14.47
	A→B	-3.66	-9.40
	B→C	10.13	8.30
	C→Opened	-14.58	-13.93
	Closed→A'	33.30	20.73
	A'→Opened	-21.20	-21.29
	Closed→Opened	12.10	-0.56
(10,0)	Closed→A	29.46	25.22
	A→B	-7.70	-11.93
	B→C	10.37	7.42
	C→Opened	-18.99	-18.94
	Closed→A'	39.59	29.27
	A'→Opened	-26.45	-27.50
	Closed→Opened	13.13	1.78
(9,0)	Closed→A	15.59	20.59
	A→B	-7.07	-8.72
	B→C	20.93	14.61
	C→D	-7.05	-7.86
	D→E	10.91	9.34
	E→Opened	-15.95	-25.29
	Closed→A'	38.20	37.62
	A'→B'	-14.17	-16.57
	B'→C'	8.93	6.25
	C'→Opened	-15.60	-24.63
	Closed→A''	47.91	45.89
	A''→Opened	-30.55	-43.21
	Closed→Opened	17.36	2.67

5. Acid Dissociation Constant (pK_a)

To calculate the acid dissociation constant associated with each deprotonation, geometry optimizations were executed for each deprotonated state, and the pK_a was computed from the direct cycle as described in Chapter II. The initial deprotonation reactions stabilize the closed conformation, then the deprotonation of all functionalizations prompts a conformational change from closed to opened (Figs. 23 and 24). The pK_{a1} value is very low for all CNTs, while the pK_{a2} is 3-5 units higher, reaching 7.58 for the (10,0) CNT and values around 6 for the (8,0) and (9,0) CNTs. The pK_{a3} of the (9,0) CNT is comparable to the pK_{a2} of the (10,0) CNT (Table 12).

The first deprotonation leaves the remaining carboxylic acids establishing HBs with the charged carboxylate groups. These interactions are expected to be very strong and are generally classified as charge-assisted HBs. The increase in energy brought by the deprotonation reactions is stabilized when charge-assisted interactions are present, leading to low pK_{a1} values. The next deprotonation drives a conformational change for the (8,0) and (10,0) nanotubes, due to repulsive interactions between the charged groups, and gives rise to a high energy state that increases the pK_{a2} value. The last deprotonated state of (10,0) CNTs seems to be energetically less stable relative to the (8,0) CNT, as it gives a pK_{a2} value more than 1 unit higher. The lowest pk_{a2} value belongs to the (9,0) CNT, since the second deprotonated state is still stabilized by a charge-assisted HB. The third deprotonation of the (9,0) CNT leads to a conformational change, and a concomitant total energy increase caused by three negatively charged groups, that gives a pK_{a3} value slightly lower than the highest.

Table 12 – Acid dissociation constant (pK_a) values for each successive deprotonation from the closed conformation.

	(n,m)		
pK_{an}	**(8,0)**	**(9,0)**	**(10,0)**
pK_{a1}	2.68	3.03	2.70
pK_{a2}	6.38	5.89	7.58
pK_{a3}	-	7.10	-

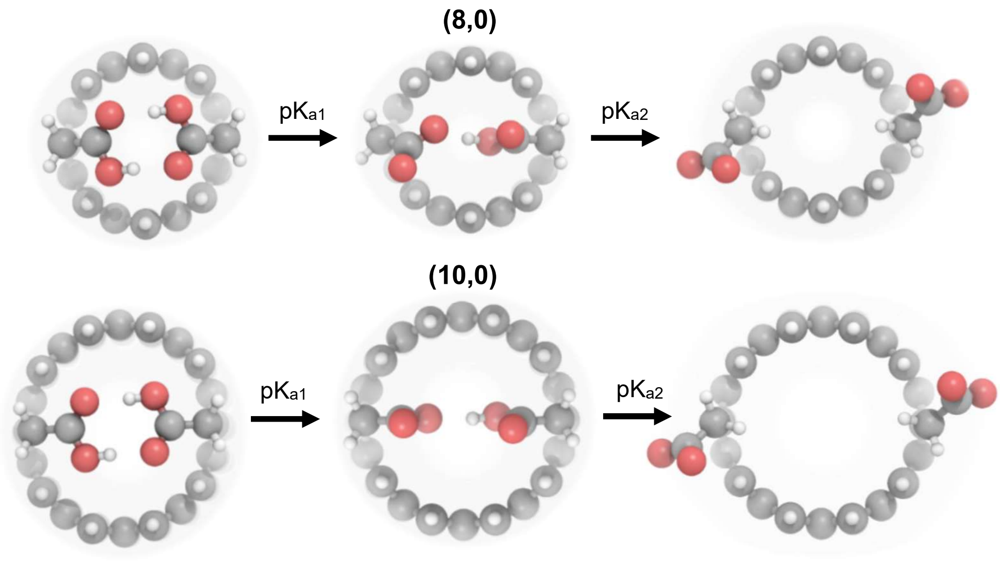

Figure 23 – Representation of the deprotonation optimized geometries obtained with the solvation model and M06-2X functional for the (8,0) and (10,0) systems.

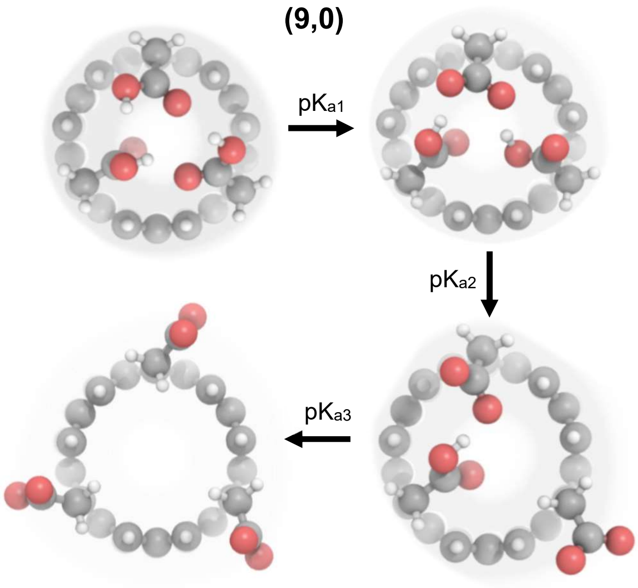

Figure 24 – Representation of the deprotonation optimized geometries obtained with the solvation model and M06-2X functional for the (9,0) system.

6. Drug Release Scan

A relaxed scan was produced for the release of fluorouracil, a heterocyclic aromatic drug molecule, in both conformations of the (10,0) CNT, initially being encapsulated and then following a linear trajectory along 14 Å to the outside, in successive steps of 1 Å (Figs. 25, 26 and 27). The energy changes follow similar trends for both conformations, except for the geometries of the closed conformation at 5 Å and 11 Å, which appear to be potential energy barriers that coincide with the rupture of the intramolecular HBs and passage of both halves of the drug molecule. In the opened conformation, the functionalizations do not interact with the drug molecule, thus there are no energetic barriers holding back diffusion. The solvent model brings an overall stabilization to the CNTs and the energetic barriers are lowered.

In the first steps of scans, the drug molecule is inside the CNT where it experiences dispersion interactions with the nanotube walls, such as π-effects. For the closed conformation, the drug reaches a distance where it starts to exert repulsive interactions with the functionalizations, promoting HB rupture and increasing the distance between functionalizations. Along the passage of the drug in the terminal region of the CNT, the OH groups in the functionalizations can show attractive interactions with the electron dense moieties of the drug molecule that might stabilize the energy, as there is presence of electronegative atoms (N, O and F) and π-bonds.

The potential energy barriers arising at 5 Å and 11 Å can be attributed to the movement of two different portions of the drug molecule along the terminal region, the first having a ketone group and a F atom, and the second having another ketone group and N atoms that are inserted in the cyclic ring. The first region has chemical groups capable of having stronger interactions with the functionalizations, due to high electronegativity, and the F atom has a smaller size that could minimize short-range repulsion, leading to a lower energetic barrier. The second region also has a ketone group, but the less electronegative and bigger sized N atoms might provide weaker attractive interactions and an increase in repulsion, that elevates the total energy of the CNT. At 12 Å, the drug molecule is no longer between the functionalization groups, and these can regenerate the intramolecular HBs, having a stabilizing effect on the energy of the CNT.

In the opened conformation, the drug and CNT only interact via dispersion forces, resulting in a smoother energy curve. With the solvent model the energetic tendency is similar, but there is an overall stabilization and lowering of the energetic barriers that can be attributed to stabilizing contributions between the solvent and the drug molecule or the functionalizations. The large energy difference observed in the drug release process may be due to the use of a smaller basis set in the nanotube C atoms, nevertheless, the interactions between drug and functionalizations are treated with the 6-31+g(d) basis set. Another factor that can have an effect in the total energy is the basis set superposition error, which is not accounted for.

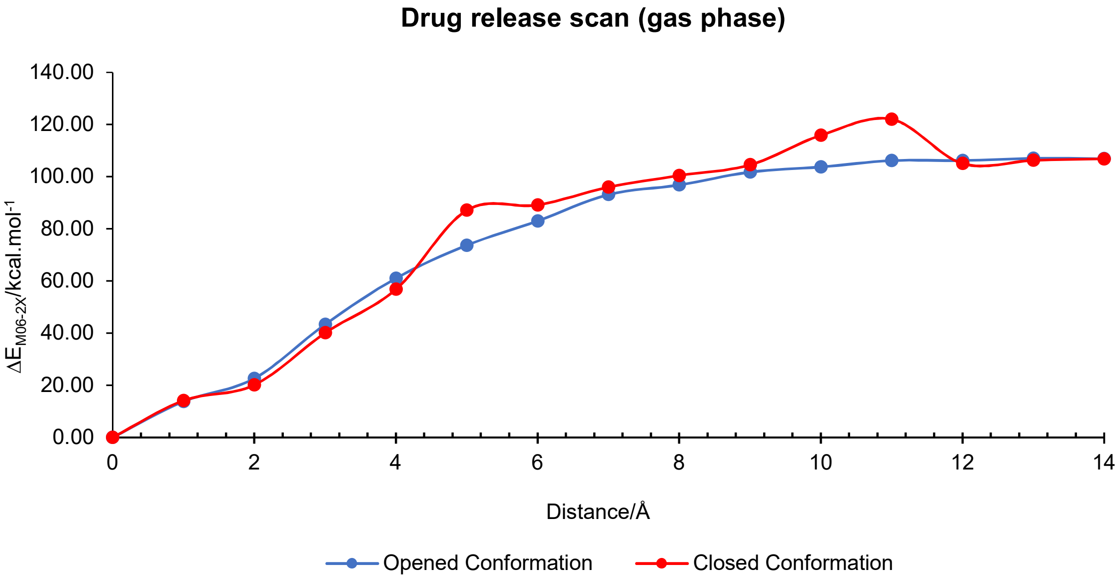

Figure 25 – Energy variation from the drug release scan in the gas phase for both conformations.

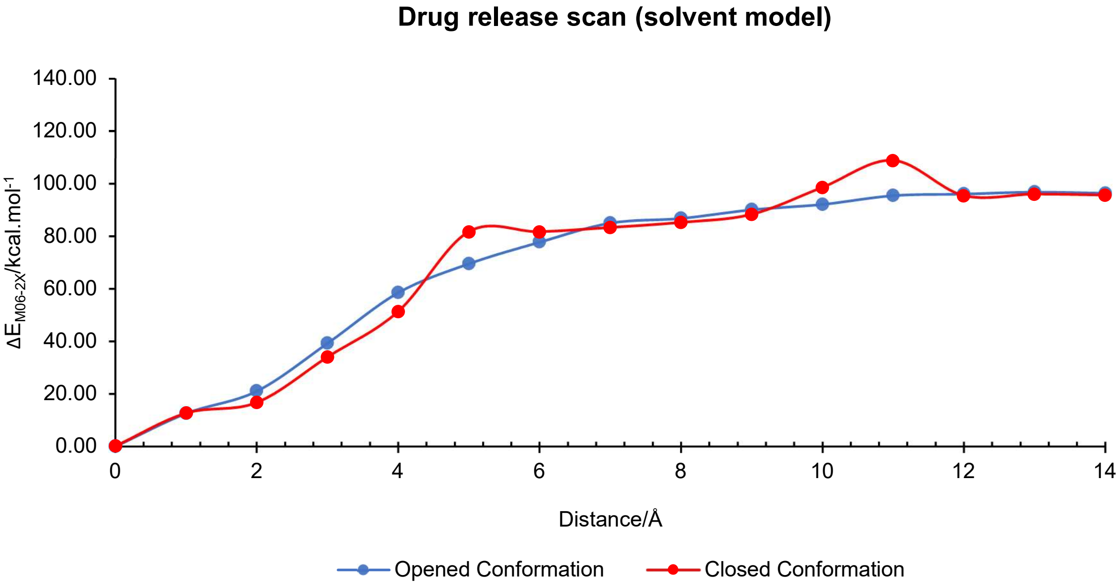

Figure 26 – Energy variation from the drug release scan with solvent model for both conformations.

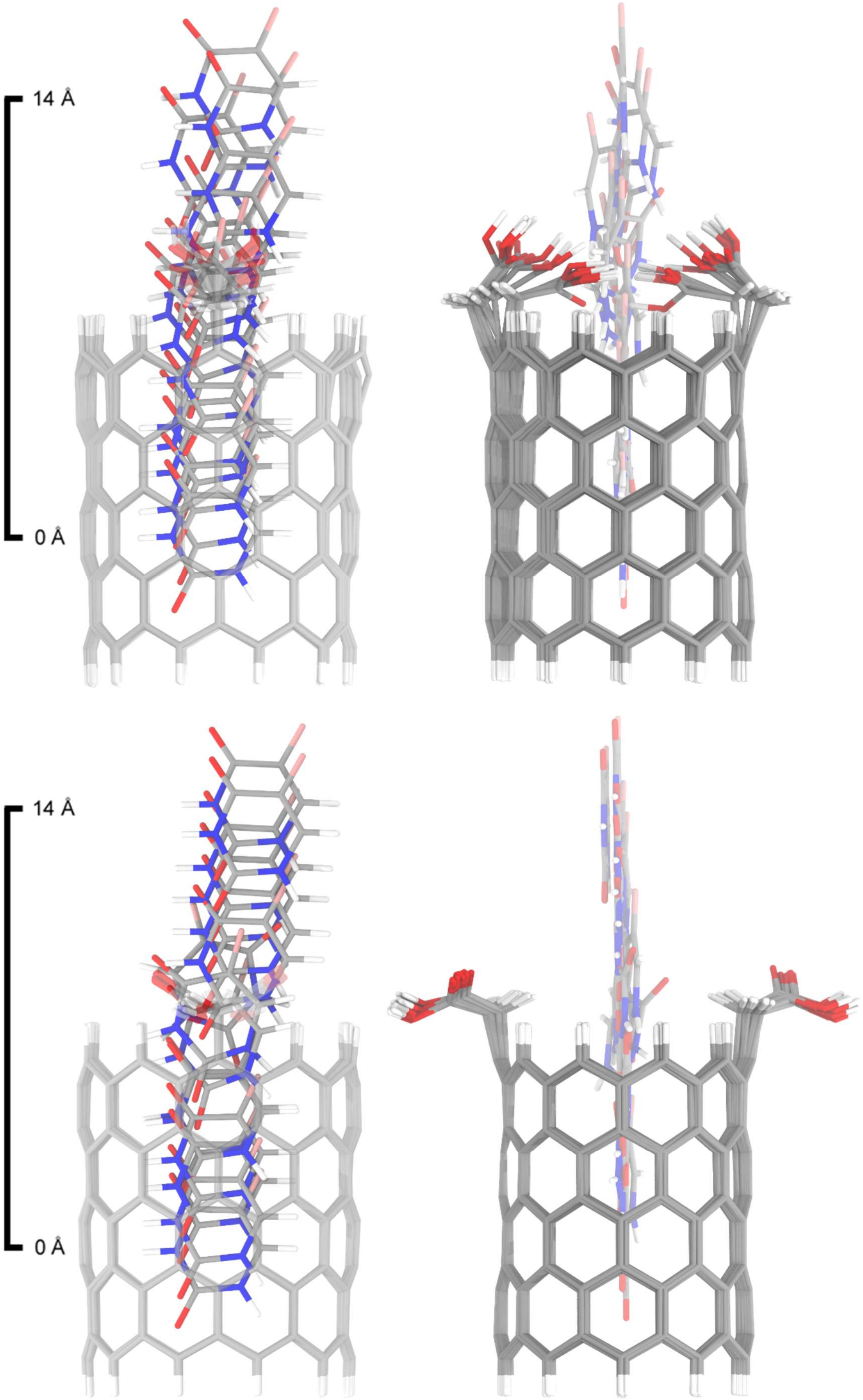

Figure 27 – Superposition of the optimized geometries from the drug release scans.

7. Concluding Remarks

Drug delivery system formulations present the advantages of reducing unwanted side effects and longer circulation times of drug molecules, promoting higher efficiency and safety in treatments of innumerous pathological conditions. The design of such systems obeys some required characteristics such as biocompatibility, protection from degradation enzymes, molecular targeting and controlled release[135, 136]. In this context, several structures that promote a solvent excluded area where drug molecules are encapsulated have been reported[137-140], many including moieties that form molecular recognition sites complementary to some specific cellular site or stimuli sensitive conformational changes that allow for the cargo release. The functionalized CNTs reported here directly address the controlled release topic, as the systems display a pH-sensitive conformational alteration that enable the diffusion of the cargo to the solvent. Furthermore, the assembly of supramolecular nanostructures that uses several molecules as building blocks may increase the appreciated qualities in the drug delivery process[141, 142].

The intramolecular HBs between functionalizations have an essential role in these CNTs, as they stabilize the system in the closed conformation. The chirality, diameter and number of functionalization parameters define systems having HBs with different characteristics, despite having the same D, H and A atoms. The strongest HBs were found for the (8,0) and (10,0) CNTs and share some similarity in terms of geometrical parameters and energy components. Nonetheless, a small difference can be spotted between the energy component, that arises from an increase in hydrogen bond linearity for the (10,0) CNT. As consequence, the QTAIM and ELF analyses suggest a higher electron delocalization contribution for the (10,0) CNT that is generally correlated with stronger HBs. The ESP quantitative analysis on the molecular surface indicates that the electrostatic contribution is higher for the (8,0) CNT, which can be interpreted as decrease in HB strength relative to the (10,0) CNT.

Additionally, the results point to interactions between HBs arising from secondary polarization phenomena, and the presence of weaker HBs to the oxygen atoms that may aid in stabilizing the systems[143, 144]. In the (10,0) CNT, charges are more evenly distributed along the HB path, reflecting the higher degree of delocalization, and there is higher ED accumulation at the middle of the carboxylic groups that may have a role in stabilizing the electrostatic interactions of the system. In the (6,0) and (8,0) CNTs, the loss of linearity attenuates this effect and contributes to an increase in electrostatic energy contribution. As result of the symmetric character of these systems it is possible to consider the classification of low-barrier HBs, especially for the (8,0) and (10,0) CNTs, since the pK_a of the D and A atoms should be similar, thus giving the same stability for the proton when covalently bound to the D or A atom and a low energetic barrier for proton trade between functionalizations that increases the strength of interaction. In contrast, the trifunctionalized CNTs present HB networks that are composed by weaker interactions, mostly characterized by a lack of linearity and large electrostatic contribution relative to the delocalization energy.

Although there are significant energy differences between the opened and closed conformations in the gas phase, the solvation model allows for an energetic stabilization of the functionalizations in the opened conformation that decreases the energy differences to a few kilocalories. As consequence of the similar stability, both conformations might be equally probable in solution[145], in contrast with the higher stability expected in the gas phase. Nevertheless, the energetic barriers associated with conformational change might be high enough to keep the functionalizations in either conformation, and could be increased by the introduction of bulky groups in CH_2. Additionally, the inclusion of CNTs in a hydrophobic medium might favor the stability of the closed conformation.

The pK_a values calculated revealed that the deprotonations are favored at distant pH values, nonetheless the conformational change only happens upon the last deprotonation. Considering the applicability in drug-delivery, this might be advantageous since cancer cells have been shown to create a pH gradient characterized by an acidic extracellular medium and an alkaline cytoplasm, that could act as trigger to drug-release[146]. Indeed, the second pK_{a2} of the (10,0) CNT fits the intracellular pH range of cancer cells ($pH_i \approx 7.3$ - 7.6), while the pK_{a1} is severely low relative to the pH of the extracellular medium ($pH_e \approx 6.8 – 7.0$)[146]. In this sense, the first deprotonated state should be more favorable in the extracellular medium and the second more favorable in the cytoplasm, resulting in conformational change upon entrance. However, the pH of biological fluids tends to be neutral, close to the pK_{a2} of the functionalized CNTs, which could induce an unwanted conformational exchange. This can be surpassed by the inclusion of the CNTs in a vehicle structure that excludes the solvent.

The relaxed scan performed for the release of fluorouracil, a small drug molecule analogous to the nucleotide uracil that is used in chemotherapy for breast, rectal, colon and stomach cancer, among others, demonstrated that the release of encapsulated cargo is unfavorable for the closed conformation of the CNT. The encapsulated molecules must provoke the rupture of the HBs between conformations and display short-range repulsive interactions with the functionalizations, making the process energetically costly relative to the release from the opened conformation. An important factor is the presence of electronegative groups, because they exhibit interactions with the functionalizations that counterbalance the repulsive forces, and the van der Waals radius also plays a role, as smaller atoms may promote lower repulsive forces and decrease the geometry distortion of the functionalizations. Hence, the increase in polar groups or electronegative atoms in encapsulated drug molecules may be translated to lower energetic barriers and a greater probability for the drug release phenomena in closed conformation. The use of nonpolar molecules can lead to an increase in the energetic barrier, as they are not capable of establishing attractive interactions to compensate the HB rupture.

The pK_a characteristics of the CNTs imply that they should be incorporated in a solvent excluded vehicle for blood circulation, such as a large surfactant vesicle with an internal acidic pH, to keep the drug molecules incapsulated. Covalent functionalization on the sidewall with molecular recognition sites could direct the CNTs to the membrane of cancer cells where they are readily incorporated[52]. Such drug-delivery system could have the advantages of increasing the bioavailability, specificity and efficiency of chemotherapeutics such as fluorouracil. The pH-sensitive nanochannels can have further applications other than biological, such as the use in water purification or separation of gases[125, 147-150], and the removal of reagents/products in catalysis[151].

List of References

1. Pauling, L., *The nature of the chemical bond. Application of results obtained from the quantum mechanics and from a theory of paramagnetic susceptibility to the structure of molecules.* Journal of the American Chemical Society, 1931. **53**(4): p. 1367-1400.
2. Cohen, I. and J. Del Bene, *Hybrid orbitals in molecular orbital theory.* Journal of Chemical Education, 1969. **46**(8): p. 487.
3. Mathur, R.B., B.P. Singh, and S. Pande, *Carbon Nanomaterials: Synthesis, Structure, Properties and Applications*. 1 ed. 2017: Taylor & Francis. 284.
4. Zhang, Q., *Carbon Nanotubes and Their Applications*. 1 ed. Pan Stanford Series on Carbon-Based Nanomaterials, ed. A. Wee and A.H.C. Neto. Vol. 1. 2012 Pan Stanford 400.
5. Bundy, F.P., *The P, T phase and reaction diagram for elemental carbon, 1979.* Journal of Geophysical Research: Solid Earth, 1980. **85**(B12): p. 6930-6936.
6. Patrick, G.S. and M.S.R. Rao, *Carbon-based nanoscience and nanotechnology: where are we, where are we heading?* Journal of Physics D: Applied Physics, 2010. **43**(37): p. 370301.
7. Yellampalli, S., *Carbon Nanotubes: Polymer Nanocomposites*. 2011: InTech.
8. Rafii-Tabar, H., *Computational Physics of Carbon Nanotubes*. 2007, Cambridge: Cambridge University Press.
9. Fuchs, J.-N. and M.O. Goerbig, *Introduction to the physical properties of graphene.* Lecture notes, 2008.
10. Novoselov, K.S., et al., *Electric Field Effect in Atomically Thin Carbon Films.* Science, 2004. **306**(5696): p. 666.
11. Warner, J.H., *Introduction*, in *Graphene*, J.H. Warner, et al., Editors. 2013, Elsevier. p. 1-4.
12. Mohan, V.B., et al., *Graphene-based materials and their composites: A review on production, applications and product limitations.* Composites Part B: Engineering, 2018. **142**: p. 200-220.
13. Randviir, E.P., D.A.C. Brownson, and C.E. Banks, *A decade of graphene research: production, applications and outlook.* Materials Today, 2014. **17**(9): p. 426-432.
14. Zurutuza, A. and C. Marinelli, *Challenges and opportunities in graphene commercialization.* Nature Nanotechnology, 2014. **9**: p. 730.
15. Wallace, P.R., *The Band Theory of Graphite.* Physical Review, 1947. **71**(9): p. 622-634.
16. Warner, J.H., et al., *Properties of Graphene*, in *Graphene*, J.H. Warner, et al., Editors. 2013, Elsevier. p. 61-127.
17. Schäffel, F., *The Atomic Structure of Graphene and Its Few-layer Counterparts*, in *Graphene*, J.H. Warner, et al., Editors. 2013, Elsevier. p. 5-59.
18. Maffucci, A. and G. Miano, *Electrical Properties of Graphene for Interconnect Applications.* Applied Sciences, 2014. **4**(2).
19. Castro Neto, A.H., et al., *The electronic properties of graphene.* Reviews of Modern Physics, 2009. **81**(1): p. 109-162.
20. Fathi, D., *A Review of Electronic Band Structure of Graphene and Carbon Nanotubes Using Tight Binding.* Journal of Nanotechnology, 2011. **2011**.
21. Geim, A.K. and K.S. Novoselov, *The rise of graphene.* Nature Materials, 2007. **6**: p. 183.
22. Geim, A.K. and P. Kim, *Carbon wonderland.* Sci Am, 2008. **298**(4): p. 90-7.
23. Choi, W., et al., *Synthesis of Graphene and Its Applications: A Review.* Critical Reviews in Solid State and Materials Sciences, 2010. **35**(1): p. 52-71.
24. Ando, T., *The electronic properties of graphene and carbon nanotubes.* Npg Asia Materials, 2009. **1**: p. 17.
25. Peres, N.M.R., *The electronic properties of graphene and its bilayer.* Vacuum, 2009. **83**(10): p. 1248-1252.

26. Allen, M.J., V.C. Tung, and R.B. Kaner, *Honeycomb Carbon: A Review of Graphene.* Chemical Reviews, 2010. **110**(1): p. 132-145.
27. Radushkevich, L.V. and V.M. Lukyanovich, *Structure of the carbon produced in the thermal decomposition of carbon monoxide on an iron catalyst*. Vol. 26. 1952. 88-95.
28. Oberlin, A., M. Endo, and T. Koyama, *Filamentous growth of carbon through benzene decomposition.* Journal of Crystal Growth, 1976. **32**(3): p. 335-349.
29. Iijima, S., *Helical microtubules of graphitic carbon.* Nature, 1991. **354**: p. 56.
30. Jorio, A., G. Dresselhaus, and M.S. Dresselhaus, *Carbon nanotubes : advanced topics in the synthesis, structure, properties, and applications.* 2008.
31. Dresselhaus, M.S., et al., *Carbon Nanotubes: Synthesis, Structure, Properties, and Applications*. 2001: Springer Berlin Heidelberg.
32. Serpell, C.J., K. Kostarelos, and B.G. Davis, *Can Carbon Nanotubes Deliver on Their Promise in Biology? Harnessing Unique Properties for Unparalleled Applications.* ACS Central Science, 2016. **2**(4): p. 190-200.
33. Balasubramanian, K. and M. Burghard, *Chemically Functionalized Carbon Nanotubes.* Small, 2005. **1**(2): p. 180-192.
34. Niyogi, S., et al., *Chemistry of Single-Walled Carbon Nanotubes.* Accounts of Chemical Research, 2002. **35**(12): p. 1105-1113.
35. Odom, T.W., et al., *Atomic structure and electronic properties of single-walled carbon nanotubes.* Nature, 1998. **391**: p. 62.
36. Odom, T.W., J.-L. Huang, and C.M. Lieber, *Single-Walled Carbon Nanotubes: From Fundamental Studies to New Device Concepts.* Annals of the New York Academy of Sciences, 2002. **960**(1): p. 203-215.
37. Saeed, K. and I. Khan, *Carbon nanotubes–properties and applications: a review*. Vol. 14. 2013. 131-144.
38. Amori, A.R., Z. Hou, and T.D. Krauss, *Excitons in Single-Walled Carbon Nanotubes and Their Dynamics.* Annual Review of Physical Chemistry, 2018. **69**(1): p. 81-99.
39. Thostenson, E.T., Z. Ren, and T.-W. Chou, *Advances in the science and technology of carbon nanotubes and their composites: a review.* Composites Science and Technology, 2001. **61**(13): p. 1899-1912.
40. Ding, F., *Theoretical study of the stability of defects in single-walled carbon nanotubes as a function of their distance from the nanotube end.* Physical Review B, 2005. **72**(24): p. 245409.
41. Artyukhov, V.I., E.S. Penev, and B.I. Yakobson, *Why nanotubes grow chiral.* Nature Communications, 2014. **5**(1): p. 4892.
42. Fernandes, R.M.F., *Dispersing Carbon Nanotubes: Towards Molecular Understanding*, in *TRITA-CHE-Report*. 2015, KTH Royal Institute of Technology: Stockholm. p. xii, 77.
43. Chen, Z., W. Thiel, and A. Hirsch, *Reactivity of the Convex and Concave Surfaces of Single-Walled Carbon Nanotubes (SWCNTs) towards Addition Reactions: Dependence on the Carbon-Atom Pyramidalization.* ChemPhysChem, 2003. **4**(1): p. 93-97.
44. Meng, L., C. Fu, and Q. Lu, *Advanced technology for functionalization of carbon nanotubes.* Progress in Natural Science, 2009. **19**(7): p. 801-810.
45. Díaz-Cervantes, E., et al., *Solubility of functionalized single-wall carbon nanotubes in water: a theoretical study.* Theoretical Chemistry Accounts, 2017. **136**(11): p. 127.
46. Sharma, A., B.J. Gifford, and S. Kilina, *Tip Functionalization of Finite Single-Walled Carbon Nanotubes and Its Impact on the Ground and Excited State Electronic Structure.* The Journal of Physical Chemistry C, 2017. **121**(15): p. 8601-8612.
47. Mostaanzadeh, H., A. Abbasi, and E. Honarmand, *DFT Theoretical Calculation of the Site Selectivity of Dihydroxylated (5, 0) Zigzag Carbon Nanotube.* Russian Journal of Physical Chemistry A, 2017. **91**(13): p. 2636-2642.
48. Burghard, M., *Asymmetric End-Functionalization of Carbon Nanotubes.* Small, 2005. **1**(12): p. 1148-1150.

49. Kharissova, O.V. and B.I. Kharisov, *Solubilization and Dispersion of Carbon Nanotubes*. 1 ed. 2017: Springer International Publishing. XII, 250.
50. Mananghaya, M., *Modeling of single-walled carbon nanotubes functionalized with carboxylic and amide groups towards its solubilization in water.* Journal of Molecular Liquids, 2015. **212**: p. 592-596.
51. Bianco, A., K. Kostarelos, and M. Prato, *Applications of carbon nanotubes in drug delivery.* Current Opinion in Chemical Biology, 2005. **9**(6): p. 674-679.
52. Lin, Y., et al., *Advances toward bioapplications of carbon nanotubes.* Journal of Materials Chemistry, 2004. **14**(4): p. 527-541.
53. Kar, T., et al., *Do phenolic and carboxylic groups coexist at the tips of oxidized single-wall carbon nanotubes (o-SWNTs)?* Carbon, 2014. **73**: p. 194-205.
54. Wang, C., et al., *Chemical Functionalization of Carbon Nanotubes by Carboxyl Groups on Stone-Wales Defects: A Density Functional Theory Study.* The Journal of Physical Chemistry B, 2006. **110**(21): p. 10266-10271.
55. Khare, K.S., F. Khabaz, and R. Khare, *Effect of Carbon Nanotube Functionalization on Mechanical and Thermal Properties of Cross-Linked Epoxy–Carbon Nanotube Nanocomposites: Role of Strengthening the Interfacial Interactions.* ACS Applied Materials & Interfaces, 2014. **6**(9): p. 6098-6110.
56. Lee, H.D., et al., *Defect-free surface modification methods for solubility-tunable carbon nanotubes.* Journal of Colloid and Interface Science, 2018. **509**: p. 307-317.
57. Zhao, Q., et al., *Dispersant selection for nanomaterials: Insight into dispersing functionalized carbon nanotubes by small polar aromatic organic molecules.* Carbon, 2015. **91**: p. 494-505.
58. Shen, C., et al., *Acyclic Cucurbit[n]uril Molecular Containers Selectively Solubilize Single-Walled Carbon Nanotubes in Water.* Journal of the American Chemical Society, 2012. **134**(17): p. 7254-7257.
59. Li, Z., et al., *Solubilization of Single-Walled Carbon Nanotubes Using a Peptide Aptamer in Water below the Critical Micelle Concentration.* Langmuir, 2015. **31**(11): p. 3482-3488.
60. Geckeler, K.E. and T. Premkumar, *Carbon nanotubes: are they dispersed or dissolved in liquids?* Nanoscale Research Letters, 2011. **6**(1): p. 136.
61. Lacerda, L., et al., *Carbon nanotubes as nanomedicines: From toxicology to pharmacology.* Advanced Drug Delivery Reviews, 2006. **58**(14): p. 1460-1470.
62. Ernst, F., et al., *Noncovalent Stable Functionalization Makes Carbon Nanotubes Hydrophilic and Biocompatible.* The Journal of Physical Chemistry C, 2017. **121**(34): p. 18887-18891.
63. Mananghaya, M., et al., *Theoretical investigation of the solubilization of COOH-functionalized single wall carbon nanotubes in water.* Journal of Molecular Liquids, 2016. **215**: p. 780-786.
64. Zheng, M., et al., *DNA-assisted dispersion and separation of carbon nanotubes.* Nature Materials, 2003. **2**: p. 338.
65. Chen, M., X. Qin, and G. Zeng, *Biodegradation of Carbon Nanotubes, Graphene, and Their Derivatives.* Trends in Biotechnology, 2017. **35**(9): p. 836-846.
66. Hou, J., et al., *Biodegradation of Single-Walled Carbon Nanotubes in Macrophages through Respiratory Burst Modulation.* International Journal of Molecular Sciences, 2016. **17**(3): p. 409.
67. Firme, C.P., 3rd and P.R. Bandaru, *Toxicity issues in the application of carbon nanotubes to biological systems.* Nanomedicine, 2010. **6**(2): p. 245-56.
68. Smart, S.K., et al., *The biocompatibility of carbon nanotubes.* Carbon, 2006. **44**(6): p. 1034-1047.
69. Sayes, C.M., et al., *Functionalization density dependence of single-walled carbon nanotubes cytotoxicity in vitro.* Toxicol Lett, 2006. **161**(2): p. 135-42.
70. Hwang, Y., S.-H. Park, and J. Lee, *Applications of Functionalized Carbon Nanotubes for the Therapy and Diagnosis of Cancer.* Polymers, 2017. **9**(1): p. 13.
71. Adeli, M., et al., *Carbon nanotubes in cancer therapy: a more precise look at the role of carbon nanotube–polymer interactions.* Chemical Society Reviews, 2013. **42**(12): p. 5231-5256.

72. Chik, M.W., et al., *Polymer-wrapped single-walled carbon nanotubes: a transformation toward better applications in healthcare.* Drug Deliv Transl Res, 2018.
73. Farvadi, F., et al., *Polyionic complex of single-walled carbon nanotubes and PEG-grafted-hyperbranched polyethyleneimine (PEG-PEI-SWNT) for an improved doxorubicin loading and delivery: development and in vitro characterization.* Artificial Cells, Nanomedicine, and Biotechnology, 2017. **45**(5): p. 855-863.
74. Liu, Z., et al., *Supramolecular Chemistry on Water-Soluble Carbon Nanotubes for Drug Loading and Delivery.* ACS Nano, 2007. **1**(1): p. 50-56.
75. Arunan, E., et al., *Definition of the hydrogen bond (IUPAC Recommendations 2011)*, in *Pure and Applied Chemistry*. 2011. p. 1637.
76. Grabowski, S.J., *What Is the Covalency of Hydrogen Bonding?* Chemical Reviews, 2011. **111**(4): p. 2597-2625.
77. Arunan, E., et al., *Defining the hydrogen bond: An account (IUPAC Technical Report)*, in *Pure and Applied Chemistry*. 2011. p. 1619.
78. Kar, T. and S. Scheiner, *Comparison of Cooperativity in CH···O and OH···O Hydrogen Bonds.* The Journal of Physical Chemistry A, 2004. **108**(42): p. 9161-9168.
79. Steiner, T., *The Hydrogen Bond in the Solid State.* Angewandte Chemie International Edition, 2002. **41**(1): p. 48-76.
80. Guevara-Vela, J.M., et al., *The nature of resonance-assisted hydrogen bonds: a quantum chemical topology perspective.* Physical Chemistry Chemical Physics, 2016. **18**(38): p. 26383-26390.
81. Lin, X., W. Wu, and Y. Mo, *A Direct Proof of the Resonance-Impaired Hydrogen Bond (RIHB) Concept.* Chemistry – A European Journal, 2018. **24**(5): p. 1053-1056.
82. Jesus, A.J.L. and J.S. Redinha, *Charge-Assisted Intramolecular Hydrogen Bonds in Disubstituted Cyclohexane Derivatives.* The Journal of Physical Chemistry A, 2011. **115**(48): p. 14069-14077.
83. Gilli, P., et al., *Predicting Hydrogen-Bond Strengths from Acid−Base Molecular Properties. The pKa Slide Rule: Toward the Solution of a Long-Lasting Problem.* Accounts of Chemical Research, 2009. **42**(1): p. 33-44.
84. Klinman, J.P., *Low Barrier Hydrogen Bonds: Getting Close, but Not Sharing.* ACS Central Science, 2015. **1**(3): p. 115-116.
85. Zhao, Y., et al., *The effect of benzo-annelation on intermolecular hydrogen bond and proton transfer of 2-methyl-3-hydroxy-4(1H)-quinolone in methanol: A TD-DFT study.* Journal of Physical Organic Chemistry, 2018. **31**(5): p. e3803.
86. Zhang, T., et al., *A detailed DFT/TDDFT study on excited-state intramolecular hydrogen bonding dynamics and proton-transfer mechanism of 2-phenanthro[9,10-d]oxazol-2-yl-phenol.* Journal of Physical Organic Chemistry, 2018. **31**(10): p. e3857.
87. Nochebuena, J., C. Cuautli, and J. Ireta, *Origin of cooperativity in hydrogen bonding.* Physical Chemistry Chemical Physics, 2017. **19**(23): p. 15256-15263.
88. Efimov, A.V. and E.V. Brazhnikov, *Relationship between intramolecular hydrogen bonding and solvent accessibility of side-chain donors and acceptors in proteins.* FEBS Letters, 2003. **554**(3): p. 389-393.
89. Lonardi, A., P. Oborský, and P.H. Hünenberger, *Solvent-Modulated Influence of Intramolecular Hydrogen-Bonding on the Conformational Properties of the Hydroxymethyl Group in Glucose and Galactose: A Molecular Dynamics Simulation Study.* Helvetica Chimica Acta, 2017. **100**(1): p. e1600158.
90. Lowe, J.P. and K. Peterson, *Quantum Chemistry*. 2005: Elsevier Academic Press.
91. Mueller, M.P., *Fundamentals of Quantum Chemistry: Molecular Spectroscopy and Modern Electronic Structure Computations*. 1 ed. 2001: Springer US.
92. Tsuneda, T., *Density functional theory in quantum chemistry.* 2014.
93. Jensen, F., *Introduction to Computational Chemistry*. 2 ed. 2007: John Wiley & Sons Ltd.
94. Hinchliffe, A., *Molecular Modelling for Beginners*. 2003: Wiley.

95. Koch, W. and M.C. Holthausen, *A chemist's guide to density functional theory*. 2002, Weinheim: Wiley-VCH.
96. Cramer, C.J., *Essentials of Computational Chemistry: Theories and Models*. 2 ed. 2004: John Wiley & Sons Ltd. 618.
97. Cohen, A.J., P. Mori-Sánchez, and W. Yang, *Challenges for Density Functional Theory.* Chemical Reviews, 2012. **112**(1): p. 289-320.
98. van Mourik, T., M. Bühl, and M.-P. Gaigeot, *Density functional theory across chemistry, physics and biology.* Philosophical transactions. Series A, Mathematical, physical, and engineering sciences, 2014. **372**(2011): p. 20120488-20120488.
99. Martin, R.M., *Electronic Structure: Basic Theory and Practical Methods*. 2004, Cambridge: Cambridge University Press.
100. Mardirossian, N. and M. Head-Gordon, *Thirty years of density functional theory in computational chemistry: an overview and extensive assessment of 200 density functionals.* Molecular Physics, 2017. **115**(19): p. 2315-2372.
101. Ireta, J., J. Neugebauer, and M. Scheffler, *On the Accuracy of DFT for Describing Hydrogen Bonds: Dependence on the Bond Directionality.* The Journal of Physical Chemistry A, 2004. **108**(26): p. 5692-5698.
102. Zhao, Y. and D.G. Truhlar, *The M06 suite of density functionals for main group thermochemistry, thermochemical kinetics, noncovalent interactions, excited states, and transition elements: two new functionals and systematic testing of four M06-class functionals and 12 other functionals.* Theoretical Chemistry Accounts, 2008. **120**(1): p. 215-241.
103. Burke, K., *Perspective on density functional theory.* The Journal of Chemical Physics, 2012. **136**(15): p. 150901.
104. Pribram-Jones, A., D.A. Gross, and K. Burke, *DFT: A Theory Full of Holes?* Annual Review of Physical Chemistry, 2015. **66**(1): p. 283-304.
105. Walker, M., et al., *Performance of M06, M06-2X, and M06-HF Density Functionals for Conformationally Flexible Anionic Clusters: M06 Functionals Perform Better than B3LYP for a Model System with Dispersion and Ionic Hydrogen-Bonding Interactions.* The Journal of Physical Chemistry A, 2013. **117**(47): p. 12590-12600.
106. Treitel, N., et al., *Calculations of PAH anions: When are diffuse functions necessary?* Physical Chemistry Chemical Physics, 2004. **6**(6): p. 1113-1121.
107. Lynch, B.J., Y. Zhao, and D.G. Truhlar, *Effectiveness of Diffuse Basis Functions for Calculating Relative Energies by Density Functional Theory.* The Journal of Physical Chemistry A, 2003. **107**(9): p. 1384-1388.
108. Kar, T., S. Scheiner, and A.K. Roy, *Reliability of Approximate Methods to Study Tip-Functionalized Single-Wall Carbon Nanotubes.* The Journal of Physical Chemistry C, 2012. **116**(48): p. 25401-25406.
109. Marenich, A.V., C.J. Cramer, and D.G. Truhlar, *Universal Solvation Model Based on Solute Electron Density and on a Continuum Model of the Solvent Defined by the Bulk Dielectric Constant and Atomic Surface Tensions.* The Journal of Physical Chemistry B, 2009. **113**(18): p. 6378-6396.
110. Lian, P., et al., *Quantum Chemical Calculation of pKas of Environmentally Relevant Functional Groups: Carboxylic Acids, Amines, and Thiols in Aqueous Solution.* The Journal of Physical Chemistry A, 2018. **122**(17): p. 4366-4374.
111. Li, H., et al., *Density functional theory prediction of pKa for carboxylated single-wall carbon nanotubes and graphene.* Chemical Physics, 2017. **490**: p. 47-54.
112. Kumar, P.S.V., V. Raghavendra, and V. Subramanian, *Bader's Theory of Atoms in Molecules (AIM) and its Applications to Chemical Bonding.* Journal of Chemical Sciences, 2016. **128**(10): p. 1527-1536.
113. Lane, J.R., et al., *Are Bond Critical Points Really Critical for Hydrogen Bonding?* Journal of Chemical Theory and Computation, 2013. **9**(8): p. 3263-3266.

114. Duarte, D.J.R., E.L. Angelina, and N.M. Peruchena, *Physical meaning of the QTAIM topological parameters in hydrogen bonding.* Journal of Molecular Modeling, 2014. **20**(11): p. 2510.
115. Fuster, F. and S.J. Grabowski, *Intramolecular Hydrogen Bonds: the QTAIM and ELF Characteristics.* The Journal of Physical Chemistry A, 2011. **115**(35): p. 10078-10086.
116. Contreras-García, J., et al., *A benchmark for the non-covalent interaction (NCI) index or… is it really all in the geometry?* Theoretical Chemistry Accounts, 2016. **135**(10): p. 242.
117. Alikhani, M.E., F. Fuster, and B. Silvi, *What Can Tell the Topological Analysis of ELF on Hydrogen Bonding?* Structural Chemistry, 2005. **16**(3): p. 203-210.
118. Pilmé, J., *Electron localization function from density components.* Journal of Computational Chemistry, 2017. **38**(4): p. 204-210.
119. Silvi, B. and H. Ratajczak, *Hydrogen bonding and delocalization in the ELF analysis approach.* Physical Chemistry Chemical Physics, 2016. **18**(39): p. 27442-27449.
120. Ghafouri, R., F. Ektefa, and M. Zahedi, *Characterization of Hydrogen Bonds in the End-Functionalized Single-Wall Carbon Nanotubes: A DFT Study.* Nano, 2014. **10**(03): p. 1550036.
121. Kar, T., et al., *Solvation Enhances the Distinction between Carboxylated Armchair and Zigzag Single-Wall Carbon Nanotubes (SWNT-COOH).* The Journal of Physical Chemistry C, 2017. **121**(17): p. 9516-9527.
122. Kupka, T., et al., *DFT calculations of structures, 13C NMR chemical shifts, and Raman RBM mode of simple models of small-diameter zigzag (4,0) carboxylated single-walled carbon nanotubes.* Magnetic Resonance in Chemistry, 2012. **50**(2): p. 142-151.
123. Kar, T., et al., *Unusual Low-Vibrational C═O Mode of COOH Can Distinguish between Carboxylated Zigzag and Armchair Single-Wall Carbon Nanotubes.* The Journal of Physical Chemistry C, 2012. **116**(49): p. 26072-26083.
124. Chełmecka, E., et al., *DFT studies of COOH tip-functionalized zigzag and armchair single wall carbon nanotubes.* Journal of Molecular Modeling, 2012. **18**(5): p. 2241-2246.
125. Corry, B., *Water and ion transport through functionalised carbon nanotubes: implications for desalination technology.* Energy & Environmental Science, 2011. **4**(3): p. 751-759.
126. Hanwell, M.D., et al., *Avogadro: an advanced semantic chemical editor, visualization, and analysis platform.* Journal of Cheminformatics, 2012. **4**(1): p. 17.
127. Humphrey, W., A. Dalke, and K. Schulten, *VMD: Visual molecular dynamics.* Journal of Molecular Graphics, 1996. **14**(1): p. 33-38.
128. Pettersen, E.F., et al., *UCSF Chimera—A visualization system for exploratory research and analysis.* Journal of Computational Chemistry, 2004. **25**(13): p. 1605-1612.
129. Tarini, M., P. Cignoni, and C. Montani, *Ambient Occlusion and Edge Cueing for Enhancing Real Time Molecular Visualization.* IEEE Transactions on Visualization and Computer Graphics, 2006. **12**(5): p. 1237-1244.
130. Frisch, M.J., et al., *Gaussian 09, Revision D. 01, Gaussian.* Inc.: Wallingford, CT, 2009.
131. Saadat, K. and H. Tavakol, *Study of noncovalent interactions of end-caped sulfur-doped carbon nanotubes using DFT, QTAIM, NBO and NCI calculations.* Structural Chemistry, 2016. **27**(3): p. 739-751.
132. Lu, T. and F. Chen, *Multiwfn: A multifunctional wavefunction analyzer.* Journal of Computational Chemistry, 2012. **33**(5): p. 580-592.
133. Lu, T. and F. Chen, *Quantitative analysis of molecular surface based on improved Marching Tetrahedra algorithm.* Journal of Molecular Graphics and Modelling, 2012. **38**: p. 314-323.
134. Lara, I.V., I. Zanella, and S.B. Fagan, *Functionalization of carbon nanotube by carboxyl group under radial deformation.* Chemical Physics, 2014. **428**: p. 117-120.
135. Tiwari, G., et al., *Drug delivery systems: An updated review.* International journal of pharmaceutical investigation, 2012. **2**(1): p. 2-11.
136. Patra, J.K., et al., *Nano based drug delivery systems: recent developments and future prospects.* Journal of Nanobiotechnology, 2018. **16**(1): p. 71.
137. Karanth, H. and R.S.R. Murthy, *pH-Sensitive liposomes-principle and application in cancer therapy.* Journal of Pharmacy and Pharmacology, 2007. **59**(4): p. 469-483.

138. Paasonen, L., et al., *Gold-embedded photosensitive liposomes for drug delivery: Triggering mechanism and intracellular release.* Journal of Controlled Release, 2010. **147**(1): p. 136-143.
139. Paliwal, S.R., R. Paliwal, and S.P. Vyas, *A review of mechanistic insight and application of pH-sensitive liposomes in drug delivery.* Drug Delivery, 2015. **22**(3): p. 231-242.
140. Kariduraganavar, M.Y., et al., *Chapter 6 - Protein Nanocarriers for Targeted Drug Delivery for Cancer Therapy*, in *Nanocarriers for Drug Delivery*, S.S. Mohapatra, et al., Editors. 2019, Elsevier. p. 173-204.
141. Webber, M.J. and R. Langer, *Drug delivery by supramolecular design.* Chemical Society Reviews, 2017. **46**(21): p. 6600-6620.
142. Jin, X., et al., *Supramolecular nanoscale drug-delivery system with ordered structure.* National Science Review, 2019.
143. Lin, X., et al., *Induction, Resonance, and Secondary Electrostatic Interaction on Hydrogen Bonding in the Association of Amides and Imides.* The Journal of Organic Chemistry, 2018. **83**(21): p. 13446-13453.
144. van der Lubbe, S.C.C., et al., *Secondary Electrostatic Interaction Model Revised: Prediction Comes Mainly from Measuring Charge Accumulation in Hydrogen-Bonded Monomers.* Journal of the American Chemical Society, 2019. **141**(12): p. 4878-4885.
145. Nagy, P., *Competing Intramolecular vs. Intermolecular Hydrogen Bonds in Solution.* International Journal of Molecular Sciences, 2014. **15**(11): p. 19562.
146. White, K.A., B.K. Grillo-Hill, and D.L. Barber, *Cancer cell behaviors mediated by dysregulated pH dynamics at a glance.* Journal of cell science, 2017. **130**(4): p. 663-669.
147. Vögele, M., J. Köfinger, and G. Hummer, *Molecular dynamics simulations of carbon nanotube porins in lipid bilayers.* Faraday Discussions, 2018. **209**(0): p. 341-358.
148. Corry, B., *Mechanisms of selective ion transport and salt rejection in carbon nanostructures.* MRS Bulletin, 2017. **42**(4): p. 306-310.
149. Thomas, M. and B. Corry, *A computational assessment of the permeability and salt rejection of carbon nanotube membranes and their application to water desalination.* Philos Trans A Math Phys Eng Sci, 2016. **374**(2060).
150. Liu, B., et al., *Carbon Nanotube Based Artificial Water Channel Protein: Membrane Perturbation and Water Transportation.* Nano Letters, 2009. **9**(4): p. 1386-1394.
151. Melchionna, M., et al., *Carbon nanotubes and catalysis: the many facets of a successful marriage.* Catalysis Science & Technology, 2015. **5**(8): p. 3859-3875.

Appendixes

Appendix 1 – Carbon nanotube bond length and angle parameters.

		$C - C$ Bond Lenght			
(n,m)	**System Type**	**Mean/Å**	**Standard Deviation**	**Relative Error (%)[1]**	**Reference/Å[2]**
(6,0)	Pristine	1.429	0.007	0.07	1.430
	Closed	1.432	0.006	0.22	
	Open	1.432	0.006	0.21	
(6,3)	Pristine	1.419	0.024	-	-
	Closed	1.420	0.025	0.09	
	Open	1.420	0.025	0.09	
(8,0)	Pristine	1.424	0.009	0.23	1.427
	Closed	1.424	0.008	0.00	
	Open	1.424	0.009	0.00	
(9,0)	Pristine	1.422	0.009	0.39	1.428
	Closed	1.422	0.008	0.01	
	Open	1.422	0.008	0.06	
(10,0)	Pristine	1.421	0.009	0.40	1.427
	Closed	1.421	0.009	0.03	
	Open	1.421	0.009	0.02	

		$C - C - C$ Angle			
(n,m)	**Conformation**	**Mean/°**	**Standard Deviation**	**Relative Error (%)[1]**	**Reference/°[2]**
(6,0)	-	117.32	2.37	0.34	116.93
	Closed	118.03	2.71	0.60	
	Open	117.91	2.40	0.50	
(6,3)	-	118.64	1.28		
	Closed	118.62	2.10	0.01	
	Open	118.68	2.12	0.03	
(8,0)	-	118.16	1.37	0.03	118.20
	Closed	118.16	1.44	0.00	
	Open	118.17	1.39	0.01	
(9,0)	-	118.65	1.00	0.08	118.56
	Closed	118.74	1.45	0.07	
	Open	118.63	1.40	0.04	
(10,0)	-	118.61	1.39	0.03	118.85
	Closed	118.75	0.97	0.12	
	Open	118.77	1.10	0.10	

---

[1] Relative error between pristine systems and a reference and functionalized systems and pristine.

[2] Kupka T, Stachów M, Stobiński L, Kaminský J. Calculation of Raman parameters of real-size zigzag (n, 0) single-walled carbon nanotubes using finite-size models. Physical Chemistry Chemical Physics. 2016;18(36):25058-25069.

Appendix 2 – Bond lengths associated with the functionalizations.

			(n,m)									
			(6,0)		(6,3)		(8,0)		(9,0)		(10,0)	
		F	**Closed**	**Opened**	**Closed**	**Opened**	**Closed**	**Opened**	**Closed**	**Opened**	**Closed**	**Opened**
Bond Lenght/Å	$O-H$	F1	0.982	0.974	0.978	0.974	0.993	0.973	0.986	0.973	0.995	0.974
		F2	0.982	0.974	0.978	0.974	0.993	0.973	0.983	0.974	0.995	0.974
		F3			0.978	0.974			0.980	0.974		
	$C=O$	F1	1.218	1.205	1.210	1.205	1.223	1.208	1.213	1.207	1.224	1.208
		F2	1.218	1.205	1.210	1.205	1.223	1.208	1.219	1.205	1.224	1.208
		F3			1.210	1.205			1.214	1.209		
	$C-OH$	F1	1.331	1.349	1.339	1.348	1.323	1.344	1.324	1.341	1.323	1.344
		F2	1.331	1.349	1.339	1.348	1.323	1.344	1.325	1.343	1.323	1.344
		F3			1.340	1.348			1.334	1.343		
	$C-CH2$	F1	1.518	1.505	1.525	1.511	1.520	1.503	1.519	1.512	1.522	1.504
		F2	1.518	1.505	1.525	1.511	1.520	1.503	1.515	1.506	1.522	1.504
		F3			1.525	1.511			1.516	1.504		
	$CH2-C$	F1	1.522	1.513	1.528	1.515	1.526	1.513	1.526	1.526	1.525	1.514
		F2	1.522	1.513	1.528	1.515	1.526	1.513	1.521	1.517	1.525	1.514
		F3			1.528	1.515			1.521	1.513		

Appendix 3 – Bond and dihedral angles associated with the functionalizations.

			(n,m)									
			(6,0)		(6,3)		(8,0)		(9,0)		(10,0)	
		F	**Closed**	**Opened**	**Closed**	**Opened**	**Closed**	**Opened**	**Closed**	**Opened**	**Closed**	**Opened**
Angle/°	$C-CH2-C$	F1	118.76	110.70	116.56	110.36	114.91	113.72	114.91	111.86	110.36	113.77
		F2	118.76	110.69	116.50	110.34	114.90	113.73	114.80	112.91	110.36	113.77
		F3			116.48	110.35			115.46	113.98		
	$O=C-OH$	F1	122.28	122.46	121.81	122.73	122.01	122.62	123.53	123.33	122.36	122.74
		F2	122.28	122.46	121.82	122.72	122.01	122.62	122.43	123.31	122.36	122.74
		F3			121.82	122.72			122.11	122.44		
Dihedral Angle/°	$C1=C-CH2-C$	F1	-81.94	66.87	-105.97	66.89	-79.69	155.65	-88.73	146.31	-78.79	149.86
		F2	-81.96	66.86	-106.06	66.93	-79.69	155.64	-85.56	145.46	-78.79	149.86
		F3			-106.00	66.95			-86.28	155.14		
	$C2=C-CH2-C$	F1	75.93	-147.64	67.33	-122.78	81.00	-51.40	82.05	-48.62	82.50	-50.87
		F2	75.88	-147.63	67.22	-122.75	81.02	-51.41	76.85	-52.15	82.50	-50.87
		F3			67.25	-122.72			78.48	-51.55		
	$C-CH2-C=O$	F1	82.71	92.55	73.93	101.40	86.65	127.01	73.48	114.74	90.15	129.32
		F2	82.82	92.53	73.42	101.29	86.68	127.02	70.79	70.79	90.15	129.32
		F3			73.24	101.19			73.94	126.18		
	$C-CH2-C-OH$	F1	-98.55	-86.86	-107.91	-77.72	-93.41	-54.46	-106.96	-65.35	-88.13	-52.31
		F2	-98.55	-86.88	-108.34	-77.85	-93.44	-54.46	-109.55	-51.99	-88.13	-52.31
		F3			-108.51	-77.94			-106.10	-51.15		

Appendix 4 – IR vibrational spectra.

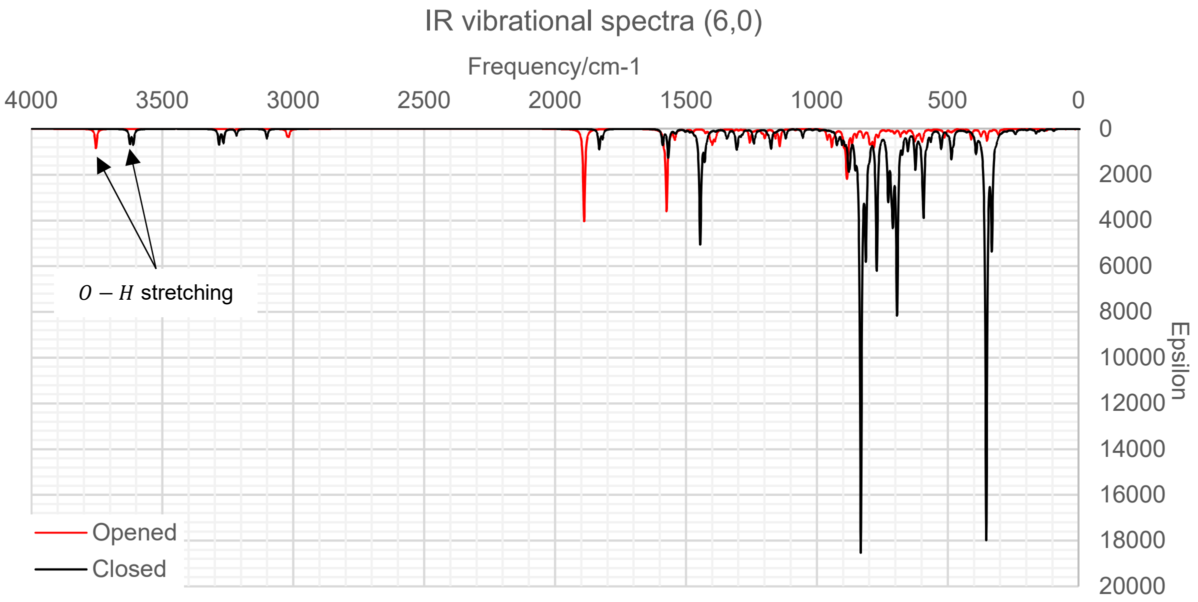

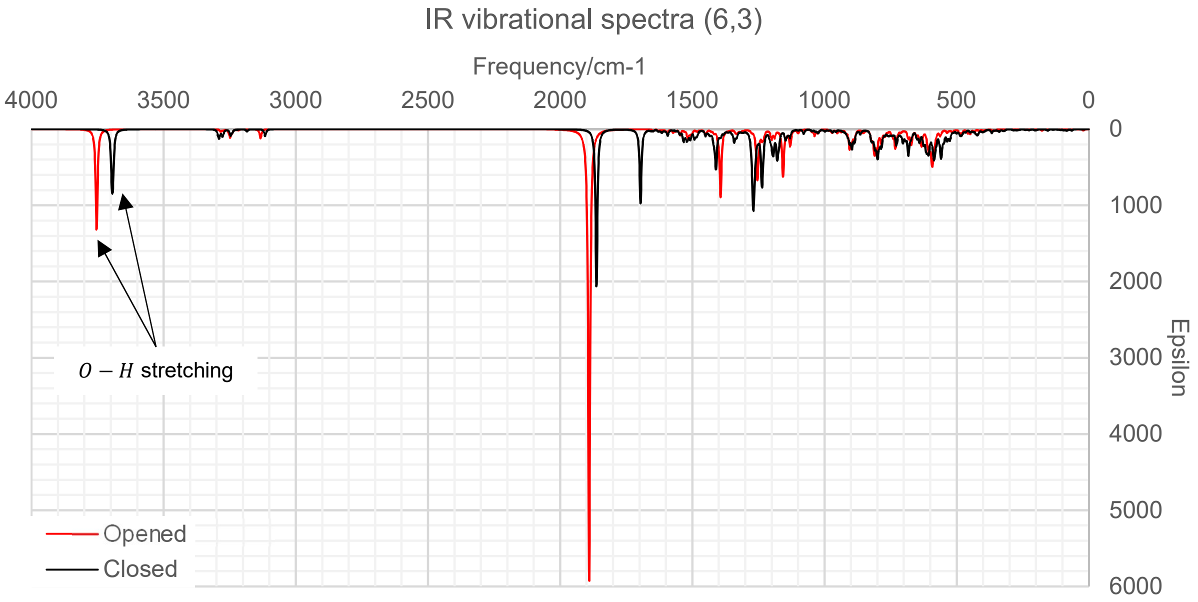

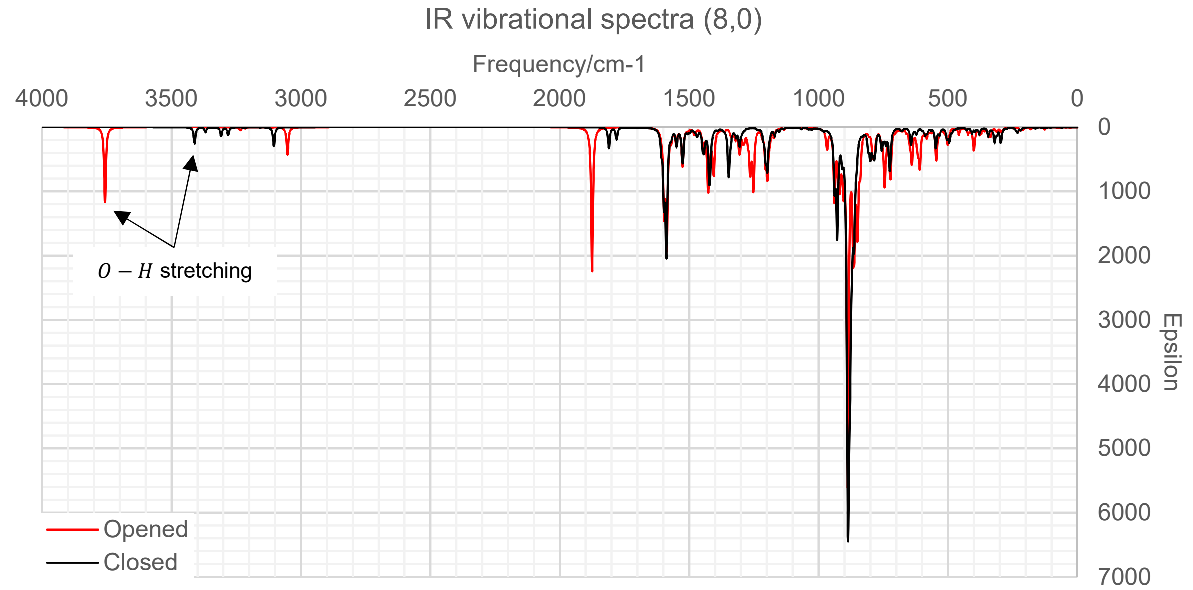
IR vibrational spectra (8,0)
Frequency/cm-1
4000
3500
3000
2500
2000
1500
1000
500
0
0
1000
2000
3000
4000
5000
6000
7000
Epsilon
$O-H$ stretching
Opened
Closed

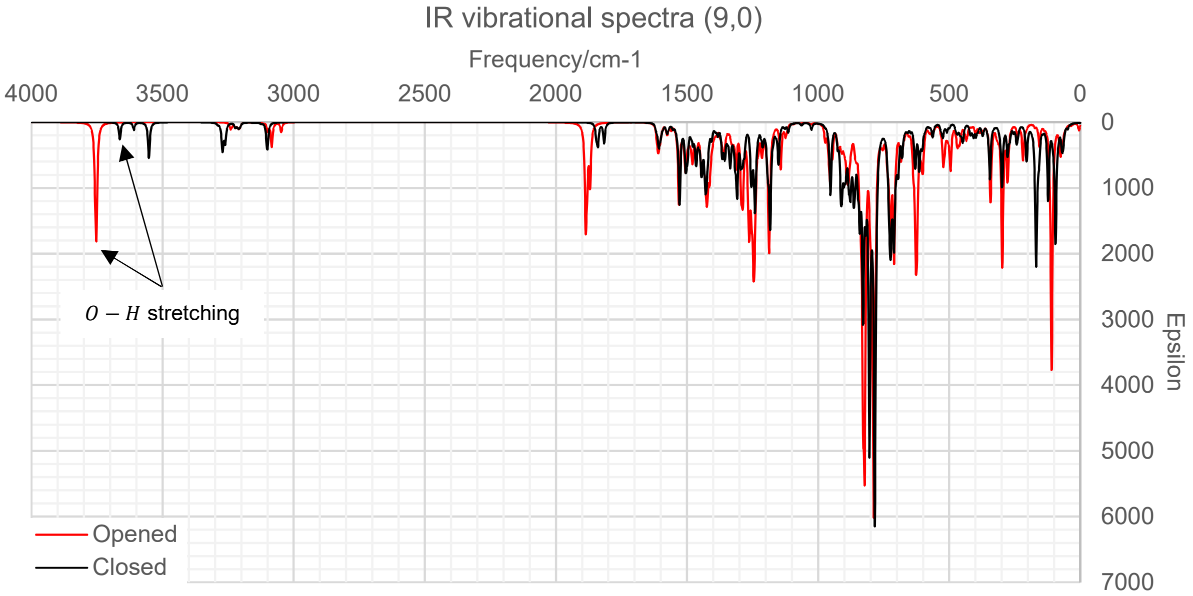
IR vibrational spectra (9,0)
Frequency/cm-1
4000
3500
3000
2500
2000
1500
1000
500
0
0
1000
2000
3000
4000
5000
6000
7000
Epsilon
$O-H$ stretching
Opened
Closed

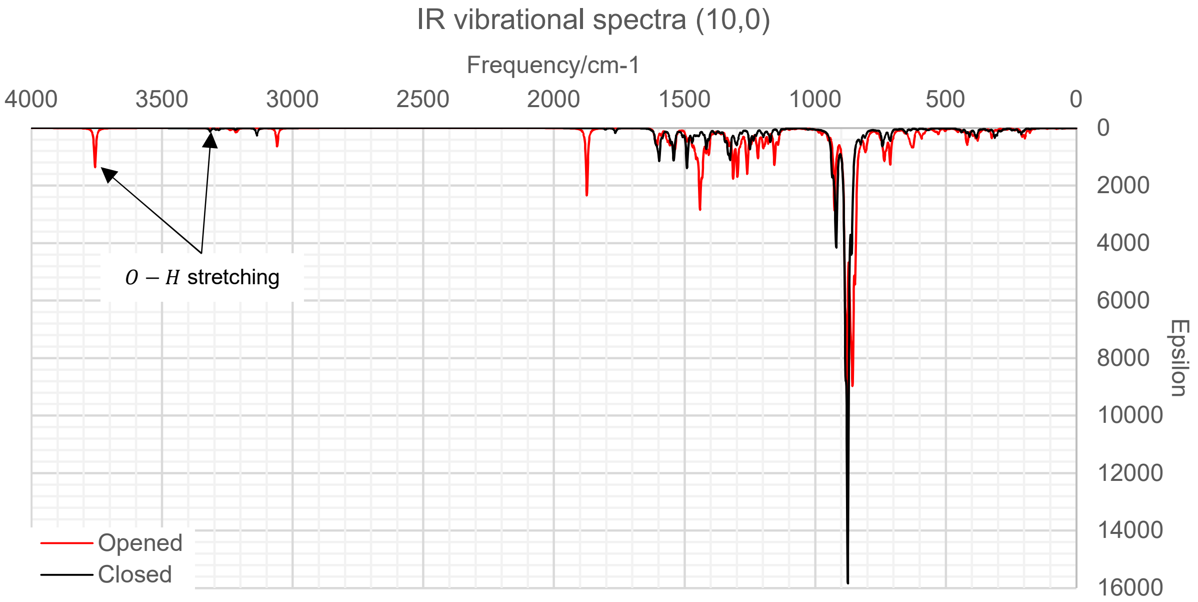
IR vibrational spectra (10,0)
Frequency/cm-1
4000
3500
3000
2500
2000
1500
1000
500
0
0
2000
4000
6000
8000
10000
12000
14000
16000
Epsilon
$O-H$ stretching
Opened
Closed

Appendix 5 – Topology parameters associated with all hydrogen bonds.

(n,m)	Hydrogen Bond	BCP	$\rho(r)$	$\nabla^2\rho(r)$	*s*	sign(λ_2)ρ	ELF
(6,0)	O80-H83…O82	187	0.025	0.094	0.345	-0.033	0.067
	O79-H81…O84	176	0.025	0.094	0.345	-0.033	0.067
	C55-H56...O84	138	0.018	0.063	0.310	-0.024	0.054
	C64-H65...O82	222	0.019	0.063	0.309	-0.024	0.054
	C58-H59...O79	204	0.018	0.061	0.310	-0.023	0.051
	C67-H68...O80	151	0.018	0.061	0.309	-0.023	0.052
	O82…O84	180	0.011	0.036	0.021	0.013	0.028
(6,3)	O94-H105…O108	250	0.016	0.069	0.357	-0.023	0.036
	O98-H103…O106	223	0.016	0.069	0.359	-0.023	0.036
	O102-H07…O104	180	0.016	0.069	0.359	-0.023	0.036
	C67-H86…O94	293	0.017	0.060	0.302	-0.022	0.047
	C74-H88…O98	201	0.017	0.060	0.302	-0.022	0.047
	C79-H89…O102	160	0.017	0.060	0.302	-0.022	0.046
	O106…C72	240	0.013	0.044	0.382	-0.016	0.039
	O104…C78	153	0.013	0.044	0.384	-0.016	0.039
	O108…C66	239	0.013	0.044	0.384	-0.016	0.039
	H90…H95	121	0.013	0.053	0.025	-0.024	0.037
	H85…H101	234	0.013	0.053	0.025	-0.024	0.037
	H87…H91	288	0.013	0.053	0.025	-0.024	0.037
(8,0)	O100-H107…O106	193	0.038	0.132	0.323	-0.047	0.119
	O104-H105…O108	182	0.038	0.132	0.323	-0.047	0.119
	C82-H93…O100	248	0.020	0.070	0.282	-0.025	0.056
	C74-H89…O104	119	0.020	0.070	0.282	-0.025	0.056
	C86-H95…O106	169	0.018	0.062	0.304	-0.023	0.051
	C78-H91…O108	212	0.018	0.062	0.304	-0.023	0.051
(9,0)	O116-H121…O123	177	0.026	0.109	0.308	-0.037	0.063
	O118-H124…O120	246	0.030	0.125	0.296	-0.041	0.075
	O112-H119…O122	241	0.023	0.097	0.313	-0.032	0.054
	C85-H101…O116	287	0.018	0.061	0.307	-0.023	0.051
	C97-H107…O112	226	0.018	0.061	0.316	-0.023	0.051
	C91-H104…O118	138	0.017	0.058	0.295	-0.022	0.048
	C99-H108…O122	273	0.017	0.057	0.339	-0.021	0.049
	C87-H102…O123	240	0.016	0.054	0.358	-0.020	0.046
	C93-H105…O120	144	0.014	0.050	0.357	-0.019	0.042
(10,0)	O132-H129…O128	211	0.038	0.127	0.340	-0.047	0.123
	O130-H131…O127	262	0.038	0.127	0.340	-0.047	0.123
	C105-H118…O130	298	0.014	0.054	0.296	-0.019	0.038
	C95-H113…O132	172	0.014	0.054	0.296	-0.019	0.038
	C99-H115…O127	268	0.013	0.049	0.330	-0.018	0.037
	C109-H120…O128	208	0.013	0.049	0.330	-0.018	0.037

Appendix 6 – Relative energy of the B3LYP/6-31g dihedral bidimensional scans.

(8,0)

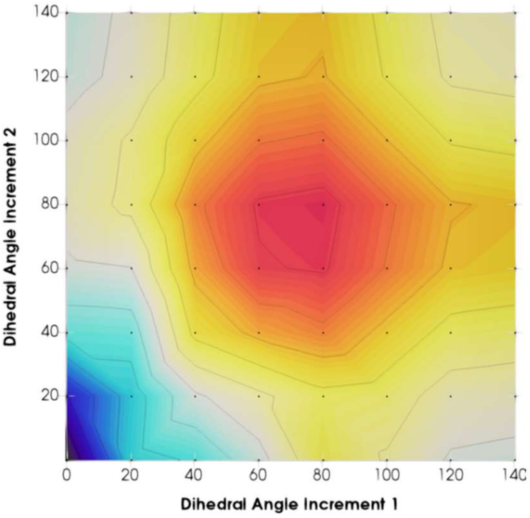

(10,0)

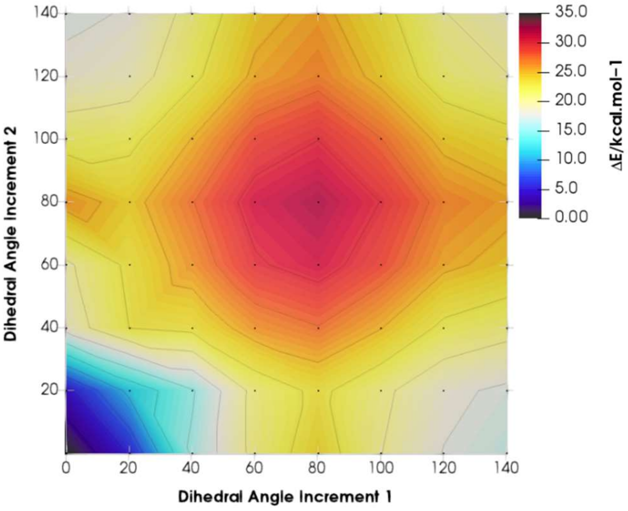

(9,0) 0º

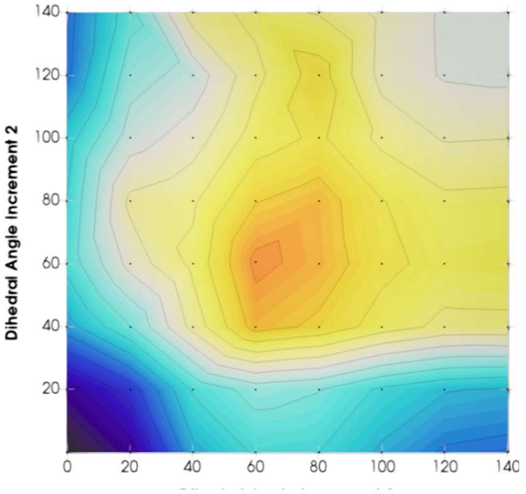

(9,0) 20º

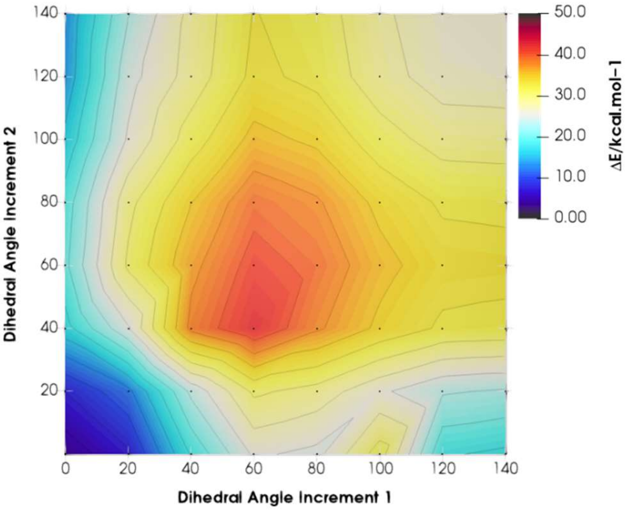

(9,0) 40º

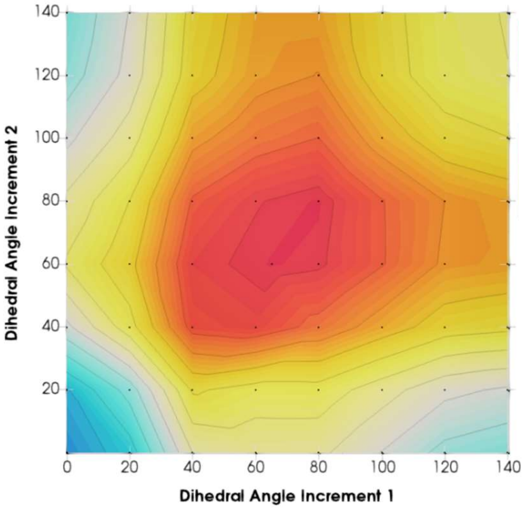

(9,0) 60º

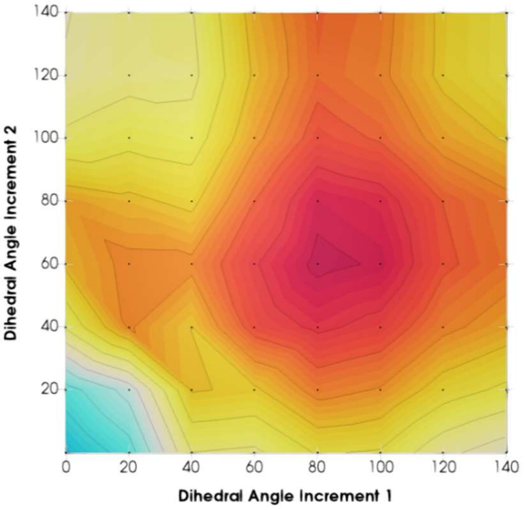

(9,0) 80º

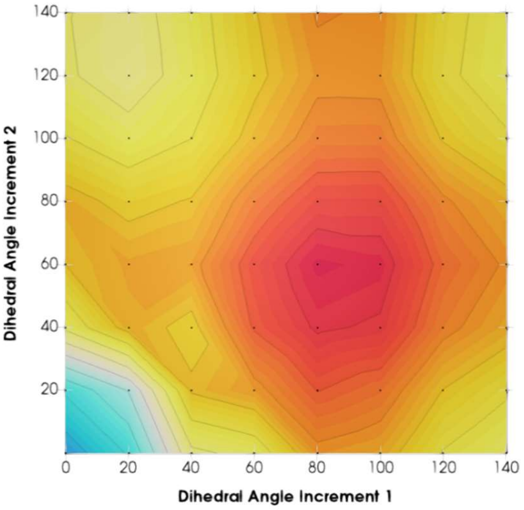

(9,0) 100º

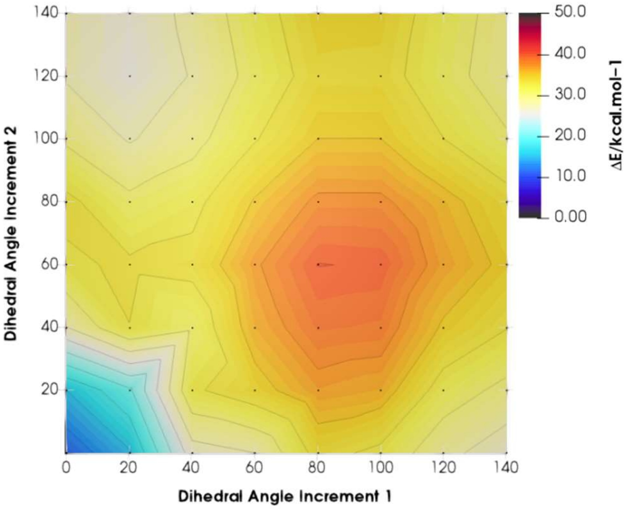

(9,0) 120º

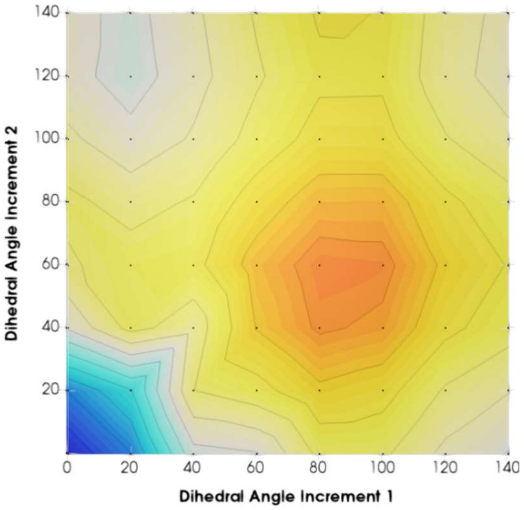

(9,0) 140º

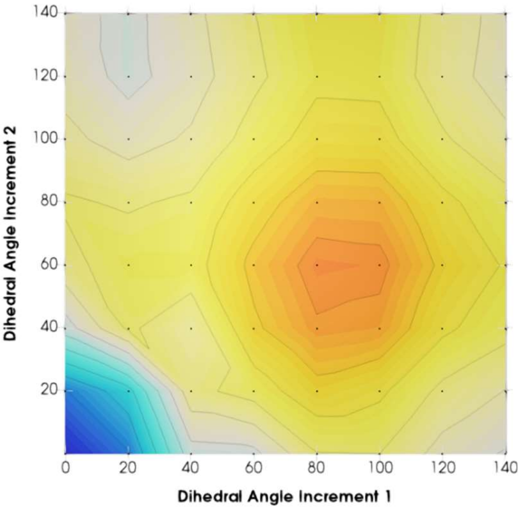

Conference Presentations

- **Oral communications:**

  Pinto, A. R., Magalhães, A. L. "*A Theoretical study on SWCNT End-Functionalization: Intramolecular Hydrogen Bonds as a Molecular Gate*" XII Encontro de Investigação Jovem da Universidade do Porto IJUP 2019

- **Poster presentations:**

  Pinto, A. R., Magalhães, A. L. "*A Theoretical study on SWCNT End-Functionalization: Intramolecular Hydrogen Bonds as a Molecular Gate*" XII Encontro Nacional de Estudantes de Bioquímica ENEBIOQ 2019

  Pinto, A. R., Magalhães, A. L. "*A Theoretical study on SWCNT End-Functionalization: Intramolecular Hydrogen Bonds as a Molecular Gate*" XXVI Encontro Nacional da Sociedade Química Portuguesa 2019

- **Awards:**

  Best Oral Communication in the Chemistry area
  Pinto, A. R., Magalhães, A. L. "*A Theoretical study on SWCNT End-Functionalization: Intramolecular Hydrogen Bonds as a Molecular Gate*" XII Encontro de Investigação Jovem da Universidade do Porto IJUP 2019